

Potential Substitutes for Replacement of Lead in Perovskite Solar Cells: A Review

Ravinder Kour, Sandeep Arya,* Sonali Verma, Jyoti Gupta, Pankaj Bandhoria, Vishal Bharti, Ram Datt, and Vinay Gupta

Lead halide perovskites have displayed the highest solar power conversion efficiencies of 23% but the toxicity issues of these materials need to be addressed. Lead-free perovskites have emerged as viable candidates for potential use as light harvesters to ensure clean and green photovoltaic technology. The substitution of lead by Sn, Ge, Bi, Sb, Cu and other potential candidates have reported efficiencies of up to 9%, but there is still a dire need to enhance their efficiencies and stability within the air. A comprehensive review is given on potential substitutes for lead-free perovskites and their characteristic features like energy bandgaps and optical absorption as well as photovoltaic parameters like open-circuit voltage (V_{OC}), fill factor, short-circuit current density (J_{SC}), and the device architecture for their efficient use. Lead-free perovskites do possess a suitable bandgap but have low efficiency. The use of additives has a significant effect on their efficiency and stability. The incorporation of cations like diethylammonium, phenylethyl ammonium, phenylethyl ammonium iodide, etc., or mixed cations at different compositions at the A-site is reported with engineered bandgaps having significant efficiency and stability. Recent work on the advancement of lead-free perovskites is also reviewed.

Russian mineralogist count Lev Aleksevich Perovski.^[1] Since then, the term perovskite has been used for any organic/inorganic compound (synthetic/natural) with the similar crystal structure and stoichiometry as of CaTiO_3 , that is, ABX_3 , where A is monovalent metallic cation, most usually from group I of the periodic table. B is divalent metallic cation, a transition metal and X is a nonmetallic anion (halide). However, for O^{2-} anions, A and B are divalent and tetravalent cations, respectively. The size of cation A must be larger than that of cation B. Ideally, perovskite crystal structure is described as a body centered cubic structure with monovalent cation A dodecahedrally (12-fold) coordinated by X anions as shown in Figure 1.^[2] The volume occupied by A ions depends on the electronegativity and size of B and X ions, respectively. A superfluity of organic/inorganic compounds has been discovered that exists in perovskite crystal structure framework ABX_3 like BaTiO_3 , SrTiO_3 , KNbO_3 , etc.

1. Introduction


Perovskite originally referred to a mineral calcium titanium oxide, CaTiO_3 , discovered in 1839 in Ural Mountains of Russia by Gustav Rose, a German mineralogist and later named after a

Generally, perovskite materials can be classified into two groups, namely, inorganic oxide perovskite and halide perovskite that further encompass alkali halide and organometal halide perovskite materials. There are some perovskite materials like MgCNi_3 having neither oxygen nor halide component and

R. Kour
Department of Physics
Government Degree College for Women
Kathua, Jammu and Kashmir 184102, India

Dr. S. Arya, S. Verma, J. Gupta
Department of Physics
University of Jammu
Jammu and Kashmir, Jammu 180006, India
E-mail: snp09arya@gmail.com

Dr. P. Bandhoria
Department of Physics
Government Gandhi Memorial Science College Jammu
Jammu and Kashmir, Jammu 180001, India

 The ORCID identification number(s) for the author(s) of this article can be found under <https://doi.org/10.1002/gch2.201900050>.

© 2019 The Authors. Published by WILEY-VCH Verlag GmbH & Co. KGaA, Weinheim. This is an open access article under the terms of the Creative Commons Attribution License, which permits use, distribution and reproduction in any medium, provided the original work is properly cited.

Dr. V. Bharti
Departamento de Ciência dos Materiais
Faculdade de Ciências e Tecnologia
FCT
Universidade Nova de Lisboa
2829-516, Campus de Caparica, Portugal

R. Datt
Advance Materials and Devices Division
CSIR-National Physical Laboratory
Dr. K. S. Krishnan Marg, New Delhi 110012, India

Dr. V. Gupta
Department of Mechanical and Materials Engineering
Khalifa University of Science and Technology
Masdar Institute
Masdar City 54224, Abu Dhabi, UAE

DOI: 10.1002/gch2.201900050

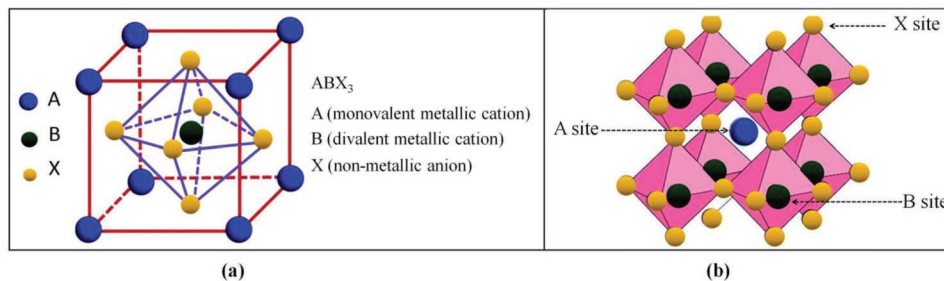


Figure 1. a) Schematic view of cubic perovskite crystal structure for ABX_3 compound, b) 3D crystal structure in which the A site is confined within a cage determined by the octahedral coordination of B site with X site. Reproduced with permission.^[1] Copyright 2019, Royal Society of Chemistry.

hence do not belong to either of the groups.^[3] In alkali halide perovskites, A-site is occupied by a monovalent organic cation such as CH_3NH_3 (methylammonium or MA), $NH_2(CH)NH_2$ (formamidinium or FA), or inorganic cations such as rubidium (Rb), caesium (Cs), etc., the B-site by a divalent metal cation lead (Pb) or tin (Sn), and X-site by a halide anion. In today's scientific world, it is the halide perovskites that have grabbed all the attention of silicon-dominated photovoltaics industry and whole of the photovoltaics research is now focused in developing perovskite materials for solar energy conversion.

The suitability of a particular combination of cations to organize into a perovskite structure can be estimated based on two important parameters. The first one is the Goldschmidt tolerance factor (t), a dimensionless number, calculated from the ratio of ionic radii^[4]

$$t = \frac{r_A + r_X}{\sqrt{2}(r_B + r_X)} \quad (1)$$

where r_A and r_B are the ionic radii of cations A and B, and r_X is the ionic radius of anion. For a particular perovskite structure, the tolerance factor (t) can be calculated by substituting the ionic radii of cations and anions. If $t = 1$, it indicates the formation of an ideal cubic structure having size of cation A larger than that of B. The tolerance factor (t) must lie in the range of 0.8–1.0 for the formation of stable perovskite structures. If $t < 0.8$ or $t > 1.0$, the cation A is too small or too big to fit into BX_6 octahedron, thereby resulting in the formation of alternative structures. The tolerance factor (t) leading to formation of different types of structures with examples is mentioned in **Table 1**.

The second one is the octahedral factor (μ) which is the ratio between ionic radii of B and X

$$\mu = \frac{r_B}{r_X} \quad (2)$$

The octahedral factor (μ) must lie in the range of 0.44–0.72 for B and X in order to form a stable BX_6 octahedron.^[2] The tolerance factor has an immense role to play in finding alternative lead halide perovskite materials as many different cations can be inserted in ABX_3 structure framework leading to development of varied materials with specific engineered properties.^[8]

The effective ionic radii of organic molecular cations and Shannon ionic radii of inorganic cations as well as the effective ionic radii of various anions are listed in **Table 2**.^[9–13]

The Goldschmidt tolerance factor (t) has played a pivotal role in development of perovskites^[10] and is now being used to engineer/synthesize new organic–inorganic stable perovskite structures by formulating the composition of perovskite. The tolerance factor can be tuned to the stable perovskite range by mixing distinct A/B cations and X anions in a particular composition.^[14–17]

2. Perovskite Sensitized Solar Cell

Solar energy has always been sought to be converted into electrical energy through photovoltaic effect of light absorbing semiconductor in order to obtain clean and green energy. The traditional first generation crystalline silicon solar employed for this purpose enjoy a market share of more than 90% in PV market.^[18] The second generation solar cells consist of thin films such as cadmium telluride, copper indium gallium selenide, and amorphous silicon. The third generation has a number of thin film technologies such as dye-sensitized solar cells (DSSCs) in development phase. The crystalline silicon solar cell has a theoretical limiting power efficiency of 33.16%^[19] noted as a Shockley Queisser limit in 1961. An efficiency of 25.6%^[20] for a silicon solar cell has been reported in 2014 that further grows to 46.1%^[21] in four-junction GaInP/GaAs/GaInAsP/GaInAs solar cell reported by French-German collaboration. The triple-junction thin film solar cells achieved an efficiency of 13.6% in June 2015.^[22] The research teams at NREL, EPFL, and GSEM have reported Sun efficiencies of dual-junction GaInP/GaAs solar cell devices up to 32.8%.^[23] Although, the monocrystalline silicon cells have photovoltaic conversion efficiency of more than 20%,^[24] they are characterized by high cost, difficult preparation conditions, and serious environmental pollution.^[25] Also, cadmium telluride and copper indium gallium selenium

Table 1. Goldschmidt tolerance factor (t) of various perovskite materials.^[5]

Goldschmidt tolerance factor (t)	Structure	Example
0.9–1.0	Cubic	$SrTiO_3$, ^[6] $BaTiO_3$ ^[7]
0.71–0.9	Several perovskite structures/ orthorhombic rhombohedral	$GdFeO_3$, $CaTiO_3$ ^[6]
<0.71	Ilmenite	$FeTiO_3$, ^[5] $KNbO_3$ ^[5]
>1	Hexagonal or tetragonal	$BaNiO_3$ ^[6]

Table 2. (a) Effective ionic radii of organic molecular cations. (b) Shannon ionic radii of inorganic cations. (c) Effective ionic radii of various anions.

(a)		
Cation A	Effective ionic radii (r_{eff}) [pm]	Ref.
Ammonium [NH ₄] ⁺	146	[10]
Hydrazinium [NH ₃ NH ₂] ⁺	217	[10]
Azetidinium [(CH) ₃ NH ₂] ⁺	250	[10]
Formamidinium [CH(NH ₂) ₂] ⁺	253	[10]
Imidazolium [C ₃ N ₂ H ₅] ⁺	258	[10]
Dimethylammonium [(CH) ₂ NH ₂] ⁺	272	[10]
Ethyl ammonium [(CH ₃ CH ₂)NH ₃] ⁺	274	[10]
Guanidinium [(NH ₂) ₃ C] ⁺	278	[10]
Tetramethylammonium [(CH ₃) ₄ N] ⁺	292	[10]
Thiazolium [C ₃ H ₄ NS] ⁺	320	[11]
Tropylium [C ₇ H ₇] ⁺	333	[11]
Hydroxylamine [NH ₃ OH] ⁺	216	[10]
Methylammonium [CH ₃ NH ₃] ⁺	217	[10]
Piperazinium [C ₄ H ₁₂ N ₂] ²⁺	322	[9]
Dabconium [C ₄ H ₁₄ N ₂] ²⁺	339	[9]
K ⁺	164	[12]
Rb ⁺	172	[12]
Cs ⁺	188	[12]

(b)		
Cation B	Effective ionic radii (r_{eff}) [pm]	Ref.
Be ²⁺	16	[12]
Mg ²⁺	72	[12]
Ca ²⁺	100	[12]
Sr ²⁺	118	[12]
Ba ²⁺	135	[12]
Mn ²⁺	66	[12]
Fe ²⁺	78	[12]
Co ²⁺	58	[12]
Ni ²⁺	55	[12]
Pd ²⁺	86	[12]
Pt ²⁺	60	[12]
Cu ²⁺	73	[12]
Zn ²⁺	60	[12]
Cd ²⁺	78	[12]
Hg ²⁺	69	[12]
Ge ²⁺	73	[12]
Sn ²⁺	110	[13]

Pb ²⁺	119	[12]
Eu ²⁺	117	[12]
Tm ²⁺	103	[12]
Yb ²⁺	103	[12]
Sn ^[4+]	69	[12]
Te ⁺	150	[12]
Au ⁺	137	[12]
Au ³⁺	85	[12]
Sb ⁺	76	[12]
Bi ³⁺	103	[12]
Te ^[4+]	97	[12]
La ³⁺	103	[12]
Ce ³⁺	101	[12]
Pr ³⁺	99	[12]
Nd ³⁺	98	[12]
Sm ³⁺	96	[12]
Eu ³⁺	95	[12]
Cd ³⁺	94	[12]
Dy ³⁺	91	[12]
Er ³⁺	89	[12]
Tm ³⁺	88	[12]
Lu ³⁺	86	[12]
Pu ³⁺	100	[12]
Am ³⁺	98	[12]
Bk ³⁺	96	[12]

(c)		
Anion X	Effective ionic radii (r_{eff}) [pm]	Ref.
Fluoride, F ⁻	129	[9]
Chloride, Cl ^[-]	181	[9]
Bromide, Br ^[-]	196	[9]
Iodide, I ^[-]	220	[10]
Formate, HCOO ^[-]	136	[9]
BH ₄ ^[-]	203	[11]

thin film solar cells' large-scale use puts a pressure on environmental pollution. DSSCs showing an efficiency of more than 13% have low cost and easy fabrication but absorption layer in such cells is very thick^[26] and light dyes used in such cells suffer from phenomenon of light bleaching.

An efficient solar cell technology must ensure low raw material and finished material cost, high light absorption and solar power conversion efficiency, high abundance of raw material, low toxicity, and less environmental pollution. In order to achieve it, the organic/inorganic perovskite compounds can be used in light harvesting layer as these materials have all the requisite properties that make them suitable for use in PV^[27] applications. With the discovery of metal halide perovskite, especially MAPbI₃, FAPbI₃ as light absorbers, the use of perovskites

in PV technology has been explored as they are cost effective and readily available for large-scale use.^[28–38] The organic–inorganic perovskite materials have been pioneering in fabricating high solar power conversion efficiency hybrid solar cells from time to time.^[32,39–45] Miyasaka and co-workers reported the first perovskite sensitized solar cell (PSSC) in between 2006 and 2008 using $\text{CH}_3\text{NH}_3\text{PbI}_3$ and $\text{CH}_3\text{NH}_3\text{PbBr}_3$ absorbers and reported solar power conversion efficiency varying between 0.4 and 2% for solid-state and liquid electrolyte cells, respectively.^[46,47] A MAPbI_3 -based solar cell with solar power conversion efficiency of 3.8% has been reported by Kojima et al. in 2009 and was the first peer reviewed publication on perovskite-sensitized solar cell.^[28] Park and co-workers using $\text{CH}_3\text{NH}_3\text{PbI}_3$ liquid electrolyte solar cell reported an improved efficiency of 6.5%.^[48] In 2011, Snaith along with his co-workers developed a solid-state perovskite solar cell (PSC) using 2,2(7,7)-tetrakis-(N,N-dimethoxyphenylamine)9,9(Spiro-bifluorene) (Spiro-OMeTAD) for hole transportation and produced solar power conversion efficiencies between 8 and 10%^[49] achieving a major breakthrough in performance efficiency of PSSC in comparison to DSSCs having only 7% efficiency.^[50] In 2012, Kim et al. replaced the liquid electrolyte with a solid-state hole conducting material depositing the perovskite precursor over the mesoporous TiO_2 layer achieving a solar power conversion efficiency (SPCE) of 9.7%.^[30] Later, increased efficiencies of 10.9% were reported by Lee et al.^[51] Gratzel and co-workers reported a SPCE of 15% by using sequential deposition to produce pinhole-free perovskite layer.^[52] Liu et al. introduced Zn_2SnO_4 nanocrystalline thin film on PCBM buffer layer to make electron extraction process easy, thereby, increasing SPCE to 17.76%.^[53] You et al. and Yang et al. first fabricated all metal oxide layer based perovskite solar cell reporting an efficiency of 16.1% and more stability of the material in 2016.^[54] Yang et al. and his team reported SPCE of 22.1%^[55] in defect engineered thin perovskite layers in PSSCs containing formamidinium with multiple cations and mixed halide anions in 2017. The SPCE of solid-state PSSCs was around 10% in 2012 that later grew up to 22.1% in 2017. This has been achieved through engineering of perovskite composition and thin film deposition methods. The big issue of degradation of perovskite in polar liquid electrolyte has been solved by use of solid-state PSSCs that have shown 500 h stability in ambient conditions without encapsulation but still the PSSCs have to prove its stability in air, on exposure to humidity,^[56–58] UV light,^[59] and high tem-

peratures.^[60,61] Research has also revealed that PSSCs also suffer from anomalous current–voltage hysteresis as reported by Snaith and co-workers in 2014^[62] that can have adverse effects on the stability of PSSCs.^[63,64]

3. Device Configuration and Working Principles of Perovskite Solar Cell

In the first perovskite solar cell fabricated in 2009, perovskite nanoparticles were used as a light absorber replacing dyes in dye-sensitized solar cells. In the fabricated device, mesoporous TiO_2 layer of several micrometer thickness acts as an anode and a platinum-coated glass acted as a cathode in a liquid electrolyte based device.^[28,29] However, the device suffered seriously from the stability issue as the perovskite light absorber layer dissolves or decomposes in the liquid electrolyte very rapidly. Hence, the liquid electrolyte was replaced by a solid-state material to act as a hole transport material (HTM) resulting in a solid-state mesoscopic perovskite solar cell with an improved stability. Organic Spiro-OMeTAD was used as a hole transport material in such cells.^[49] The perovskite materials when used as a light absorber enhances the device stability and performance to its broad optical absorption range than the conventional dyes.^[65] In a mesoscopic perovskite solar cells, a compact metal oxide (TiO_2) layer is deposited on a fluorine-doped tin oxide (FTO) glass substrate by spin-coating on which is further deposited a mesoporous TiO_2 layer by spin-coating. The perovskite light absorber layer is grown on the scaffold of mesoporous TiO_2 layer which is further deposited by a HTM by spin-coating and finally to a metal-back electrode (Ag or Au). The device configuration of mesoporous perovskite solar cell is shown in **Figure 2a**.^[66]

TiO_2 is most commonly employed in mesoporous layer that facilitates in the formation of inner connected layer of perovskite crystals by allowing their deep penetration into the pores of mesoporous layer. Compact TiO_2 layer transports electrons, blocks holes, and suppresses the recombination of electron–hole pairs. The mesoporous TiO_2 layer needs a high-temperature sintering that can consequently increase the device fabrication time. Since the perovskite materials have ambipolar nature, they have the potential of transporting electrons and holes on their own in between two electrodes so a planar structure is viable for them.^[67] Also, the perovskite solar cells

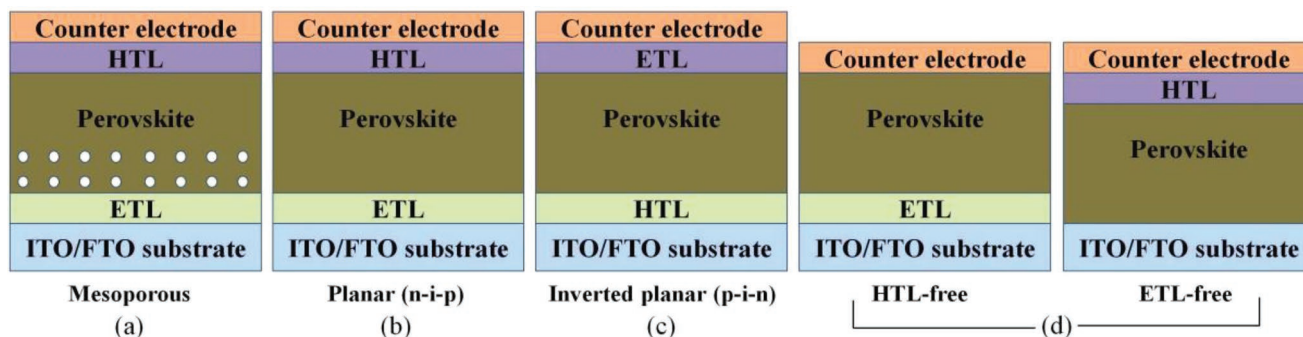


Figure 2. a) Device structure of mesoporous PSSCs, b) planar heterojunction, c) inverted planar PSSCs, and d) HTM-free PSSCs. Reproduced with permission.^[66] Copyright 2016, Springer Nature.

using planar structure over time have revealed the best device performance as that of a mesoporous structure.^[32,67] The device with planar configuration has reported almost 100% internal quantum efficiencies ascertaining them as an efficient device structure.^[43] Thus, typically there are two major device configurations for a perovskite solar cell, viz., a planar heterojunction/conventional structure (n-i-p) and an inverted planar structure (p-i-n). In a planar heterojunction structure (n-i-p) as shown in Figure 2b,^[66] a compact electron transport layer (ETL) of 30–50 nm of TiO₂ (most commonly) is deposited on a transparent conducting oxide substrate that can be indium-doped tin oxide (ITO) or FTO. The mesoporous TiO₂ layer is removed and perovskite light absorber is sandwiched between an ETL and a hole transport layer (HTL) by spin-coating or by vapor deposition and vapor-assisted solution process on a compact TiO₂^[32,33] layer and finally connected to a metal electrode such as Au, Ag, or Pt. Spiro-OMeTAD or poly-triallylamine (PTAA) can be used in ETL. For an inverted planar structure (p-i-n) as shown in Figure 2c,^[66] a hole transport layer of poly(3,4-ethylene dioxythiophene):poly(styrene sulfonate) (PEDOT:PSS) or NiO_x is deposited on a conducting glass substrate that is most commonly ITO followed by a photoactive perovskite light absorber layer and is further covered by an electron transport layer of [6,6]-phenyl-C₆₁-butyric acid methyl ester (PC₆₁BM) or zinc oxide (ZnO) and finally to a metal electrode of Au, Ag, or Al. The electron and holes are generated in the photoactive perovskite layer on absorption of photons of incident light and move to the opposite electrodes constituting current. HTL is used to receive the holes generated in the perovskite layer and transports them to the surface of the metal electrode whereas ETL transports electrons, blocks holes, and inhibits the electron–hole recombination in the FTO conductive substrate. The material used in ETL must be a n-type semiconductor with high carrier mobilities, transparent to light, and with a suitable energy band structure matching with that of the perovskite material. ETL must have lowest unoccupied molecular orbital (LUMO) and highest occupied molecular orbital (HOMO) higher than the photoactive perovskite layer while HTL can facilitate hole motion only if the HOMO matches with the valence band of the perovskite material. The inverted planar structure has an operational edge over a conventional structure as it required a temperature of 300 °C for device fabrication in contrast to a planar heterojunction structure where a temperature up to 500 °C is required. Moreover, the hysteresis effect of perovskite solar cells is rarely observed in a planar inverted structure while this effect is most commonly observed in planar heterojunction devices.^[68] The highest device performance has been observed with the planar heterojunction structure using TiO₂ as an electron transport layer.^[69] The most commonly reported structure is inverted planar device PEDOT:PSS/light absorber/PCBM as it is easily fabricated and more cost effective.^[68,70] The poor SPCE of inverted planar structure may be due to a barrier at the contact interface between Fermi level of the metal electrode and lowest unoccupied molecular orbital of the ETL.^[126] In a planar heterojunction structure, the expensive HTL of Spiro-OMeTAD may be removed leading to a new device framework known as planar HTM-free architecture^[71,72] as shown in Figure 2d.^[66]

4. Why Lead-Free?

The use of organic–inorganic lead halide perovskite such as MAPbI₃ and FAPbI₃ has caused an increase in solar power conversion efficiencies from 3.8% in 2009^[28] to 22.1%^[34,35,73–76] in last nine years as these materials do possess requisite optoelectronic features such as a direct bandgap, long charge carrier lifetime, diffusion length, high charge carrier mobility, and strong optical absorption coefficient.^[77–90] Lead halide perovskite has high open-circuit voltages due to photon recycling as a result of which they have long charge extraction lengths through multiple absorption–emission events within the perovskite active layer.^[91] The metal lead has invaluable intrinsic properties like high melting point, high density, malleability, ductility, corrosion resistance, etc. Despite having all characteristic features to be exploited in commercial PV solar market, it is the toxic nature of lead in lead halide perovskite solar cells that hinders its use in silicon-dominated PV market. The stringent directives of European Union clearly prohibit the use of hazardous substance in electrical and electronic equipment and lead has been identified as one of the ten hazardous chemicals listed by ROHS in order to avoid its exposure to environment and people as well.^[92,93] The toxicity of lead is due to its affinity for bond formation with thiol and cellular phosphate groups of numerous enzymes, proteins, and cell membranes.^[94] Lead halide perovskite solar cells do contain a considerable portion of lead, that is, 33% by weight. Lead is carcinogenic in nature and has no safe threshold limit of exposure. It can cause serious toxicological implications on human beings leading to cardiovascular and development diseases by inflicting the functioning of liver, kidney, brain, and central nervous system. Exposure to lead can produce irreversible health damages in infants and pregnant ladies.^[95–97] Also, organic–inorganic lead halide perovskites are liable to degradation under moisture, rain, heat, and prolonged illumination in air.^[98–100] Therefore, instability is another prime issue linked with these materials that reduces their working life span which is the most important prerequisite for commercialization on large scale as PV panels are generally placed over roof tops or in open fields so their exposure to rain is inevitable.

Hailegnaw et al. have reported that in case of a catastrophic failure of a solar plant, the impact of rain of different pHs on MAPbI₃ films is complete degradation of perovskite material leaving behind PbI₂ in water in the order of 10^{−8} mol L^{−1} which is of course low but higher than that of CdTe, CdS, and PbS values varying from 10^{−27} to 10^{−34} so it becomes most probable that lead, being soluble in water, may leech into the underground water resources.^[101] Not only this, Hailegnaw et al. have analyzed the impact of leaching lead out of the damaged solar panels on the soil and reported that the leakage of lead due to broken encapsulation or sealing will induce the concentration of Pb in first cm of ground below the damaged solar panel by 70 ppm.^[101] Taking into consideration the repercussions of use of toxic lead halide perovskites, it becomes pertinent to investigate lead-free perovskite materials providing better stabilities with solar power conversion efficiencies without compromising human health and environment.

5. Characteristic Features of Lead-Free Perovskites

The perovskite based materials used in solar cells do possess such a structure that enables them to have most suitable optical bandgaps to act as a light absorber. These materials do possess a high dielectric constant, long diffusion length, and a broad optical absorption range covering the entire visible spectrum and into the infrared. Perovskite materials exhibit ambipolar properties that enable them to display both n-type and p-type behavior on exposure to photons of incident light. The rate of nonradiative recombination in such material is strongly suppressed that is essential for high solar power conversion efficiencies. The presence of hysteresis loss in these materials clearly indicates the presence of magnetic properties at room temperature or above. Another important characteristic of these materials is that they are deposited by low-temperature solution methods that provide easy fabrication with low production cost. Besides they are typically flexible, light weight, and semitransparent making them more appealing for use in photovoltaic applications.

The lead-based halide perovskites have reported a highest solar power conversion efficiency of 22% up to now within 8 years of research.^[102] The efficiency limit of perovskite solar cell has been envisaged to be 31% based on detailed balance calculations much closer to the Shockley–Queisser limit

of 33%.^[103] Although the lead-based halide perovskites have all the structural, optical, and electrical features for use in perovskite solar cell as a light absorber but due to toxicity issues of lead, it is pertinent to replace it by another suitable elements such as tin, germanium, bismuth, etc. The lead-free perovskites have attracted the attention of the researchers at present time due to significant properties of these materials that can be engineered to make them suitable for their use as light absorbers in perovskite solar cells. Lead-free perovskite methylammonium tin iodide MASnI₃ is a direct gap semiconductor with an optical bandgap of 1.3 eV^[104–106] which is close to 1.5 eV of MAPbI₃. It exhibits a strong photoluminescence emission corresponding to the onset at 950 nm in 700–1000 nm range of the absorption edge at room temperature. MASnI₃ has an electrical conductivity of $5 \times 10^{-2} \text{ S cm}^{-1}$ at room temperature that corresponds to a Seebeck coefficient of $\approx -60 \mu\text{V K}^{-1}$. The material exhibits a carrier concentration of the order of $\approx 1 \times 10^{14} \text{ cm}^{-3}$ having excellent electron mobilities of the order of $\approx 2000 \text{ cm}^2 \text{ V}^{-1} \text{ s}^{-1}$ and hole mobility of $300 \text{ cm}^2 \text{ V}^{-1} \text{ s}^{-1}$ in comparison to lead halide perovskites that have an electron mobility of $66 \text{ cm}^2 \text{ V}^{-1} \text{ s}^{-1}$ and hole mobility of $105 \text{ cm}^2 \text{ V}^{-1} \text{ s}^{-1}$.^[84] **Table 3** summarizes the electron and hole mobilities of all the lead-free perovskite materials. The Hall measurements of as-grown crystals of MASnI₃ have revealed a hole concentration of about $9 \times 10^{17} \text{ cm}^{-3}$ with a hole mobility of about $200 \text{ cm}^2 \text{ V}^{-1} \text{ s}^{-1}$ at 250 K.^[107]

Table 3. Charge carrier mobility of lead-free perovskites.

Light absorber	Architecture	Measurement method	Component	Mobilities [$\text{cm}^{-1} \text{ V}^{-1} \text{ s}^{-1}$]	Ref.
MASnI ₃	Poly c	Hall	Electron	2320	[105]
MASnI ₃	Poly c	Hall	Hole	322	[105]
MASnI ₃	Single c	Hall	Hole	200	[107]
MASnI ₃	Poly c	Hall	Hole	50	[121]
MASnI ₃	Mesostructural	THzC	Total	1.6	[120]
FASnI ₃	Poly c	Hall	Electron	103	[105]
FASnI ₃	Film	THzC	Total	22	[122]
CsSnI ₃	Poly c	Hall	Electron	536	[105]
CsSnI ₃	Poly c	Hall	Hole	585	[123]
(C ₆ H ₅ C ₂ H ₄ NH ₃) ₂ SnI ₄	Film	FET	Hole	0.6	[124]
PEASnI ₄	Film	FET	Hole	15	[125]
(MA) ₃ Sb ₂ I _x Br _{9-x}	Single c	SCLC	Electron	12.3	[116]
(MA) ₃ Sb ₂ I _x Br _{9-x}	Single c	SCLC	Hole	4.8	[116]
Ba ₂ BiTaO ₆	Film	Hall	Hole	30	[126]
MASnI ₃	Mesostructural	–	Electron	2000	[106]
MBI	Single c	Hall	Total	1–11	[127]
(MA) ₃ Sb ₂ I ₉	Single c	SCLC	Hole	4.8	[116]
(MA) ₃ Sb ₂ I ₉	Single c	SCLC	Electron	12.3	[116]
(MA) ₃ Sb ₂ I ₉	Film	SCLC	Hole	1.2×10^{-4}	[116]
(MA) ₃ Sb ₂ I ₉	Film	SCLC	Electron	1.5×10^{-4}	[116]
Cs ₂ SnI ₆	Poly c	Hall	Hole	310	[115]
MA ₃ Bi ₂ I ₉	Single c	SCLC	Hole	29.7	[128]
MA ₃ Bi ₂ I ₉	Single c	Hall	Electron	1	[127]
(MA) ₂ SnI ₆	Poly c	Hall	Electron	3	[129]

Although tin halide perovskite has higher charge carrier mobilities, Sn^{2+} has a strong tendency to get oxidized to Sn^{4+} causing a p-type self-doping.^[108] The artificial hole doping of the halide-based perovskites increases their electrical conductivity and they exhibit a metal-like conducting behavior.^[107] The formamidinium tin iodide (FASnI_3) has an optical bandgap of 1.41 eV that is much closer to the bandgap 1.5 eV of MAPbI_3 making it a potential candidate to display an optical absorption up to 950 nm.^[109] The cesium tin iodides (CsSnI_3) display a bandgap of ≈ 1.3 eV at 300 K close to the optimum value of 1.5 eV for photovoltaic performance.^[110] Bismuth-based halide perovskites display lower light absorption onset at 450 nm with absorption coefficient of $\approx 1 \times 10^5 \text{ cm}^{-1}$ that are lower as compared to MAPbI_3 that has an absorption coefficient of around $2 \times 10^5 \text{ cm}^{-1}$ at 450 nm.^[111]

Lead-free perovskites have high exciton binding energies that provide them stable optical properties. The exciton binding energies of bismuth-based halide perovskites $\text{MA}_3\text{Bi}_2\text{I}_9$, $\text{Cs}_3\text{Bi}_2\text{I}_9$, and $\text{MA}_3\text{Bi}_2\text{I}_9\text{Cl}_x$ are of 70, 270, and 300 meV that are much higher than that of lead-based halide perovskites (25–50 meV).^[111] UV–vis absorption measurements for $\text{Cs}_3\text{Bi}_2\text{I}_9$ have reported a strong exciton absorption peak at room temperature. $\text{Cs}_3\text{Bi}_2\text{I}_9$ exhibits an exciton absorption peak at ≈ 485 nm (2.56 eV) with an indirect optical bandgap of ≈ 2.1 eV. The films exhibited an optical absorption coefficient of $\approx 1 \times 10^4 \text{ cm}^{-1}$ at 450 nm. In spite of indirect bandgaps, the material is still a potential candidate for use as a light absorber due to strong exciton binding energy.^[112] CsSnI_3 perovskite exhibits a direct bandgap of 1.32 eV with an exciton binding energy of 18 meV at room temperature. The large binding energy is on the account of exciton motion in the 2D layer of SnI_4 tetragons present in the material.^[123]

Tin-based perovskites are prepared by using solution methods and crystallizes at room temperature whereas lead-based perovskites crystallize by heating. The variation in composition of halide anion in lead-free perovskites has a significant effect on the absorption coefficient of these materials thus paving the way for engineering the bandgaps and optical absorption spectrum of these materials. The tin-based hybrid halide perovskites $\text{MASnI}_{3-x}\text{Br}_x$ ($x = 0, 1, 2, 3$) synthesized in an inert atmosphere in the nitrogen glove box exhibit an optical absorption onset that can be blueshifted from 954 to 577 nm by varying the composition of halide anion, that is, for $x = 0$ and $x = 3$ whereas for $x = 1$ and 2, optical absorption onset at 795 and 708 nm has been reported. Also ultraviolet photoelectron spectroscopy (UPS) measurements of valence band energy E_{VB} of $\text{MASnI}_{3-x}\text{Br}_x$ under high vacuum have revealed that the bandgaps can be engineered from 1.30 eV for MASnI_3 to 2.15 eV for MASnBr_3 .^[106] Not only this, the color of the tin-based hybrid halide perovskite $\text{MASnI}_{3-x}\text{Br}_x$ shows a variation with increased bromine content from black ($x = 0$) to dark brown ($x = 1$) and yellow ($x = 3$); thus, colorful solar devices can be designed by using bandgap engineering. Thus, the composition of tin-based mixed halide perovskite can be tailored to emit between 954 and 574 nm in contrast to lead-based counterparts that display photovoltaic emission in between 700 and 800 nm. The emitted wavelengths are in agreement with the values of bandgaps obtained through experiments clearly indicating the presence of direct optical bandgaps in MASnI_3 .^[106]

The investigation of Ge mixed halide perovskites $\text{MAGeI}_{3-x}\text{Cl}_x$ [$x = 0, 1, 1.5, 2, 3$] by using first principle calculations has reported a bandgap of 1.8 eV for MAGeI_3 ($x = 0$) whereas MAGeCl_3 ($x = 3$) has a much wider bandgap of 3.8 eV clearly demonstrating the effect of doped chlorine in MAGeI_3 perovskites. The absorption coefficients also display an increasing trend when the proportion of x decreases from 3 to 0 attributed to the redshift of the optical bandgap caused due to change in chemical composition of the material.^[113] In case of antimony-based mixed halide perovskites $\text{MA}_3\text{Sb}_2\text{I}_x\text{Br}_{9-x}$, the optical bandgap onset for perovskite films shows a decreasing trend, that is, the optical absorption onset is blueshifted from 558 to 453 nm as x changes from 9 to 0. The hole and electron mobilities of $\text{MA}_3\text{Sb}_2\text{I}_9$ single crystals have been calculated by using space charge limited current methods^[114,115] and are shown in Table 3. The $\text{MA}_3\text{Sb}_2\text{I}_9$ single crystals have high absorption coefficient greater than 10^5 cm^{-1} at absorption peak wavelengths. The absorption onset for [$x = 0, 3, 6$] in $\text{MA}_3\text{Sb}_2\text{I}_x\text{Br}_{9-x}$ films are 453, 486, and 516 nm with a direct bandgap of 2.78, 2.66, and 2.49 eV, respectively.^[116] Lead-free perovskites do possess suitable carrier diffusion lengths and minority charge carrier lifetimes exhibiting photovoltaic performance. The long carrier diffusion lengths of electrons and holes in MASnI_3 are 279 ± 88 and 193 ± 46 nm, respectively, obtained by broadband transient absorption and time-resolved fluorescence spectroscopy. Addition of SnF_2 in MASnI_3 films results in not only increase in diffusion lengths to more than 500 μm but also enhances the fluorescence lifetime up to ten times.^[117] The background concentration of doped holes has an effect on the diffusion lengths of MASnI_3 perovskite. As the background doping level in MASnI_3 decreases, there is a corresponding increase in diffusion length. For a doping concentration below 10^{15} cm^{-3} , the diffusion length can be engineered to increase above 1 μm in length that is close to the value shown by lead-based halides.^[120] Lead-free CsSnI_3 perovskite films synthesized by the solution method have carrier lifetime of ≈ 54 ps, minority carrier diffusion length of ≈ 1.6 nm, and a doping concentration of more than $9.2 \times 10^{18} \text{ cm}^{-3}$ obtained as a consequence of better quality of crystalline films whereas single crystals of CsSnI_3 have a long minority carrier diffusion length of more than 930 nm which is comparable to that of the lead-based perovskites^[110] having diffusion lengths exceeding 1 μm .^[74]

6. Hole Transport Material and Electron Transport Material in Lead-Free Perovskite Solar Cells

Lead-free perovskites have been prepared by using mesoporous perovskite solar cells in planar heterojunction and inverted planar structures. Spiro-OMeTAD is most commonly used hole transport material in lead-free perovskites as it has the ability to penetrate deep into the pores of the perovskite layer but it has a low hole mobility and complicated device processing. Also it deteriorates the stability of the fabricated device.^[130,131] Therefore, dopants are added into it in order to enhance its conductivity. The first lead-free perovskite device was prepared by solvent engineering method by employing MASnI_3 as a light absorber. Spiro-OMeTAD has been used as

a HTM on the top of the perovskite layer in a device architecture of FTO/compact TiO₂/mesoporous TiO₂ layer/MASnI₃ light absorber/Spiro-OMeTAD/Au.^[120] An additive doping of hydrogen bis(trifluoromethane sulfonyl)imide (H-TFSI) and *tert*-butyl pyridine is done into Spiro-OMeTAD to enhance the rate of hole extraction and transport.^[132] The additive doping of lithium bis(trifluoro methyl sulfonyl)imide salt (Li-TFSI) and 4-*tert*-butyl pyridine (TBP) deteriorates the stability of MASnI₃ perovskite device than H-TFSI.^[120] In another approach, also Spiro-OMeTAD used as a HTM is doped with lithium bis(trifluoro methyl sulfonyl)imide and 2,6-lutidine in order to enhance its hole mobility.^[49] The solar cell capacitance simulator and analytical calculations (SCAPS) have reported an efficiency of above 15% in lead-free tin-based MASnI₃ perovskites employing Spiro-OMeTAD as a hole transport material.^[133] Chlorobenzene (CB), Li-TFSI, and TBP have been used as an additive in Spiro-OMeTAD in lead-free Ma₃Bi₂I₉ perovskites.^[111] Oxygen-doped Spiro-OMeTAD employed as a HTM in Cs₃Bi₂I₉ perovskite solar device has yielded the maximum of the reported solar power conversion efficiencies.^[134] The Spiro-OMeTAD as a HTM has been used in lead-free tin, germanium, antimony, bismuth, and copper-based perovskite devices. **Figure 3** shows the scanning electron microscopy (SEM) image of a MASnI₃ perovskite device with Spiro-OMeTAD as a HTM.^[106]

Cu-based lead-free perovskites reported so far have a planar heterojunction (n-i-p) structure employing Spiro-OMeTAD as a HTM with a highest reported efficiency of 2.41%. The low efficiency is attributed to the mismatch in the energy levels between the (MA)₂CuCl_xBr_{4-x} and Spiro-OMeTAD as a HTM leading to a poor hole extraction in the device.^[135-137] Another polymeric organic HTM PTAA has been employed in planar heterojunction n-i-p perovskite devices.^[138,139] Owing to its large hole mobility the use of PTAA as a HTM in Cs₃Sb₂I₉ perovskite solar cells has reported a V_{OC} of 250–300 meV and an extremely low solar power conversion efficiency.^[140] The doping of bismuth-based perovskite Cs₃Bi₂I₉ films with N,N-dimethyl formamide/hydroiodide (HI) solution featured a pure crystalline film with an excellent thermal stability.^[141] PTAA employed as a HTM in ethylene diammonium and methylammonium tin iodide en[MASnI₃] has reported a SPCE of 6.63% with a very high current density of 24.3 mA cm⁻² in a device architecture of FTO/C-TiO₂/mp-TiO₂/en[MASnI₃]/PTAA/Au.^[142]

Many research groups have synthesized lead-free MASnI₃, FASnI₃, and CsSnI₃ perovskite solar devices by using PTAA as a HTM. The presence of another polymeric organic poly(3-hexyl thiophene) (P3HT) as a HTM in lead-free perovskites can enhance the SPCE as well as stability of the fabricated device due to its potential to decrease the resistance from the hole transfer impedance. P3HT has been employed as a HTM instead of Spiro-OMeTAD for Cs₃Bi₂I₉ perovskite solar devices.^[111] In another research, P3HT is used as a HTM in thin films of CsBi₃I₁₀ perovskite deposited by solution processing in device architecture of glass/FTO/compact TiO₂/mesoporous TiO₂/CsBi₃I₁₀ light absorber/P3HT/Ag. The addition of dopant 4-*tert*-butyl pyridine in Spiro-OMeTAD employed as a HTM in CsBi₃I₁₀ perovskite dissolves the light absorbing perovskite layer^[143] and suffers from stability and degradation issues. Unlike Spiro-OMeTAD, P3HT enhances the SPCE of the fabricated perovskite device as in CsSnBr₃ films, an efficiency of 0.11% was enhanced to 3.2% by replacing Spiro-OMeTAD HTM by P3HT.^[144] Also, P3HT employed as a HTM in MA₃Bi₂I₉ films enhance the overall performance of the fabricated device.^[127] P3HT has been employed as a HTM in MASnBr₃, FASnI₃, CsSnI₃, en[MASnI₃], Cs₂SnI₆, MA₃Bi₂I₉, Cs₃Bi₂I₉, CsBi₃I₁₀, AgBi₂I₇, and AgBiI₅ perovskite solar devices.

In an inverted planar (p-i-n) perovskite device, the hole transport layer is kept under the perovskite light absorber layer that alleviates the stringent requirement of efficient conductivity of hole transport material. Polymeric organic HTM PEDOT:PSS is used in such devices. PEDOT:PSS is used as a HTM in FASnI₃ perovskite solar cells in an inverted planar (p-i-n) architecture and at present has reported a maximum SPCE of 8.12% in FA_{0.75}MA_{0.25}SnI₃ in lead-free tin-based perovskite with a V_{OC} of 0.61 V.^[145] The PEDOT:PSS with intercalated polyethylene glycol (PEG) used as a HTM in FASnI₃ perovskite solar cell alleviates the energy level mismatch between the perovskite light absorber and PEDOT:PSS as HTM. As a consequence, the SPCE increased from 2.01 to 5.12% in the forward scan.^[146] The inverted planar (p-i-n) device structure employed for antimony-based MA₃Sb₂I₉ perovskite films has reported a SPCE of 0.5% with a V_{OC} of 0.89 V.^[147] Additives are added into PEDOT:PSS in order to enhance the conductivity and morphology of PEDOT:PSS films. Polyorganic solvents such as dimethyl sulfoxide (DMSO), dimethylformamide (DMF), and ethylene

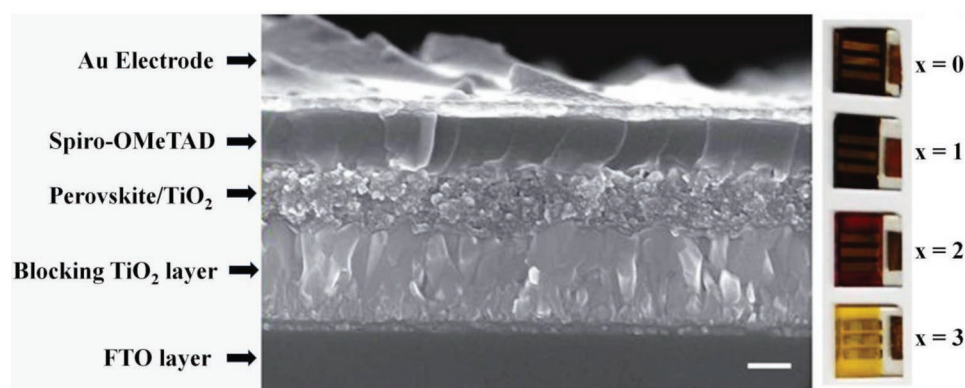


Figure 3. SEM image of a photovoltaic device using CH₃NH₃SnI₃ perovskite material. Reproduced with permission.^[106] Copyright 2014, Springer Nature.

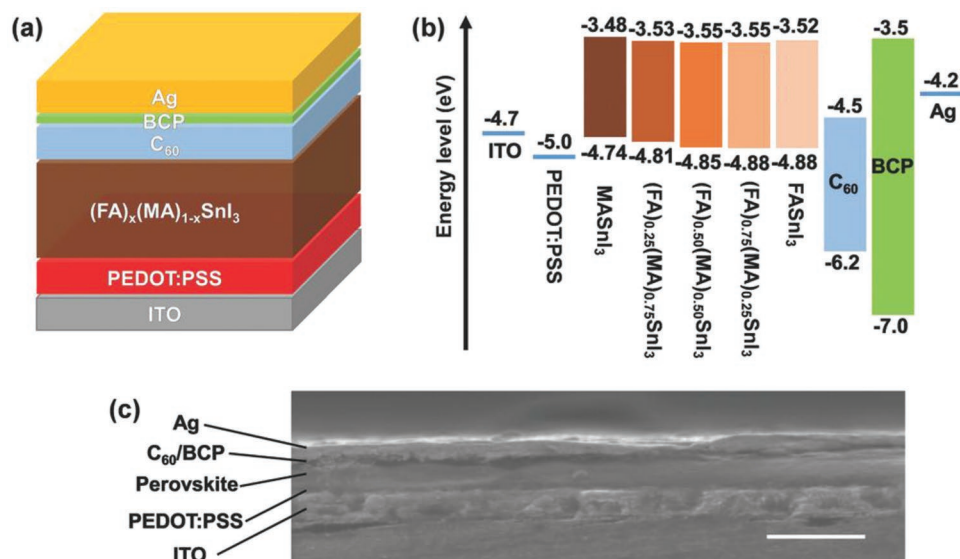


Figure 4. a) Schematic device structure of (FA)_x(MA)_{1-x}SnI₃ perovskite solar cell. b) Band alignment diagram. c) Cross-sectional scanning electron microscope (SEM) image of a completed device (scale bar: 500 nm). Reproduced with permission.^[150] Copyright 2017, Wiley-VCH.

glycol have been used as additives in lead-free perovskite device fabrication.^[148] The addition of additive in PEDOT:PSS films leads to enhancement in efficient hole extraction and collection rate attributed to the strong dipole–dipole or dipole–charge interactions between the polar additive and PEDOT:PSS used as a HTM in fabricated perovskite device.^[149] PEDOT:PSS as a HTM has been employed in lead-free MASnI₃, FASnI₃, FASnI₃Br, FA_{1-x}MA_xSnI₃, MA₃Bi₂I₉, MA₃Sb₂I₉, and Cs₃Sb₂I₉ reported perovskite solar devices. **Figure 4** shows the device structure and energy band diagram of (FA)_x(MA)_{1-x}SnI₃ perovskite solar cell.^[150] The use of Spiro-OMeTAD as a HTM damages the perovskite film. In order to overcome this issue, inverted planar (p-i-n) perovskite solar cells of MASnI₃ have been prepared by using PEDOT:PSS doped with poly-TPD as a HTM as shown in **Figure 4**.^[150] **Figure 4** shows the (a) schematic device structure of (FA)_x(MA)_{1-x}SnI₃ perovskite solar cell, (b) band alignment diagram, and (c) cross-sectional SEM image of a completed device (scale bar: 500 nm).^[150] Addition of poly-TPD layer into PEDOT:PSS resulted into suppressed charge recombination and better efficiencies.^[151]

Besides organic HTMs, inorganic NiO (nickel oxide) and CuI (copper iodide) have also been used as a HTM in inverted planar (p-i-n) structures. NiO has a large work function of 5.2 eV in comparison to 5.2 eV for PEDOT:PSS that makes it viable for use as a HTM in perovskite solar cells reporting a higher V_{OC}.^[152–155] The thickness and morphology of NiO as a HTM has a direct impact on charge collection and recombination in perovskite solar devices. The use of NiO as a HTM leads to more air stability in FASnI₃ perovskite inverted planar (p-i-n) solar cell using (PEA)₂FA₈Sn₉I₂₈ as a light absorber reporting a SPCE of 5.94%.^[156] NiO_x has been employed as a HTM instead of Spiro-OMeTAD in inverted planar structured B-γ-CsSnI₃ PSCs in order to overcome the low conductivity of the undoped Spiro-OMeTAD. The perovskite device exhibited an enhanced SPCE of 2.61% higher than that of Spiro-OMeTAD used as a HTM.^[157] **Figure 5** shows the device structure and

corresponding energy diagram employing NiO_x as a HTM in B-γ-CsSnI₃ perovskite solar cells.^[157]

CuI has a hole conductivity greater than that of Spiro-OMeTAD that enables CuI to improve the fill factor (FF) of the perovskite device employing it as a HTM.^[158] CuI has been used as a HTM in fabrication of CsSnI₃ perovskite solar cells reporting a V_{OC} of 0.55 V and enhanced air stability.^[159] **Figure 6** shows the device architecture of CsSnI₃ using CuI as a HTM and SEM image of CsSnI₃ films.^[159]

Perovskite solar cells without a HTM layer have the advantage of having simple structures, easy fabrication process, and higher stability if the work function of the metal electrode used in perovskite solar cells is close to the maximum valence band of perovskite light absorber, then absence of hole transport layer has no impact on the built-in electric field.^[160] The perovskite material in HTL-free devices works as a light absorber and a hole transport layer in such cells.^[161] A HTL-free solar cell of MASnI₃ has reported an efficiency of 3.15%, J_{SC} of 21.4 mA cm⁻² that has been prepared through a solvent engineering method having a device architecture of the form FTO/c-TiO₂/mp-TiO₂/MASnI₃ light absorber/Au.^[162]

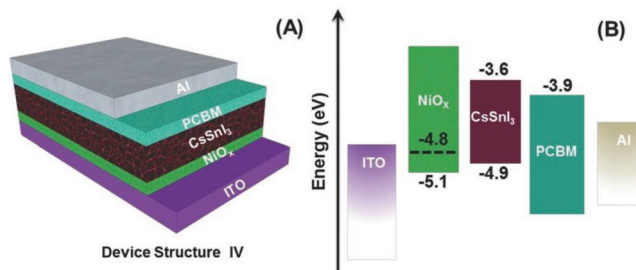


Figure 5. A) Scheme of the “inverted” structure planar B-γ-CsSnI₃ PSC device employing NiO_x as HTL and PCBM as ETL, and B) corresponding energy level diagram (the dashed line indicates NiO_x work function). Reproduced with permission.^[157] Copyright 2016, Wiley-VCH.

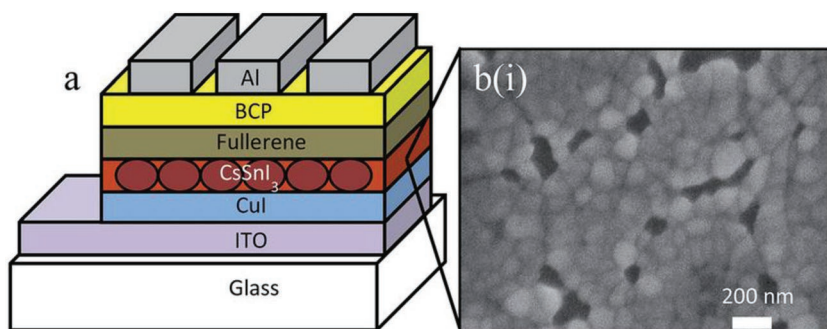


Figure 6. a) Schematic of the device architecture used in this work; b) SEM image of a CsSnI_3 film prepared with a 10 mol% excess SnI_2 and spin cast at 4000 rpm from 8 wt% solution onto an ITO glass substrate coated with a 100 nm layer of CuI. Reproduced with permission.^[159] Copyright 2015, Royal Society of Chemistry.

HTL-free CsSnI_3 PSC has stability ten times greater than the devices using same device architecture using MAPbI_3 as a light absorber.^[163] Inorganic metal oxides like TiO_2 , ZnO , SnO_2 and organic fullerene derivatives like phenyl- C_{60} -butyric and methyl ester (PC_{60}BM) or PC_{70}BM have been employed as an ETM for perovskite solar cells. The efficient ETM should have the capability to engineer the optical bandgap for maximum absorption of incident light by the perovskite light absorber layer and must have a better electron extraction and hole blocking property in order to suppress the electron–hole recombination at the interface of the device. TiO_2 as an ETM has been employed in device fabrication of most of the reported lead-free perovskite solar cells. On the top of a mesoporous TiO_2 layer, the perovskite film of MASnI_3 is crystallized upon spin-coating and it penetrates into the pores of ETM. The MASnI_3 films fabricated on the

top of 400 nm thick mp- TiO_2 layer are better than that of prepared on an 80 nm thick mp- TiO_2 layer. The mesoporous $\text{MAPbI}_{3-x}\text{Cl}_x$ perovskite films have a better film morphology than that of MASnI_3 films fabricated in a similar way and architecture as shown in Figure 7.^[120] Figure 8 shows the schematic energy-level diagram of $\text{CH}_3\text{NH}_3\text{SnI}_{3-x}\text{Br}_x$ compounds.^[106]

By controlled crystallization, it is possible to enhance the quality of film formation.^[120] In another approach, solvent engineering method was employed to prepare thin films of MASnI_3 . A 30 nm thick TiO_2 compact layer as an ETM is deposited on the substrate by atomic layer deposition system. The perovskite light absorber crystals infiltrate into the

pores of mp- TiO_2 layer and remaining pores of mesoporous TiO_2 layer are filled up by the HTM forming a 200 nm thick capping layer on the top of the composite structure.^[106]

In a planar heterojunction (n-i-p) structure, a compact TiO_2 layer is deposited on a glass that is further covered by a mesoporous TiO_2 layer in order to enhance the electron collection and to avoid hysteresis loss during V – I measurements.^[164] By employing mp- TiO_2 as an ETM, the homogenous MASnI_3 films prepared by vapor-assisted solution process^[165,166] have reported a J_{SC} of 17.4 mA cm^{-2} when used as a light absorber in perovskite solar cells. The SPCE of pristine FASnI_3 films was 0.003% by using mesoporous TiO_2 layer as an ETM. The low value of SPCE is attributed to high background carrier density of 10^{19} cm^{-3} that leads to a metal like conductivity and device short circuiting.^[156] However, the addition of Br_2 into FASnI_3

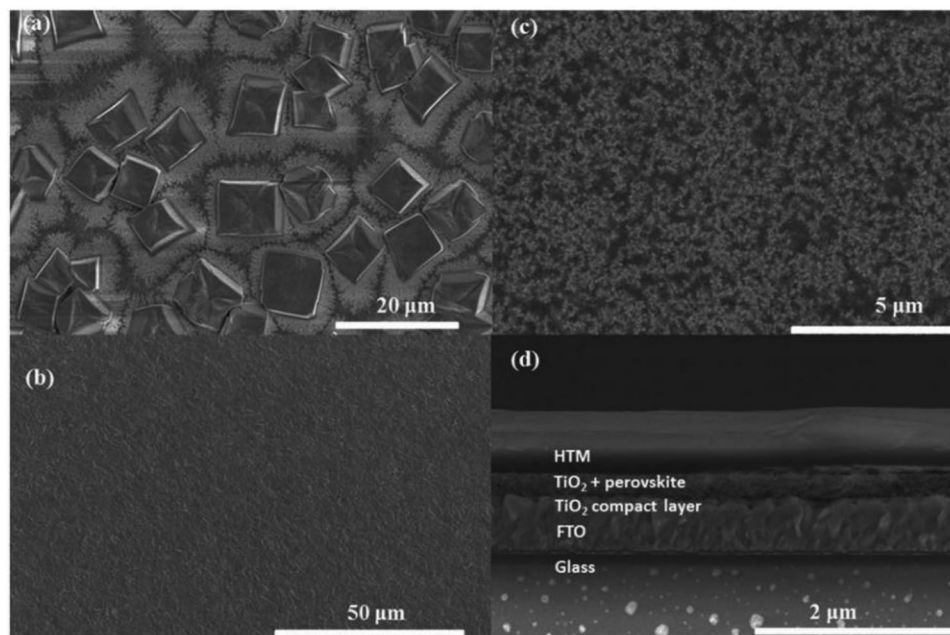


Figure 7. SEM images. a) Top view of a film of $\text{CH}_3\text{NH}_3\text{SnI}_3$ spin-coated onto mesoporous TiO_2 (80 nm thickness). b) Top view of a spin-coated film of $\text{CH}_3\text{NH}_3\text{PbI}_{3-x}\text{Cl}_x$ on mesoporous TiO_2 (400 nm thickness). c) Top view of a spin-coated film of $\text{CH}_3\text{NH}_3\text{SnI}_3$ on mesoporous TiO_2 (400 nm thickness). d) Cross-sectional view of a complete device active layer composed of FTO glass/compact TiO_2 (50 nm)/mesoporous TiO_2 infiltrated with $\text{CH}_3\text{NH}_3\text{SnI}_3$ (400 nm)/Spiro-OMeTAD (600 nm). Reproduced with permission.^[120] Copyright 2014, Royal Society of Chemistry.

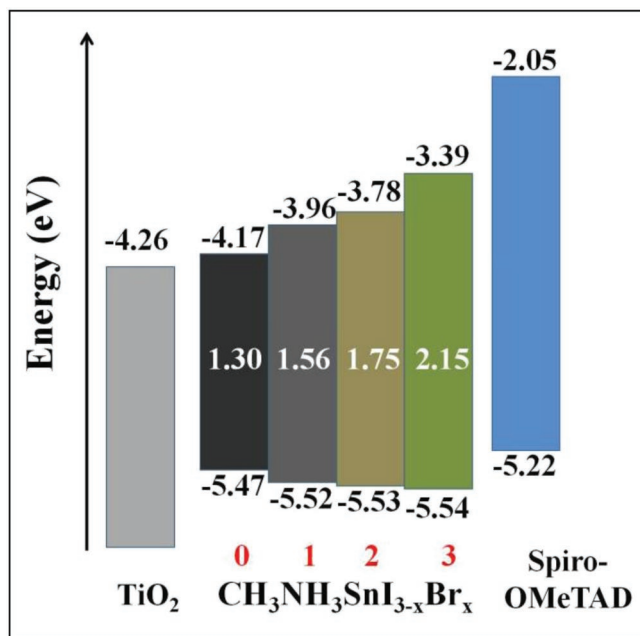


Figure 8. Schematic energy-level diagram of $\text{CH}_3\text{NH}_3\text{SnI}_{3-x}\text{Br}_x$ compounds. Reproduced with permission.^[106] Copyright 2014, Springer Nature.

films lowers the background carrier density of the perovskite. As a consequence of reduction in tin vacancies, the leakage current of the device is reduced that further increases the recombination lifetime and finally V_{OC} and FF of the fabricated device and SPCE up to 5.5%.^[167] TiO_2 as an ETM has an intrinsic low mobility and this has been a generation of deep traps by UV light that results in charge accumulation, recombination classes, and severe $V-I$ hysteresis.^[41,59,62,168,169] The evaporation-assisted method combining thermal evaporation with solution method has been employed to obtain uniform, full coverage, dense, and pinhole-free CsSnI_3 films eliminating the direct contact between HTM and ETM and reduces the consequent recombination. Evaporation-assisted solution method makes it feasible for convenient tuning of SnF_2 addition as a solvent. The conventional mesoporous n-i-p structure PSCs with an architecture $\text{FTO}/\text{bl-TiO}_2/\text{mp-TiO}_2/\text{CsSnI}_3/\text{OMeTAD}/\text{Au}$ has reported an efficiency of 2.2% in the device based on a 66 nm thickness of CsI .^[170] In CsSnBr_3 , the best reported SPCE so far is 2.1% that is due to the significant role of SnF_2 addition as a solvent that alleviates the serious mismatch of band energy levels between the perovskite light absorber and TiO_2 layer as an ETM.^[102]

Germanium-based perovskites have been fabricated by employing compact and mesoporous TiO_2 layer as ETM and Spiro-OMeTAD as a HTM. The fabrication films of CsGeI_3 and MAGeI_3 displayed a smooth morphology with a SPCE of 0.11 and 0.20% whereas that of FAGeI_3 exhibited a poor morphology leading to no photovoltaic behavior. The poor performance of the device is attributed to oxidation of Ge^{2+} into Ge^{4+} during fabrication process.^[144] However, TiO_2 requires a high-temperature sintering and exhibits degradation in SPCE on exposure to UV light. TiO_2 requires high-temperature annealing but the substrate cannot withstand such a high temperature. The

mesoporous TiO_2 (n-i-p) devices have exhibited better efficiencies whereas inverted planar (p-i-n) devices suffer from hysteresis losses. Tin-based lead-free perovskites are considered unsuitable for planar heterojunction solar cells due to their short diffusion lengths, a SPCE of 1.72% is shown by FASnI_2Br films as a light absorber with C_{60} as ETM suggesting the significance of perovskite film morphology on the device performance. FASnI_2Br films with an architecture $\text{ITO}/\text{PEDOT:PSS}/\text{FASnI}_2\text{Br}/\text{C}_{60}/\text{Ca}/\text{Al}$ reported a J_{SC} of 6.82 mA cm^{-2} and V_{OC} of 0.46 mV.^[171] **Figure 9** shows the structure of (a) FASnI_2Br (SEM image)^[171] and (b) FASnI_3 (SEM image) and energy band diagram.^[172]

Anatase, rutile, and brookite are three stable phases in TiO_2 when used as an ETM. For anatase TiO_2 -based perovskite solar cells, the electron diffusion constant was ten times higher but the time constant for recombination was ten times lower than for rutile TiO_2 -based one. Fast charge recombination in anatase TiO_2 -based device is the result of poor charge separation in TiO_2 /perovskite interface.^[173] **Figure 10** shows the MBI perovskite layer deposited on a compact, mesoporous, and brookite TiO_2 .^[174] Fullerene C_{60} and its derivatives such as PC_{60}BM or PC_{70}BM have been employed as an interfacial material at the interface between TiO_2 and perovskite layer because of its high electron mobility. A self-assembled C_{60} monolayer was introduced on TiO_2 surface that enhances the charge separation, reduces the capacitance of TiO_2 and $V-I$ hysteresis.^[175] Organic ETM of PC_{60}BM or PC_{70}BM is more efficient to collect electrons in comparison to mp- TiO_2 in inverted planar p-i-n devices as they can passivate the charge traps of metal oxide^[176–178] and hence can reduce the nonradiative recombination channels at the surface leading to an improved SPCE with a very low hysteresis.^[179,180] The perovskite layer of $\text{Cs}_3\text{Sb}_2\text{I}_9$ was prepared through a single-step spin-coating process for an inverted planar p-i-n structure using architecture $\text{glass}/\text{ITO}/\text{PEDOT:PSS}/\text{Cs}_3\text{Sb}_2\text{I}_9/\text{PC}_{71}\text{BM}/\text{C}_{60}/\text{bathocuproine (BCP)}/\text{Al}$. $\text{PC}_{71}\text{BM}/\text{C}_{60}$ is a double fullerene layer employed as an ETM to minimize the trap densities.^[181] Also, the perovskite solar cells with a p-i-n structure of $\text{ITO}/\text{PEDOT:PSS}/(\text{NH}_4)_3\text{Sb}_2\text{I}_9/\text{PC}_{61}\text{BM}/\text{Al}$ were synthesized to study the photovoltaic performance of $(\text{NH}_4)_3\text{Sb}_2\text{I}_9$ reporting a SPCE of 0.51%.^[147]

The selection of charge extraction layers by modulating a desirable energy band alignment between the conduction band edge of CsSnI_3 and LUMO of ETL is another feasible strategy. A V_{OC} of 0.55 V was reported for CsSnI_3 perovskite solar device using p-i-n structure $\text{ITO}/\text{CuI}/\text{CsSnI}_3/\text{indane-C}_{60}\text{-bisadduct ICBA}/\text{BCP}/\text{Al}$ architecture. Here, ICBA acted as an ETM.^[159] BCP is used as an interfacial material in between C_{60} derivatives and the metal electrodes. The FF was significantly improved by using electrode interfacial layer. In an inverted planar (p-i-n) FASnI_3 perovskite device, C_{60} has been employed as an ETM for efficient electron extraction.^[172] A solution gel derived ZnO used as an ETL bilayer fabricated at $<110 \text{ }^\circ\text{C}$ facilitates the improved energy level alignment and enhanced charge carrier extraction and a PCBM layer is used to reduce the hysteresis and enhance the perovskite thermal stability.

ZnO can be a potential candidate to replace TiO_2 as an ETM layer without causing a marked effect on the performance of PSCs.^[182,183] The doping of pure ZnO nanorods with Au/Al results in high electron mobility and high electron density.^[184]

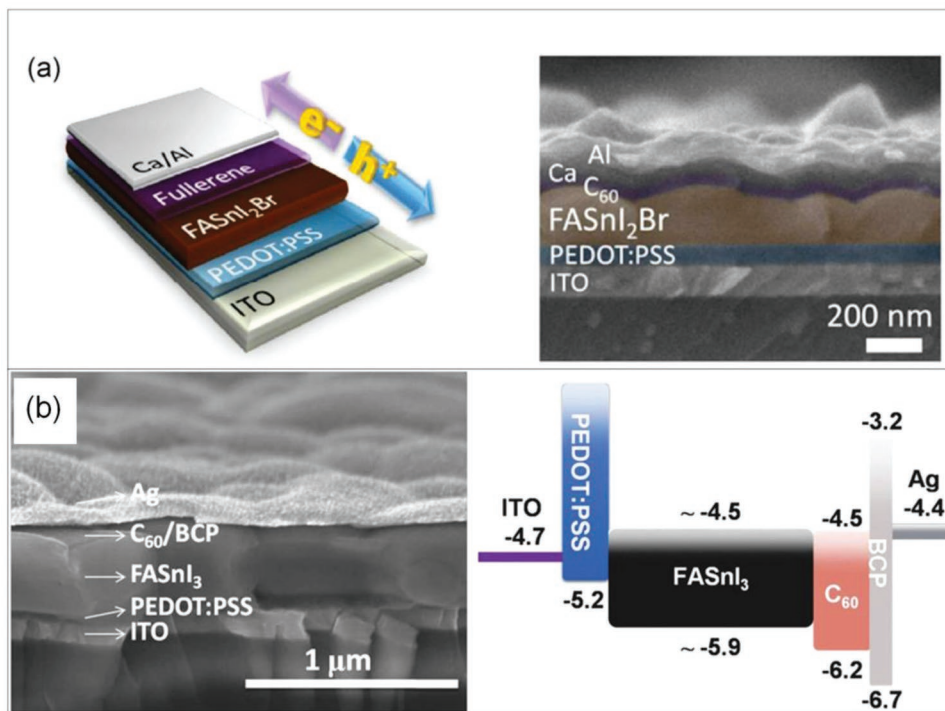


Figure 9. a) Configuration of the FASnI₂Br-based p-i-n heterojunction solar cells and its cross-sectional SEM image of a typical device. Reproduced with permission.^[171] Copyright 2016, Springer Nature. b) Cross-sectional SEM image of the entire device with 10 mol% SnF₂ additives, in which each layer is labeled, and schematic of energy level diagram of our FASnI₃ perovskite solar cells. Reproduced with permission.^[172] Copyright 2016, Wiley-VCH.

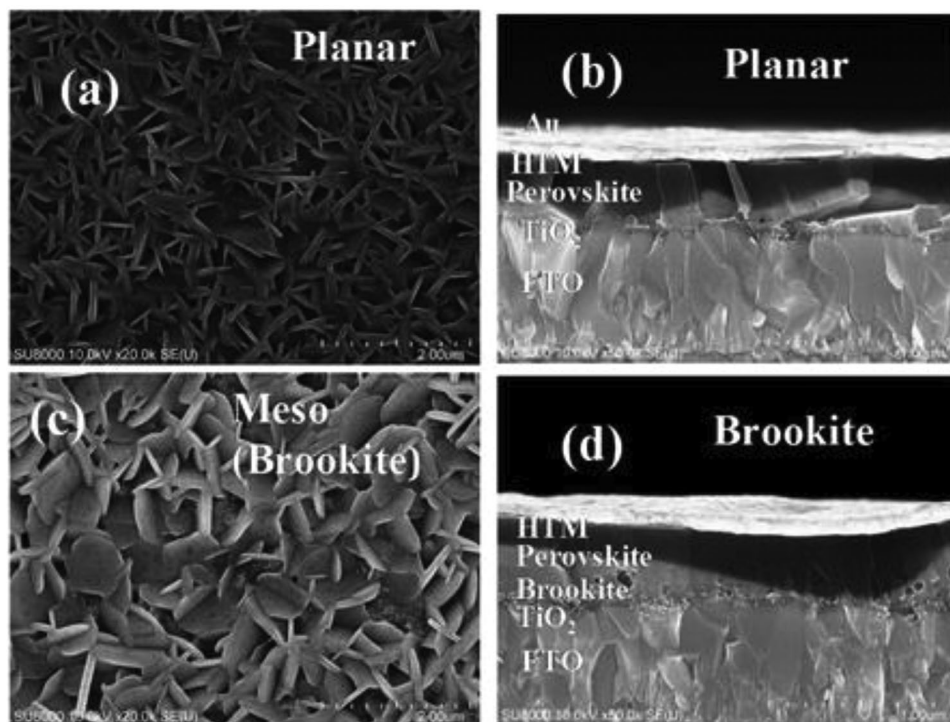


Figure 10. Top and cross-sectional SEM view of MBI perovskite layer deposited on a,b) TiO₂ compact layer and c,d) brookite mesoporous layer. Reproduced with permission.^[174] Copyright 2016, American Chemical Society.

From SCAPS-1D, the use of ZnO nanorods as an ETM and Cu₂O as a HTM for MASnI₃ perovskite devices has displayed the best performance among all the PSCs. Cu₂O is a suitable HTM layer in PSCs due to its high hole mobility and low electron affinity. The device displayed a maximum SPCE for ZnO nanorods/MASnI₃/Cu₂O structure exhibiting a J_{SC} of 32.26 mA cm⁻², V_{OC} of 0.85 V, FF of 0.74, and SPCE of 20.23%.^[185] The ETM used in a perovskite solar cell has a significant impact on the SPCE of the device when bl-TiO₂ layer in Ag₂Bi₃I₁₁ is replaced by bl-SnO₂, there is a significant increase in current density from 1.33 mA cm⁻² (TiO₂) to 2.31 mA cm⁻² (SnO₂) attributed to better electron extraction by SnO₂ ETM.^[186]

7. Lead-Free Perovskites

7.1. Tin-Based Perovskites

Tin is the most suitable candidate for substitution of lead for lead-free perovskite solar cell because of its similar valence electronic configuration as that of lead and approximate same ionic radius of Sn²⁺ (115 pm) as that of Pb²⁺ (119 pm). It has lower value of electronegativity Sn²⁺ (1.96) than that of Pb²⁺ (2.33).^[237] Tin-based perovskites have optical bandgap of 1.2–1.6 eV most suitable for their use as light absorbers, large carrier mobilities, and low exciton binding energies of 18 meV.^[105,119,187] Tin-based perovskites are represented by the general formula ASnX₃ where A can be MA⁺, Fa⁺ or Cs⁺ cation, and X is a halogen anion.

Methylammonium tin halides MASnX₃ have a direct bandgap of 1.20–1.35 eV, electron mobility of 2320 cm² V⁻¹ s⁻¹, hole carrier mobility of 322 cm² V⁻¹ s⁻¹,^[105,188] and long charge carrier diffusion length of more than 500 nm.^[117] The first completely lead-free Sn-based perovskite MASnI₃ was processed on a mesoporous TiO₂ scaffold that achieved SPCE of 8.4% under 1 sun illumination in a highly inert atmosphere in a glove box with V_{OC} of 0.88 V, J_{SC} of 16.8 mA cm⁻², and FF of 0.42 obtained from material having optical bandgap of 1.23 eV.^[120] A Sn-based perovskite model with the novel architecture of glass/ZnO:Al/TiO₂/CH₃NH₃SnCl₃/Cu/Au, devised by Mandadapu et al.,^[189] has been analyzed by using the solar cell capacitance simulator (SCAPS-ID), with the predicted parameters such as thickness 0–6 μm, defect density of 10¹⁴ cm⁻³ of light absorber layer, and bandgap 1.3 eV. The model achieved a SPCE of 24.82%, V_{OC} of 1.04 V, J_{SC} of 3.50 mA cm⁻², and FF of 0.78. The excellent results of this model clearly signify the enormous potential of Sn-based perovskites for their efficient use in solar cells. Since then an extensive work has been carried out on preparation and characterization of Sn-based perovskites material to examine their structural, optical, and charge transport abilities for efficient use as light absorber in perovskite solar cells.^[188] The perovskite solar cells with CH₃NH₃SnBr₃ as light absorber reported a SPCE of 0.35% for coevaporation and 0.12% for sequential deposition method.^[190] The composition of a halide anion in mixed halide tin-based perovskites has an influence on the photovoltaic performance exhibited by them. The mixed halide tin-based perovskite MASnI_{3-x}Br_x was investigated by altering the Br⁻/I⁻ ratio, it was reported that MASnBr₃

as a light absorber displays more V_{OC} (0.88 V) and less J_{SC} (8.26 mA cm⁻²) in comparison to MASnIBr₂ having V_{OC} (0.82 V) and J_{SC} (12.33 mA cm⁻²). Among all MASnI_{3-x}Br_x perovskites, MASnIBr₂ has the highest reported SPCE of 5.73% under stimulated full sunlight.^[98] Also, the position of band edge of mixed halides perovskites, MASnI_{3-x}Br_x can be tuned from 954 nm (MASnI₃) to 577 nm (MASnBr₃) thus displaying a remarkable tunability of color. Also the mixed halides tin-based perovskites MASnIBr_{2-x}Cl_x has been fabricated for carbon-based mesoscopic cells devoid of ETM and HTM layers by varying the composition of SnCl₂/SnBr₂. The solar device with MASnIBr_{1.8}Cl_{0.2} achieved the best photovoltaic performance of 3.11% with a long-term stability in air. The device exhibited excellent charge recombination and dielectric relaxation properties.^[191] However, tin-based perovskites have low values of SPCE due to fast oxidation of divalent Sn²⁺ into a more stable state Sn⁴⁺ and easy formation of Sn vacancies due to small value of formation energy. As a consequence of it, there is a large charge carrier recombination and high levels of self p-doping in Sn-based perovskites films. Thus, a lot of research has been carried out to suppress oxidation of divalent Sn²⁺. SnF₂ has been added to such films to inhibit the oxidation process so as to reduce the background carrier hole density by filling Sn vacancies. The entire fabrication process is carried out in an inert atmosphere in the glove box encapsulated by hot melt polymer film, a glass cover slide with sealed edges so as to avoid the oxidation of perovskite film on exposition to ambient air that could cause its fast degradation. Addition of 5-ammonium valeric acid iodide to MASnI₃ suppressed oxidation of Sn²⁺ for better stability of the perovskite device.^[192] Hypophosphorous acid was also used for reducing the oxidation of divalent Sn²⁺ thereby reducing the number of Sn vacancies and charge carrier density. As a consequence of it, there is enhancement in charge recombination lifetime by fourfold than that of the control device.^[193]

A SPCE of 2.14% was reported for a perovskite solar cell having MASnI₃ with SnF₂ additive as a light absorber. The fabricated device achieved V_{OC} of 0.45 V, J_{SC} of 11.48 mA cm⁻², and FF of 0.48 and has long lifetimes of 200 h under 1 sun degradation conditions.^[194] However, an excess of SnF₂ deteriorates the perovskite film morphology and device performance indicating that SnF₂ concentration must be kept very low; as a result, the background charge carrier density remains too large to achieve high efficiency, thus it becomes mandatory to explore new and more efficient ways to alleviate the background charge carrier density for better performance of the perovskite solar cell. It was also proposed that the fabrication of perovskite film must be carried out under a reducing vapor atmosphere to reduce the hole density in MASnI₃ films by inhibiting the oxidation of Sn²⁺ during the fabrication process. The excess use of SnF₂ induces the phase separation in perovskite films. As a result of exposure to excess SnF₂, plate like aggregates are formed in the film, thus it was resolved to use nonsolvent dripping process along with SnF₂ via the formation of SnF₂-pyrazine complex. Pyrazine has a strong binding affinity to SnF₂ thereby suppressing the phase separation induced by the excess use of SnF₂.^[195] **Table 4** shows some photovoltaic parameters of methylammonium tin halides.

Table 4. Photovoltaic parameters of methylammonium tin halides (MASnX₃).

Light absorber	E_g	V_{OC}	J_{SC}	FF	SPCE	Architecture	Ref.
MASnI ₃	1.23	0.88	16.8	0.42	6.4	FTO/c-TiO ₂ /mp-TiO ₂ /absorber/ Spiro-OMeTAD/Au	[120]
MASnI ₃	1.3	0.716	15.18	0.50	5.44	FTO/c-TiO ₂ /absorber/Spiro-OMeTAD/Au	[196]
MASnI ₃ +SnF ₂	1.3	0.32	21.4	0.46	3.15	FTO/c-TiO ₂ /mp-TiO ₂ /absorber/Au	[162]
MASnI ₃	1.3	0.38	12.1	0.36	1.7	ITO/PEDOT:PSS/poly-TPD/absorber/ C ₆₀ /BCP/Ag	[151]
MASnI ₃	1.26	0.27	17.4	0.39	1.86	FTO/c-TiO ₂ /mp-TiO ₂ /absorber/PTAA/Au	[197]
MASnIBr ₂	1.75	0.82	12.33	0.57	5.73	FTO/c-TiO ₂ /mp-TiO ₂ /absorber/ Spiro-OMeTAD/Au	[106]
MASnBr ₃	2.15	0.88	8.26	0.59	4.27	FTO/c-TiO ₂ /mp-TiO ₂ /absorber/ Spiro-OMeTAD/Au	[106]
MASnBr ₃	2.2	0.50	4.27	0.49	1.12	FTO/c-TiO ₂ /mp-TiO ₂ /absorber/P3HT/Au	[190]
MASnBr ₃	1.41	0.20	4.5	0.36	0.3	ITO/PEDOT:PSS/absorber/ PCBM/Bis-C ₆₀ /Ag	[198]
MASnI ₃ +hydrazine vapor	1.3	0.38	19.9	0.51	3.80	FTO/c-TiO ₂ /mp-TiO ₂ /absorber/PTAA/Au	[199]
MASnI ₃ +SnF ₂	–	0.45	11.8	0.40	2.14	FTO/PEDOT:PSS/absorber/C ₆₀ /BCP/Ag	[194]
en[MASnI ₃]+SnF ₂	1.4	0.43	24.3	0.63	6.63	FTO/c-TiO ₂ /mp-TiO ₂ /absorber/PTAA/Au	[142]
MASnI ₃ +SnF ₂		0.46	21.4	0.42	4.29	ITO/PEDOT:PSS/absorber/C ₆₀ /BCP/Ag	[150]
(FA) _{0.75} (MA) _{0.25} SnI ₃	1.33	0.61	21.2	0.62	8.12	ITO/PEDOT:PSS/absorber/C ₆₀ /BCP/Ag	[150]
(FA) _{0.75} (MA) _{0.5} SnI ₃	1.33	0.53	21.3	0.52	5.92	ITO/PEDOT:PSS/absorber/C ₆₀ /BCP/Ag	[150]
FASnI ₃	1.36	0.48	21.3	0.64	6.60	ITO/PEDOT:PSS/absorber/C ₆₀ /BCP/Ag	[150]
MASnIBr _{2-x} Cl _x +0%SnCl ₂ +100% SnBr ₂	1.81	0.31	13.37	0.52	2.18	Glass/FTO/TiO ₂ /absorber/carbon	[191]
10% SnCl ₂ +90% SnBr ₂	1.87	0.38	13.99	0.57	3.11	Glass/FTO/TiO ₂ /absorber/carbon	[191]
25% SnCl ₂ +75% SnBr ₂	1.97	0.35	11.06	0.47	1.87	Glass/FTO/TiO ₂ /absorber/carbon	[191]
50% SnCl ₂ +50% SnBr ₂	1.49	0.24	9.33	0.47	1.07	Glass/FTO/TiO ₂ /absorber/carbon	[191]
75% SnCl ₂ +25% SnBr ₂	1.36	0.19	13.34	0.32	0.81	Glass/FTO/TiO ₂ /absorber/carbon	[191]
100% SnCl ₂ +0% SnBr ₂	1.25	0.12	19.12	0.30	0.74	Glass/FTO/TiO ₂ /absorber/carbon	[191]

Formamidinium tin iodide FASnI₃ has a direct bandgap of 1.41 eV closer to the requisite bandgap value for use in perovskite solar cells and do possess a single stable phase over a broad temperature range up to 200 °C. Sn-based perovskite FASnI₃ is more stable than MASnI₃ due to suppression of oxidation of Sn²⁺ by FA⁺.^[188,200] FASnI₃ is first used as light absorber in perovskite solar cell by Koh et al.^[109] The fabricated films displayed a SPCE of 2.1%, J_{SC} of 24.5 mA cm⁻², V_{OC} of 0.2 V, and FF of 0.36. Additive SnF₂ is incorporated into FASnI₃ to suppress the oxidation of Sn²⁺ for better film morphology. A SPCE of 4.8% has been achieved by incorporating SnF₂ in FASnI₃ to form a complex with SnF₂ thereby improving the morphology of the perovskite film and slowing down the rate of crystallization of perovskite thin film. Antisolvent process can play a very significant role in preparing the uniform and pinhole-free compact thin film with the use of diethyl ether as an antisolvent. A significant SPCE of 6.22% has been achieved in FASnI₃ by using antisolvent process under forward scan with a small photocurrent hysteresis and a highly reproducibility.^[172]

SnF₂-pyrazine complex has been used to further enhance the morphology of FASnI₃ perovskite that achieved a SPCE of 4.8%, V_{OC} of 0.32 V, J_{SC} of 23.7 mA cm⁻², and improved

stability. The encapsulated FASnI₃ films displayed a stable performance for over 100 d maintaining 98% of their initial efficiency.^[195] Chlorobenzene is also used as an antisolvent for FASnI₃ films. The A-site cation in Sn-based perovskite has a significant effect on photovoltaic performance. The use of diethylammonium (en) and FA⁺ at A-site of tin-based perovskite results in a wider bandgap and an improved stability of photovoltaic performance. The complex en [FASnI₃] displayed a SPCE of 7.1% and retained 96% of its initial efficiency over 1000 h without encapsulation. Also, the addition of en at A-site cation along with (FA/MA/Cs) SnI₃ cannot reduce dimensionality of the perovskite to 2D.^[192]

The first mixed design composition in tin-based perovskite was reported on FA_{1-x}MA_xSnBr₃ with a cubic structure. The bandgap of the perovskite film was varied from 2.4 eV ($x = 0$) to 1.92 eV ($x = 0.82$) but the device displayed no photovoltaic performance.^[201]

Another mixed A-site cation perovskite (FA)_x(MA)_{1-x}SnI₃ has been investigated for its use as a light absorber in a perovskite solar cell with an inverted structure. By tuning the ratio of FA and MA yields the different values of SPCE. A SPCE of 8.12% is achieved for (FA)_{0.75}(MA)_{0.25}SnI₃ with V_{OC} of 0.61 V and bandgap of 1.33 eV. The high SPCE is attributed to the

improved perovskite film morphology and reduced recombination process.^[150]

Phenylethylammonium (PEA) is substituted at A-site in tin-based perovskite and pure 3D, 2D-3D mixture and pure 2D perovskite are fabricated by tuning the ratio of PEA from 0 to 100% such that inside every two metal halide octahedral layers, there is bilayer of PEA. The resulting mixed cation perovskite is $(\text{PEA})_2(\text{FA})_{n-1}\text{Sn}_n\text{I}_{3n+1}$ where n is the number of tin iodide layers in the structure unit ($n \geq 1$). For $n = 3, 4$, optical bandgaps of 1.5 and 1.42 eV are achieved. The 2D tin perovskite displayed better moisture stability than their 3D counterparts. Incorporation of 20% PEA into FA leads to low-dimensional mixed perovskite $(\text{PEA})_2\text{FA}_8\text{Sn}_9\text{I}_{28}$. The as-fabricated solar cells achieved a SPCE of 5.9% with V_{OC} of 0.55 V and J_{SC} of 14.4 mA cm^{-2} .^[156]

The incorporation of phenylethylammonium iodide (PEAI) obtained by evaporating it at the bilateral interface of a FASnI_3 film enhances the V_{OC} and FF of the mixed perovskite solar cell due to improvement in service coverage and formation of 2D-3D bulk heterojunction structure whereas the presence of LiF at A-site in tin-based perovskite by evaporating it at the bilateral interface of FASnI_3 film reduces the work function of PEDOT:PSS and aids in hole extracting at the ITO/PEDOT:PSS interfacial layer. A SPCE of 6.98% is achieved for LiF thickness of 5 nm in perovskite films with a V_{OC} of 0.47 V and FF of 0.74, respectively.^[202] The incorporation of BAI as an additive to the tin-based perovskite film as a light absorber changes the orientation of the crystal growth thereby enhancing the connectivity of the crystal grains. The fabricated FASnI_3 devices doped with 15% BAI exhibited a SPCE of 5.5% in contrast to the pristine FASnI_3 films having 4% efficiency.^[203] Similarly, the doping of EDAI_2 into FASnI_3 films results in the removal of pinholes in the perovskite films, inhibition of oxidation of Sn^{2+} into Sn^{4+} , and passivation of surface defect states. The 1% EDAI_2 -doped FASnI_3 perovskite films displayed an efficiency of 8.9% with a stability of over 1400 h with only slight degradation for more than 200 h in contrast to pristine FASnI_3 films with a SPCE of 7.4% only. The high efficiency is attributed to improved perovskite film morphology and passivation of surface defects that enable better separation of charge carriers and suppression of oxidation of Sn^{2+} to Sn^{4+} .^[203] **Figure 11a** shows the schematic representations of perovskite crystals in the presence of BAI and EDAI_2 additives; top-view SEM images of (b) pristine FASnI_3 , (c) FASnI_3 -BAI 15%, and (d) FASnI_3 - EDAI_2 1%; (e) current-voltage curves, (f) corresponding IPCE spectra with integrated current densities, (g) histograms of 30 fresh cells fabricated under the same experimental conditions, (h) Mott-Schottky plots, (i) Nyquist plots obtained from electrochemical impedance spectra (EIS), and (j) stabilized power-conversion efficiencies and photocurrent densities of the FASnI_3 -BAI 15% and FASnI_3 - EDAI_2 1% devices for 240 s.^[203]

Crystalline FASnI_3 with the orthorhombic a -axis out-of-plane direction was fabricated by mixing (0.08 M) 2D tin perovskite with (0.92 M) 3D tin perovskite in a planar p-i-n structure and achieved a SPCE of 9% with a V_{OC} of 0.25 V with more efficient collection of charge and stability in ambient air.^[145] The introduction of a low-dimensional interlayer to the interface in a FASnI_3 perovskite solar cell can improve the morphology of the film reducing the number of trap sites. As a result, the charge

accumulation and recombination in the device is suppressed leading to a high SPCE of 7.05%.^[204]

The bifunctional ammonium cations, 2-hydroxyethyl ammonium $\text{OH}(\text{CH}_2)\text{NH}_3^+$ (HEA⁺), are incorporated into FASnI_3 resulting in a mixed tin-based perovskite $\text{HEA}_x\text{FA}_{1-x}\text{SnI}_3$ where $x = 0-1$ and can act as a light absorber in carbon-based mesoscopic solar cells. As a consequence of incorporation of HEA⁺, the crystal lattice changed from orthorhombic to rhombohedra ($x = 0.2-0.4$). For $x \geq 0.6$, a 3D vacant perovskite $(\text{HEA})_x\text{FA}_{1-x}\text{Sn}_{0.67}\text{I}_{2.33}$ with a tetragonal structure is formed. The light absorbers in this series are synthesized by employing mesoporous solar cells using one-step drop-cast (DC), two-step solvent-solvent extraction (SE), and a solvent extraction by using ethylenediammonium diiodide (EDAI_2) as an additive. The fabricated solar device $\text{HEA}_{0.4}\text{FA}_{0.6}\text{SnI}_3$ displayed the photovoltaic parameters with V_{OC} of 0.371 V, J_{SC} of 18.52 mA cm^{-2} , FF of 0.562, and a stable SPCE of 3.9% for a period of 340 h.^[205] The FASnI_3 perovskite light absorbers incorporated with a diammonium cation such as propylenediammonium (PW) and trimethylenediammonium (TN) display better efficiency than the pristine FASnI_3 solar cell. The FASnI_3 light absorbers mixed with 10% TN and 10% PN displayed a SPCE of 5.53 and 5.58% with a better film morphology along with retaining their 3D perovskite structure.^[206] **Figure 11** shows the (k) device structure, (l) $J-V$ curves, (m) EQE curves, and (n) PCE statistics of the FASnI_3 solar cells with and without 10% PN and 10% TN.^[206] The addition of bromide into FASnI_3 crystal lattice reduces the p-doping in the perovskite film by reducing the Sn vacancies thereby lowering the current density of the light absorbers. As a result, there is an enhancement in charge recombination lifetime that increases V_{OC} and FF of the devices having M-TiO_2 as electron transport layer. The fabricated devices achieved SPCE of 5.5% with high stability of encapsulated devices over 1000 h under continuous illumination including UV region.^[167] **Table 5** shows some photovoltaic parameters of formamidinium tin halides.

Cesium tin iodide perovskite CsSnI_3 possess a direct bandgap of 1.30 eV, a melting point of 435 °C indicating its better thermal stability and a 3D orthorhombic structure^[110,210,211] whereas cesium tin bromide perovskite CsSnBr_3 has a bandgap of 1.7 eV.^[102] Cesium-based tin perovskite has a high hole mobility of $585 \text{ cm}^{-1} \text{ V}^{-1} \text{ s}^{-1}$, low exciton binding energy (180 meV) than MAPbI_3 .^[119,187] The melt-synthesized CsSnI_3 ingots containing high-quality large single crystal grains have been reported to have bulk carrier lifetime more than 6.6 ns, doping concentration of about $4.5 \times 10^{17} \text{ cm}^{-3}$, and minority carrier diffusion lengths approaching to 1 μm .^[118] A SPCE of 23% was predicted for optimized single crystal solar cells CsSnI_3 highlighting their great potential for use in perovskite solar cell. The CsSnI_3 was first used in a Schottky-type perovskite solar cell consisting of simple layer architecture of ITO/ CsSnI_3 /Au/Ti on a glass substrate that achieved an efficiency of 0.9%. A HTM-free CsSnI_3 perovskite solar cell with SnI_2 as an additive displayed an efficiency of up to 2.76% with a V_{OC} of 0.43 V and FF of 0.39.^[212] The use of excess SnI_2 as an additive in CsSnI_3 not only suppress Sn^{2+} vacancies but also reduces p-type conductivity thereby producing a SPCE of 4.8% in CsSnI_3 perovskite solar cells.^[213] The thin films of CsSnI_3 were fabricated with the addition of hypophosphorous acid (HPA) with thermal stability

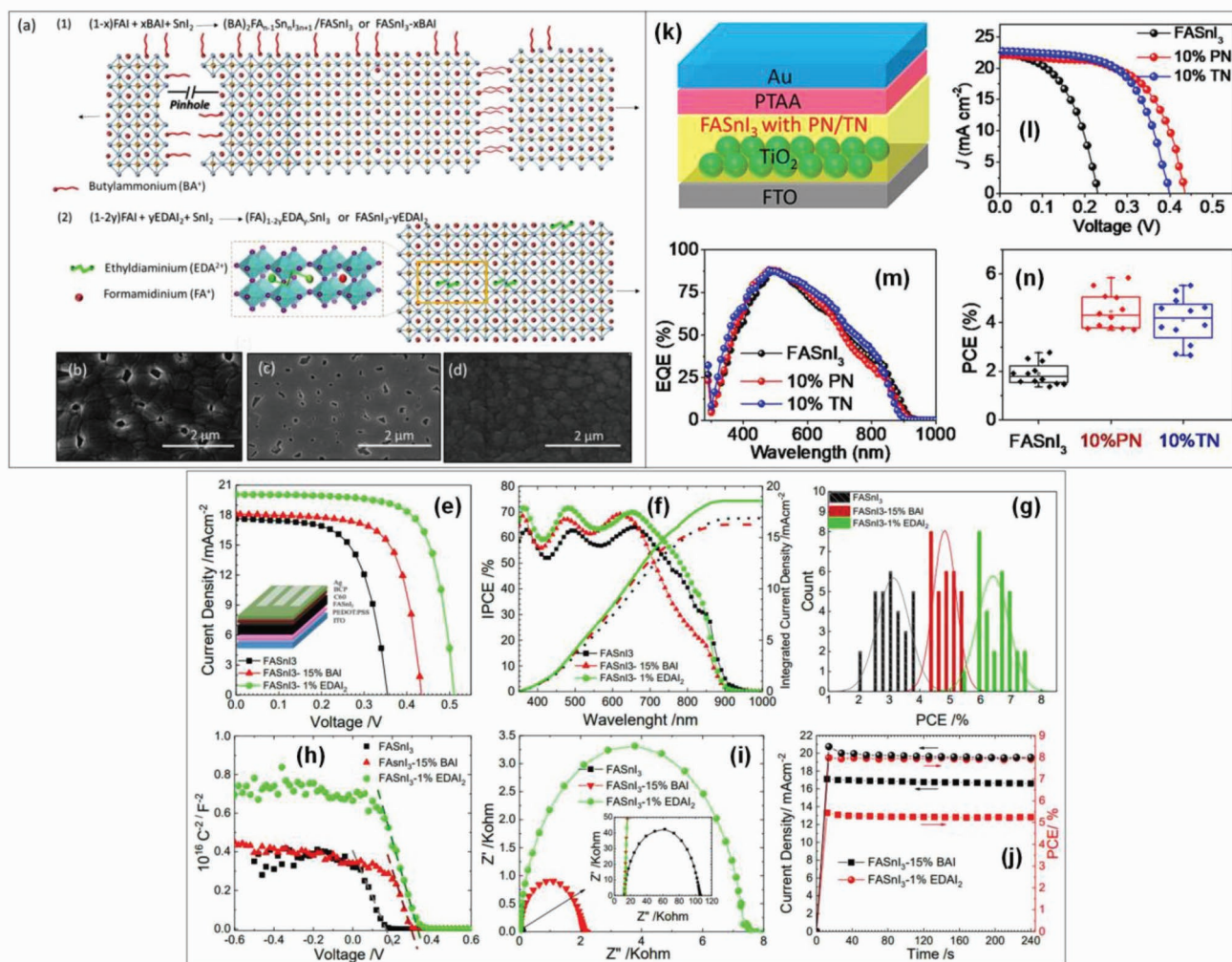


Figure 11. a) Schematic representations of perovskite crystals in the presence of BAI and EDAl₂ additives; top-view SEM images of b) pristine FASnI₃, c) FASnI₃-BAI 15%, and d) FASnI₃-EDAl₂ 1%; e) current–voltage curves, f) corresponding IPCE spectra with integrated current densities, g) histograms of 30 fresh cells fabricated under the same experimental conditions, h) Mott–Schottky plots, i) Nyquist plots obtained from electrochemical impedance spectra (EIS), and j) stabilized power-conversion efficiencies and photocurrent densities of the FASnI₃-BAI 15% and FASnI₃-EDAl₂ 1% devices for 240 s; Reproduced with permission.^[203] Copyright 2018, Royal Society of Chemistry. k) Device structure, l) J–V curves, m) EQE curves, and n) PCE statistics of the FASnI₃ solar cells with and without 10% PN and 10% TN; Reproduced with permission.^[206] Copyright 2018, American Chemical Society.

up to 473 K achieving a SPCE of 3% that last for over 77 d.^[193] The results of a computational study on mixed cesium perovskite Rb_yCs_{1-y}Sn (Br_xI_{3-x})₃ as a light absorber have revealed that the substitution of Rb⁺ for Cs⁺ enhanced the quality of perovskite film and its practical applicability in perovskite solar cells.^[214] Another study on CsSnI₃ and CsSnI_{3-x}Br_x as light absorbers in n-i-p devices structure reported an efficiency of 2%. CsSnI₃ has a small bandgap of 1.27 eV to a near-infrared absorption onset to 950 nm and exhibited a high charge carrier density up to 27.67 mA cm⁻².^[215]

An excess of SnCl₂ and SnI₂ to CsSnI₃ perovskite films can have masked influence on both stability and SPCE of the corresponding cells reported to be of 3%. An extensive monitoring of oxidation of CsSnI₃ in the air by using additives SnCl₂, SnBr₂, and SnI₂ has been carried out to measure electronic, optical absorption spectrum with time and reported that it exhibits the highest stability by inhibiting the crystallization/

decomposition.^[163,192] The addition of SnF₂ lowers the background charge carrier density by neutralizing traps.^[214,216] The mesostructured CsSnI₃ displayed a SPCE of 2.02% with the addition of 20% SnF₂ as an additive. Also a spectral response of 950 nm is demonstrated with SnF₂ addition. As a result, the concentration of the defect is reduced that further suppressed the background charge carrier density.^[215] The anionic substitution of Br⁻ in CsSnI_{3-x}Br_x (0 ≤ x ≤ 3) results in change in crystal structure from orthorhombic to cubic framework for CsSnBr₃ enhancing the V_{OC} and J_{SC} as a result of decrease in tin vacancies and low charge carrier densities of 10¹⁵ cm⁻³.^[217] The carrier lifetime gets enhanced and the PL line width has reduced when the temperature decreases below 110 K due to the phase transition from orthorhombic to tetragonal phase in CsSnX₃ that improved the solar cell performance.^[218]

The evaporation method comprising of thermal evaporation with solution method has been used to produce smooth

Table 5. Photovoltaic parameters of formamidinium tin halides (FASnX₃).

Light absorber	E _g	V _{OC}	J _{SC}	FF	SPCE	Architecture	Ref.
FASnI ₃ +SnF ₂	1.41	0.24	24.5	0.36	2.1	FTO/c-TiO ₂ /mp-TiO ₂ /absorber/Spiro-OMeTAD/Au	[195]
FASnI ₃ +SnF ₂ piperazine	1.4	0.32	23.7	0.63	4.8	FTO/c-TiO ₂ /mp-TiO ₂ /absorber/Spiro-OMeTAD/Au	[109]
FASnI ₃ +diethyl ether	1.36	0.47	22.1	0.60	6.22	ITO/PEDOT:PSS/absorber/C ₆₀ /BCP/Ag	[172]
FASnI ₃ +SnF ₂	1.4	0.48	21.3	0.64	6.6	ITO/PEDOT:PSS/absorber/C ₆₀ /BCP/Ag	[150]
FASnI ₃ +SnF ₂	1.4	0.38	23.1	0.60	5.27	FTO/c-TiO ₂ /mp-TiO ₂ /ZnS/absorber/PTAA/Au	[207]
en[FASnI ₃]	1.5	0.48	22.5	0.66	7.14	FTO/c-TiO ₂ /mp-TiO ₂ /absorber/PTAA/Au	[208]
FA _{0.25} MA _{0.75} SnI ₃ +SnF ₂	1.28	0.48	20.7	0.45	4.49	ITO/PEDOT:PSS/absorber/C ₆₀ /BCP/Ag	[150]
FA _{0.50} MA _{0.50} SnI ₃ +SnF ₂	1.33	0.53	21.3	0.52	5.92	ITO/PEDOT:PSS/absorber/C ₆₀ /BCP/Ag	[150]
FA _{0.75} MA _{0.25} SnI ₃ +SnF ₂	1.33	0.61	21.2	0.62	8.12	ITO/PEDOT:PSS/absorber/C ₆₀ /BCP/Ag	[150]
FA _{0.8} CS _{0.2} SnI ₃	1.41	0.24	16.05	0.35	1.4	ITO/PEDOT:PSS/absorber/PCBM/Bis-C ₆₀ /Ag	[198]
FASnI ₃	1.37	0.31	18.36	0.67	3.85	ITO/PEDOT:PSS/absorber/C ₆₀ /BCP/Ag	[202]
FASnI ₃ +50% PEAL	1.38	0.38	19.96	0.69	5.28	ITO/PEDOT:PSS/absorber/C ₆₀ /BCP/Ag	[202]
(PEA) ₂ (FA) ₂ Sn ₂ I ₂₈ +SnF ₂	1.789	0.59	14.4	0.69	5.94	ITO/NiOx/absorber/PCBM/Al	[156]
(BA) ₂ (MA) ₃ Sn ₄ I ₁₃ +SnF ₂	1.42	0.229	24.1	0.45	2.53	FTO/c-TiO ₂ /mp-TiO ₂ /absorber/PTAA/Au	[209]
FASnI ₃ +LiF (0 nm)	–	0.38	19.65	0.71	5.04	ITO/PEDOT:PSS/absorber/C ₆₀ /BCP/Ag	[202]
FASnI ₃ +LiF (3 nm)	–	0.42	19.83	0.73	5.96	ITO/PEDOT:PSS/absorber/C ₆₀ /BCP/Ag	[202]
FASnI ₃ +LiF (5 nm)	–	0.47	20.00	0.73	6.77	ITO/PEDOT:PSS/absorber/C ₆₀ /BCP/Ag	[202]
FASnI ₃ +LiF (8 nm)	–	0.45	16.66	0.65	4.71	ITO/PEDOT:PSS/absorber/C ₆₀ /BCP/Ag	[202]
FASnI ₃	–	0.36	17.6	0.62	4.0	ITO/PEDOT:PSS/absorber/C ₆₀ /BCP/Ag	[203]
FASnI ₃ +15% (BAI)	1.40	0.44	18.0	0.69	5.5	ITO/PEDOT:PSS/absorber/C ₆₀ /BCP/Ag	[203]
FASnI ₃ +1% EDAL ₂	1.43	0.51	20.0	0.71	7.4	ITO/PEDOT:PSS/absorber/C ₆₀ /BCP/Ag	[203]
FASnI ₃ +2% EDAL ₂	1.44	0.58	21.3	0.71	9.6	ITO/PEDOT:PSS/absorber/C ₆₀ /BCP/Ag	[203]
FASnI ₃	–	0.525	24.1	0.71	9.0	ITO/PEDOT:PSS/absorber/C ₆₀ /BCP/Al	[145]
HEA _{0.4} FA _{0.6} SnI ₃ +3%EDAL ₂	–	0.371	18.52	0.562	3.9	–	[205]
FASnI ₃ +10%TN	–	0.398	22.72	0.610	5.53	FTO/mp-TiO ₂ /absorber/PTAA/Au	[206]
FASnI ₃ +10%PN	–	0.435	22.15	0.606	5.85	FTO/mp-TiO ₂ /absorber/PTAA/Au	[206]

uniform dense pinhole-free CsSnI₃ films that achieved a SPCE of 1.86% with V_{OC} of 0.265 V, J_{SC} of 15.25 mA cm⁻², and FF of 0.46, by using the architecture (FTO/bl-TiO₂/mp-TiO₂/absorber/Spiro-OMeTAD).^[102]The undesirable p-doping of CsSnI₃ perovskite films can be reduced by the addition of piperazine that can improve the morphology of the film as well as can alleviate the crystallization of excess SnI₂ at the same time. With the use of piperazine as an additive, CsSnI₃ perovskite devices displayed a SPCE of 3.83%.^[219] **Table 6** shows some photovoltaic parameters of cesium-based perovskites. **Figure 12** shows schematic diagram along with the performance of CsSnI₃-based perovskite solar cell.^[170]

Tin in +4 oxidation state shows more air and moisture stability with enhanced photovoltaic properties. To combat the challenge of oxidation of Sn²⁺ to Sn⁴⁺, tin-based perovskite structures like A₂SnX₆ are investigated for their use in a perovskite solar cell.^[105,221,222] Tin-based Cs₂SnI₆ as a light absorber has reported a SPCE of almost 1%. These perovskites have been investigated for their use as hole transport material in solar cells.^[223] Cs₂SnI₃Br₃^[222] and Cs₂SnI₆^[224] as light absorbers in solid-state dye-sensitized solar cells have displayed an efficiency of 7.8%^[224] by using classical dyes as a light absorber. Cs₂SnI₆ used as a hole transport material in solid-state DSSCs reported

an efficiency close to 8.6% in air.^[224] Cs₂SnI₆ has a direct bandgap of 1.3–1.6 eV, high absorption coefficient, high electron carrier concentration of the order of 1 × 10¹⁴ cm⁻³, electron mobility of 310 cm² V⁻¹ s⁻¹, and better stability in air with moisture than that of CsSnI₃ as Sn⁴⁺ is chemically more stable than Sn²⁺.^[105,216,225] The cesium-based perovskite Cs₂SnI₆ as a light absorber was first studied in 2016 that reported an efficiency of 1%.^[216,223] Cs₂SnI₆ do possess defects of iodide vacancies and interstitial Sn atoms that give rise to the intrinsic n-type behavior completely opposite to p-type behavior in CsSnI₃. Optimization of thickness of perovskite light absorption layers leads to spontaneous oxidation conversion of unstable B-YCsSnI₃ to air stable Cs₂SnI₆ that has bandgap of 1.48 eV and a high absorption coefficient of 10⁵ cm⁻¹.^[216] The bandgap of A₂SnX₆ perovskite depends upon the composition of halide anion. With increase in bromide composition CsSnI_{6-x}Br_x, the bandgap can be tuned from 1.3 to 2.9 eV and the color of the film changes from dark brown to brown red then to yellow. Cs₂SnI₄Br₂ reported an efficiency of 2.03% highest among all the fabricated compositions. The fabrication of all the reported composition was done in ambient air without the use of any additive and the perovskite film exhibited thermal stability.^[226] The polycrystalline films of (MA)₂SnI₆ have been proposed by

Table 6. Photovoltaic parameters of cesium-based perovskites.

Light absorber	E_g	V_{oc}	J_{sc}	FF	SPCE	Architecture	Ref.
CsSnI ₃ +SnI ₂	1.3	0.38	25.71	0.49	4.81	FTO/c-TiO ₂ /mp-TiO ₂ /absorber/PTAA/Au	[213]
CsSnI ₃ +SnI ₂	1.3	0.43	12.3	0.39	2.76	ITO/CuI/absorber/ICBA/BCP/Al	[159]
CsSnI ₃	1.3	0.52	10.2	0.62	3.31	ITO/NiO _x /absorber/PCBM/Al	[157]
CsSnI ₃ +SnCl ₂	1.3	0.50	9.89	0.68	3.56	ITO/absorber/PC ₆₁ BM/BCP/Al	[163]
CsSnI ₃ +SnF ₂	1.27	0.20	22.7	0.29	1.66	FTO/TiO ₂ /mp-TiO ₂ /absorber/Spiro-OMeTAD/Au	[217]
CsSnI ₃ +SnF ₂	1.25	0.17	30.8	0.34	1.83	FTO/c-TiO ₂ /mp-TiO ₂ /absorber/PTAA/Au	[199]
CsSnI ₃ +SnF ₂	1.3	0.24	27.7	0.37	2.0	FTO/c-TiO ₂ /mp-TiO ₂ /absorber/m-MTDATA/Au	[215]
CsSnI ₃	1.3	0.42	4.8	0.22	0.88	ITO/absorber/Au/Ti	[212]
CsSnBr ₃ +SnF ₂	1.8	0.45	2.4	0.55	0.55	ITO/MoO ₃ /absorber/C ₆₀ /BCP/Ag	[220]
CsSnBr ₃ +SnF ₂	1.75	0.41	3.99	0.58	0.95	ITO/mp-TiO ₂ /absorber/Spiro-OMeTAD/Au	[217]
CsSnIBr ₂ +SnF ₂	1.65	0.31	11.6	0.43	1.56	ITO/mp-TiO ₂ /absorber/Spiro-OMeTAD/Au	[217]
CsSnIBr ₂ +HPA-SnF ₂	1.63	0.31	17.4	0.57	3.2	FTO/c-TiO ₂ /Al ₂ O ₃ /absorber/C	[193]
CsSnBr ₃ +SnF ₂	1.79	0.37	14.0	0.59	3.04	FTO/c-TiO ₂ /mp-TiO ₂ /absorber/PTAA/Au	[199]
CsSnBr ₃ +SnF ₂	1.75	0.42	9.1	0.58	2.1	FTO/c-TiO ₂ /mp-TiO ₂ /absorber/Spiro-OMETAD/Au	[102]
CsSnI _{2.9} Br _{0.1} +SnF ₂	–	0.22	24.16	0.33	1.76	FTO/c-TiO ₂ /mp-TiO ₂ /absorber/Spiro-OMETAD/Au	[217]
CsSnI ₃	–	0.265	15.25	0.46	1.86	FTO/bl-TiO ₂ /mp-TiO ₂ /absorber/Spiro-OMETAD/Au	[170]

using thermal evaporation method having a direct bandgap of 1.81 eV with a strong absorption coefficient of $7 \times 10^4 \text{ cm}^{-1}$, carrier concentration of $2 \times 10^{15} \text{ cm}^{-3}$, and electron mobility of $\approx 3 \text{ cm}^2 \text{ V}^{-1} \text{ s}^{-1}$.^[129] Table 7 shows some photovoltaic parameters of cesium-based perovskites.

7.2. Germanium-Based Perovskites

Germanium is another candidate for substitution of lead for lead-free perovskite solar cells because of its valence electronic configuration as that of Pb²⁺. Ge²⁺ has a small ionic radius (73 pm) as compared to that of divalent metal cation Pb²⁺ (119 pm) and Sn (110 pm). Ge²⁺ is low in toxicity than Pb²⁺.^[227]

However, germanium is prone to oxidation than tin. It has a value of electronegativity (2.1) as compared to Pb (3.2) and Sn (1.96). Methyl ammonium germanium halides MAgGeX₃ are the most potential candidate for perovskites solar cells as Goldschmidt tolerance factor for MAgGeX₃[X=Cl, Br, I] has value of 1.005, 0.988, and 0.965, respectively, that is close to the optimum range $0.99 < t < 1.03$ for a material to form a stable 3D perovskite structure. MAgGeI₃ has an optical bandgap 1.63 eV which is greater in magnitude than that of MAPbI₃ (1.55 eV) and MASnI₃ (1.30), excellent hole and electron conducting behavior and better stability in air as compared to MaPbI₃.^[217] However, Ge²⁺ cation being smaller in size (73 pm) deviates from its regular [GeI₆] octahedral center as it replaces cation of much larger ionic radius as that of Pb²⁺ (119 pm) and Sn²⁺ (110 pm).^[228] As a

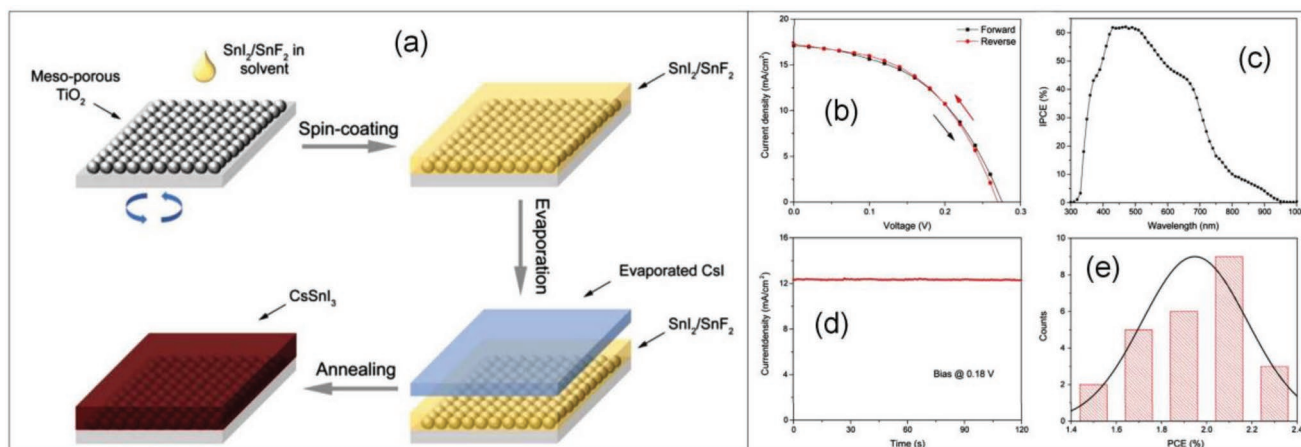


Figure 12. a) Schematic diagram for development of evaporation-assisted solution (EAS) method using CsSnI₃. b) J–V curves of the device by EAS method in both forward and reverse directions, c) IPCE spectrum of the optimized device ($V_{oc} = 0.265 \text{ V}$, $J_{sc} = 15.25 \text{ mA cm}^{-2}$, FF = 46.05%, and PCE = 1.86%), d) steady-state current density of champion device at a bias of 0.18 V, and e) PCE histogram of 25 tested devices. Reproduced with permission.^[170] Copyright 2018, Wiley-VCH.

Table 7. Photovoltaic parameters of tin-based perovskites A_2SnX_6 .

Light absorber	E_g	J_{sc}	V_{oc}	FF	SPCE	Architecture	Ref.
Cs_2SnI_6	1.48	5.41	0.51	0.35	0.96	FTO/TiO ₂ /absorber/P3HT/Ag	[216]
Cs_2SnI_6	1.30	6.75	0.37	0.59	1.47	FTO/bl-TiO ₂ /2% Sn-TiO ₂ /absorber/Cs ₂ SnI ₆ HTM/LPAH/FTO	[226]
Cs_2SnI_3Br	1.38	6.58	0.44	0.55	1.60	FTO/bl-TiO ₂ /2% Sn-TiO ₂ /absorber/Cs ₂ SnI ₆ HTM/LPAH/FTO	[226]
$Cs_2SnI_4Br_2$	1.40	6.23	0.56	0.57	2.03	FTO/bl-TiO ₂ /2% Sn-TiO ₂ /absorber/Cs ₂ SnI ₆ HTM/LPAH/FTO	[226]
$Cs_2SnI_2Br_4$	1.63	3.41	0.58	0.54	1.08	FTO/bl-TiO ₂ /2% Sn-TiO ₂ /absorber/Cs ₂ SnI ₆ HTM/LPAH/FTO	[226]
Cs_2SnIBr_5	2.36	0.01	0.57	0.37	0.002	FTO/bl-TiO ₂ /2% Sn-TiO ₂ /absorber/Cs ₂ SnI ₆ HTM/LPAH/FTO	[226]
Cs_2SnBr_6	2.85	–	–	–	–	FTO/bl-TiO ₂ /2% Sn-TiO ₂ /absorber/Cs ₂ SnI ₆ HTM/LPAH/FTO	[226]

consequence, it forms three short Ge–I bonds (2.73–2.77 Å)^[228] and three long in Ge–I bonds (3.26–3.58 Å). The Ge-based perovskites have been extensively studied by carrying computational work based on density functional theory (DFT).^[229,230] The size of constituent halide ion has a remarkable effect on the bandgap of Ge-based perovskite. The DFT calculations of bandgap values of CsGeX₃[X=Cl, Br, I] showed the decreasing trend of 3.67, 2.32, and 1.53 eV, respectively.^[231] Similar trend is noticed in MAGEI₃[X=Cl, Br, I] whose DFT calculations reveal that with the increase in size of halide anion, the bandgaps have decreasing values of 3.7, 2.81, and 1.61 eV.^[230] The cation at A-site also plays a pivotal role for the size of bandgap of AGEI₃.^[144,230] Bandgaps show an increasing trend when small Cs⁺ cation (1.6 eV) is replaced by a larger counterpart such as CH₃NH₃⁺ (1.9 eV) and CH(NH₂)⁺ (2.2 eV), acetamidinium (2.5 eV), trimethylammonium (2.8 eV), guanidinium (2.7 eV), and isopropyl ammonium (2.7 eV).^[229]

A study of Ge-based perovskite AGEX₃ (A=Cs⁺, CH₃NH₃⁺, HC(NH₂)₂⁺) reported the estimated values of optical bandgap derived from tauc plot for CsGeI₃ (1.63 eV), MAGEI₃ (2.0 eV), and FAGEI₃ (2.3 eV).^[144] The replacement of Cs with MA and FA decreases the valence band level as evident from measured value of valence band of CsGeI₃, MAGEI₃, and FAGEI₃ that has the value of –5.10, –5.2, and –5.5 eV, respectively, by photoemission spectroscopy in air.^[144] CsGeI₃ displays a higher stability up to 850 °C in contrast to up to ≈250 °C stability shown by MAGEI₃ and FAGEI₃. Ge-based perovskite solar cells have two values of V_{oc} due to its oxidation into Ge⁴⁺ during the fabrication process. The poor quality of FAGEI₃ films results in loss of photoconductivity in them.^[144] The small A-site cations like Cs⁺, CH₃NH₃⁺, and HC(NH₂)₂⁺ in AGEX₃ lead to 3D structure framework based on corner-sharing octahedral and the perovskite materials do exhibit direct bandgaps whereas large A-size cations lead to distortion of the crystal structure. As a result, 1D chain like perovskite structures are formed having indirect bandgaps.^[144,229] The introduction of bromide ions into MAGEI₃ perovskites enhances not only photovoltaic performance but also stability to a slight extent.^[232] The substitution of 10% of the iodide content by bromide results in MAGEI_{2.7}Br_{0.3} perovskite that reported a SPCE of 0.57% as a light absorber in solar cells fabricated with planar p-i-n architecture having PEDOTS:PSS as HTM and PC₇₀BM as ETM.^[232]

The mixed Ge-based perovskite RbSn_{0.5}Ge_{0.5}I₃ displays a direct optical bandgap in the range of 0.9–1.6 eV with sufficient optical absorption spectrum comparable to MAPX₃ perovskites. The material exhibited favorable effective masses for higher

carrier mobility and good stability in water.^[233] A 2D perovskite (C₆H₅(CH₂)₂NH₃)₂GeI₄ [(PEA)₂GeI₄] consisting of inorganic germanium iodide planes separated by organic PEA layers has a direct bandgap of 2.12 eV that is very close to the value 2.17 eV obtained through DFT calculations. The perovskite material exhibits luminescence at room temperature with a medium lifetime and is a potential candidate for PV applications. The 2D (PEA)₂GeI₄ shows more stability in air than 3D MAGEI₃ that is attributed to the presence of a hydrophobic organic long chain.^[234] On the basis of DFT calculations, one more 2D Ruddlesden–Popper hybrid organic–inorganic perovskite BA₂MA_{n–1}MnI_{3n+1} [M = Sn or Ge, n = 2–4] has been reported that has suitable excitonic and optical light absorbing properties for application in lead-free perovskites. Moreover, 2D Ge-based perovskites have enhanced thermodynamic stability in comparison to their 3D counterparts that enables 2D Ge-based perovskites with a thickness of a few tens of unit cells to be used as light absorbers in perovskite solar cell.^[235] **Table 8** shows some photovoltaic parameters of Ge-based perovskites. **Figure 13** shows the crystal structure, band diagram, and the I–V characteristics of Ge-based perovskites in a solar cell (a) CsGeI₃ and (b) MAGEI₃,^[229] (c) optical absorption spectrum of CsGeI₃, MAGEI₃, and FAGEI₃, in comparison with CsSnI₃, and (d) calculated band structure and projected density of states of CsGeI₃. The energy of the highest occupied state is set to 0 eV. (e) Photoelectron spectroscopy in air (PESA) of powder samples and (f) schematic energy level diagram of CsGeI₃, MAGEI₃, and FAGEI.^[144]

7.3. Bismuth-Based Perovskites

Bismuth can form +3 ions with similar valence electronic configuration as that of Pb²⁺, having ionic radius (103 pm) in comparison to divalent Pb²⁺ (119 pm) and Sn²⁺ (110 pm). The value of electronegativity of bismuth is 2.02 in comparison to that of Pb (2.33) and Sn (1.96).^[237] Bismuth-based perovskites are represented with a general formula A₃Bi₂X₉, where A can be MA, Cs, NH₃, Ag. These materials have attracted large attention due to their low toxic nature.^[238] They can have 0D dimer, 1D chain like, 2D layered, or 3D double perovskite elpasolite frameworks,^[238] containing A-site cations such as MA⁺, Cs⁺, Rb⁺, K⁺, guanidinium, cyclohexylammonium, imidazolium to form a 0D dimer perovskite structure.^[143] Bismuth-based methylammonium single crystal MABi₂I₉ (MBI) shows a regular hexagon shape with a diameter ranging from 100 to 200 nm.

Table 8. Ge-based perovskites and their photovoltaic parameters.

Light absorber	E_g	V_{OC}	J_{SC}	FF	SPCE	Architecture	Ref.
MAGeI ₃	2.0	0.15	4.0	0.30	0.2	FTO/c-TiO ₂ /mp-TiO ₂ /absorber/Spiro-OMeTAD/Au	[144]
CsGeI ₃	1.63	0.07	5.7	0.27	0.11	FTO/c-TiO ₂ /mp-TiO ₂ /absorber/Spiro-OMeTAD/Au	[144]
CsGeI ₃	–	0.57	10.49	0.53	3.2	FTO/mp-TiO ₂ /CsGeI ₃ /P3HT Au	[236]

The MBI crystals exhibit a dark red color with an optical bandgap of ≈ 2.11 eV. The 0D MBI consists of face-sharing bi-octahedral [Bi₂I₉] clusters surrounded by MA⁺ cations. The fabricated solar cells using MBI as light absorbing layer reported

an efficiency of 0.08% with J_{SC} (≈ 0.36 mA cm⁻²), V_{OC} of 0.51 V, and FF of 0.44. The photovoltaic performance was enhanced by using thick mesoporous TiO₂ layer (1.8 μ m) to V_{OC} of 0.51 V, J_{SC} of 1.16 mA cm⁻², FF of 0.46, and SPCE of 0.19%.^[127]

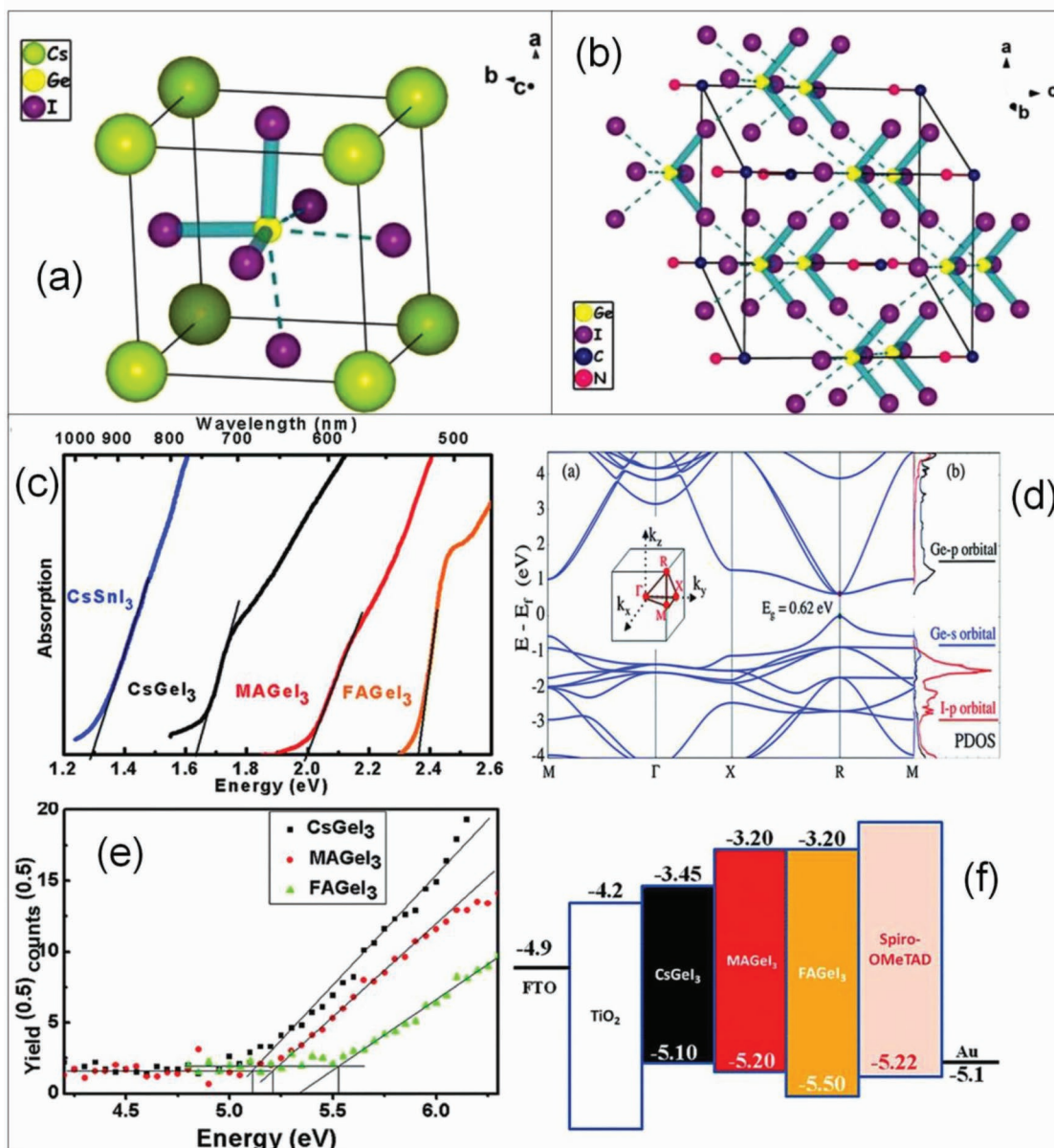


Figure 13. Schematic diagram for the unit cell of a) CsGeI₃ and b) MAGeI₃; Reproduced with permission.^[229] Copyright 2015, American Chemical Society. c) Optical absorption spectrum of CsGeI₃, MAGeI₃, and FAGEI₃, in comparison with CsSnI₃. d) Calculated band structure and projected density of states of CsGeI₃. The energy of the highest occupied state is set to 0 eV. e) Photoelectron spectroscopy in air (PESA) of powder samples and f) schematic energy level diagram of CsGeI₃, MAGeI₃, and FAGEI₃; Reproduced with permission.^[144] Copyright 2012, Royal Society of Chemistry.

The positive Hall coefficient of MBI film reveals p-type charge carrier with carrier concentration of 10^{15} – 10^{16} cm^{-3} for solution-processed MBI films. MBI films have got excellent stability against exposure to humidity level of 50% and ambient air at room temperature for 40 d.^[127] The first study on bismuth-based perovskite $(\text{MA})_3\text{Bi}_2\text{I}_9$ as a light absorber was reported by preparing simple $(\text{MA})_3\text{Bi}_2\text{I}_9$ perovskite and mixed $(\text{MA})_3\text{Bi}_2\text{I}_{9-x}\text{Cl}_x$ perovskite thin films with a hexagonal crystalline phase. The mesostructured solar cells displayed a better SPCE of 0.12%, V_{OC} of 0.68 V, J_{SC} of 0.52 mA cm^{-2} , and FF of 0.33 as compared to $(\text{MA})_3\text{Bi}_2\text{I}_{9-x}\text{Cl}_x$ displaying SPCE of 0.003, V_{OC} of 0.04 V, J_{SC} of 0.18 mA cm^{-2} , and FF of 0.38. Also the substitution of iodine with chloride in $(\text{MA})_3\text{Bi}_2\text{I}_{9-x}\text{Cl}_x$ shifted the bandgap from 2.1 to 2.4 eV.^[111] An efficiency of 0.42% is achieved by using a mesoporous TiO_2 substrate for fabricating a $(\text{MA})_3\text{Bi}_2\text{I}_9$ perovskite film with V_{OC} of 0.67 V, J_{SC} of 1.0 mA cm^{-2} , and FF of 0.62.^[240] $\text{MA}_3\text{Bi}_2\text{I}_9$ films fabricated by evaporation-spin-coating process produced better quality films which produced SPCE of 0.39% in an inverted planar device with a V_{OC} of 0.83 V, J_{SC} of 1.39 mA cm^{-2} , and FF of 0.34.^[241] The gas-assisted deposition method enhances the morphology of active light absorber layer. The fabricated $(\text{MA})_3\text{Bi}_2\text{I}_9$ light absorber layer by gas-assisted deposition process reported an enhanced value of SPCE of 0.08% and V_{OC} of 0.686 V.^[242] The solvent annealing in $(\text{MA})_3\text{Bi}_2\text{I}_9$ films enhances its electrical conductivity. The DMF-induced solvent annealing impacts the charge transport through the films.^[243] The morphology of $(\text{MA})_3\text{Bi}_2\text{I}_9$ perovskite film can also be enhanced by incorporating a small amount of N-methyl-2 pyrrolidone (NMP) into the MBI-DMF solution. The addition of various concentration of NMP into the precursor solution not only controls the rate of crystallization but also enhanced SPCE to a value of 0.31% and stability for 30 d in a relative humidity of 50–60%.^[244] The optical measurement of solution-processed perovskite film $(\text{MA})_3\text{Bi}_2\text{I}_9$ fabricated by spin-coating process showed a strong absorption band around 500 nm on further heating. The devices made on anatase TiO_2 mesoporous layer exhibited a current density of 0.8 mA cm^{-2} whereas those fabricated by using brookite TiO_2 layer do not display any current density.^[174] There is considerable effect of solvent treatment and substrate temperature on the morphology and structure of bismuth-based perovskite films of $\text{MA}_3\text{Bi}_2\text{I}_9$. The electron transport layer of fluorinated perylene diimide (FPD) treated by solvent vapor annealing with chloroform reported an efficiency of 0.06% for substrate temperature at 75 °C. The perovskite solar cell $\text{MA}_3\text{Bi}_2\text{I}_9$ exhibited a small degradation after 17 d storage in ambient air conditions.^[245]

The concentration of perovskite solution also impacts the morphology and photovoltaic performance of spin-coated $\text{MA}_3\text{Bi}_2\text{I}_9$ solar cells. The fabricated cells displayed an efficiency of V_{OC} (0.73 V) and efficiency of 0.17% after 48 h in air. The solar cells exhibited 56% of peak efficiency and 84% of open-circuit voltage even after 300 h exposure in ambient air.^[246] The vapor-assisted solution process (VASP) applied to BiI_3 films by exposing them to $\text{CH}_3\text{NH}_3\text{I}$ vapors results in enhancement of film morphology, efficiency, and stability in ambient air. The solar cell fabricated using pure BiI_3 films and CH_3NH_3 vapors on mesoporous TiO_2 substrate displayed high SPCE up to 3.17% attributed to better morphology, improved device com-

position, reduced metallic content, and suitable optoelectronic properties of the fabricated material that maintained a stability for 60 d with only 0.1% drop in efficiency.^[247] The wide bandgap of lead-free perovskite devices ($E_g > 1.9$ eV) can be engineered to a narrow bandgap by incorporating triiodide into (4-methyl piperidinium)₃ Bi_2I_9 (MP- Bi_2I_9) that resulted in 0D perovskite (MP-T- BiI_6) (4-methyl piperidinium)₄ I_3BiI_6 . MP-T- BiI_6 displayed a narrow bandgap of 1.58 eV comparable to 1.5 eV of MAPbI_3 , hole mobility (≈ 12.8 $\text{cm}^2 \text{V}^{-1} \text{s}^{-1}$), and charge trap density ($\approx 1.13 \times 10^{10}$ cm^{-3}). The narrow bandgap signifies its potential to be used as an effective light absorber in perovskite solar cells.^[248] The solvent engineering method can be applied at bismuth-based perovskite to produce pinhole-free films of $\text{MA}_3\text{Bi}_2\text{I}_9$, Cs_3BiI_9 , or $(\text{MA})_3\text{Bi}_2\text{I}_9$. The fabricated $\text{MA}_3\text{Bi}_2\text{I}_9$ films are most suitable for efficient and stable perovskite solar cells than the pristine $\text{MA}_3\text{Bi}_2\text{I}_9$ films with pinholes.^[249] An enhanced open-circuit voltage of 0.84 V is obtained in $(\text{MA})_3\text{Bi}_2\text{I}_9$ perovskite by using ethanol as solvent.^[250] The film quality of $(\text{MA})_3\text{Bi}_2\text{I}_9$ can be enhanced by high-vacuum BiI_3 deposition and low-vacuum transformation of BiI_3 to $(\text{MA})_3\text{Bi}_2\text{I}_9$. The fabricated perovskite solar cells exhibited a SPCE of 1.64%, J_{SC} of 2.95 mA cm^{-2} , V_{OC} of 0.81 V, FF of 0.69, and long stability.^[251] 0D $\text{Cs}_3\text{Bi}_2\text{I}_9$ perovskite films in mesostructured perovskite solar cells exhibited a SPCE of 1.09% with a V_{OC} of 0.81 V, J_{SC} of 2.95 mA cm^{-2} , and FF of 0.69^[111] with a bandgap of 2.2 eV.

1D iodobismuthates consisting of 1D chain like BiI_4^- anions with edge-sharing BiI_6 octahedra have been prepared from aqueous solutions. The four reported compounds $\text{LiBiI}_4 \cdot 5\text{H}_2\text{O}$, $\text{MgBi}_2\text{I}_8 \cdot 8\text{H}_2\text{O}$, $\text{MnBi}_2\text{I}_8 \cdot 8\text{H}_2\text{O}$, and $\text{KBiI}_4 \cdot \text{H}_2\text{O}$ have direct bandgaps of 1.70–1.76 eV and can be used as potential light absorber.^[252] The 1,6 hexadiazonium bismuth halide perovskite (HDABiI_5) showing 1D chain like structure is prepared by solution method. The (HDABiI_5) m-str. perovskite displayed a SPCE of 0.027%, V_{OC} of 0.40 V, J_{SC} of 0.12 mA cm^{-2} , and FF of 0.43 with an optical bandgap of 2.05 eV.^[253] $\text{K}_3\text{Bi}_2\text{I}_9$ and $\text{Rb}_3\text{Bi}_2\text{I}_9$ are 2D layered defect perovskites prepared by solution method or solid-state reactions. $\text{K}_3\text{Bi}_2\text{I}_9$ and $\text{Rb}_3\text{Bi}_2\text{I}_9$ have a direct bandgap of 2.1 eV.^[239] The perovskite film $\text{CsBi}_3\text{I}_{10}$ has a layered 2D structure as evident from X-ray diffraction (XRD) pattern with a bandgap of 1.77 eV which is smaller than the bandgap of $\text{Cs}_3\text{Bi}_2\text{I}_9$ (2.03 eV), absorption coefficient 1.4×10^5 cm^{-1} . The perovskite solar cell with $\text{CsBi}_3\text{I}_{10}$ achieved a photocurrent up to 700 nm leading to better scope for use in solar cells.^[143] The $\text{Cs}_3\text{Bi}_2\text{I}_9$ films have a better film morphology and pinhole-free layers. The $\text{CsBi}_3\text{I}_{10}$ films as a light absorber in mesostructured solar cells displayed a SPCE of 0.4% whereas $\text{Cs}_3\text{Bi}_2\text{I}_9$ solar cells have displayed a SPCE of 0.02% only in same device architecture.^[143] Another 2D layered perovskite is $\text{MA}_3\text{Bi}_2\text{I}_9$ which is prepared from solution and has a bandgap of 2.04 eV which is smaller than that of $\text{K}_3\text{Bi}_2\text{I}_9$ and $\text{Rb}_3\text{Bi}_2\text{I}_9$ (2.1 eV).^[254,255] Bismuth-based 3D double perovskite has been proposed with a chemical formula $\text{A}_2\text{B}^{\text{I}}\text{Bi}^{\text{II}}\text{X}_6$ to maintain a charge neutrality of the perovskite material. The double perovskites like $\text{Cs}_2\text{AgBiX}_6$ (Br, Cl)^[254–257] and $(\text{MA})_2\text{KBiCl}_6$ ^[258] have been synthesized by using a solution method. It has been reported that $\text{Cs}_2\text{AgBiBr}_6$ ^[254] and $\text{Cs}_2\text{AgBiCl}_6$ have an indirect bandgap of 2.19 and 2.77 eV. $(\text{MA})_2\text{KBiCl}_6$ has too large bandgap of 3.04 eV to be suitable for use in perovskite solar cells.^[258] The DFT calculations have revealed that double

Table 9. PV parameters of bismuth-based perovskites.

Light absorber	E_g	V_{OC}	J_{SC}	FF	SPCE	Architecture	Ref.
MA ₃ Bi ₂ I ₉	2.11	0.35	1.16	0.46	0.19	FTO/TiO ₂ /mp-TiO ₂ /absorber/P3HT/Au	[127]
MA ₃ Bi ₂ I ₉	2.1	0.68	0.52	0.33	0.12	FTO/TiO ₂ /mp-TiO ₂ /absorber/Spiro-OMeTAD/Ag	[111]
MA ₃ Bi ₂ I ₉	2.26	0.72	0.49	0.31	0.11	FTO/TiO ₂ /absorber/Spiro-OMeTAD/Au	[128]
MA ₃ Bi ₂ I ₉	2.1	0.68	0.37	0.32	0.08	FTO/TiO ₂ /absorber/Spiro-OMeTAD/Au	[242]
MA ₃ Bi ₂ I ₉	–	0.56	0.83	0.49	0.26	FTO/TiO ₂ /mp-TiO ₂ /absorber/Spiro-OMeTAD/Au	[173]
MA ₃ Bi ₂ I ₉	–	0.51	0.94	0.61	0.31	FTO/TiO ₂ /mp-TiO ₂ /absorber/Spiro-OMeTAD/Au	[244]
MA ₃ Bi ₂ I ₉	2.1	0.65	1.10	0.50	0.36	FTO/TiO ₂ /mp-TiO ₂ /absorber/Spiro-OMeTAD/Au	[264]
MA ₃ Bi ₂ I ₉	2.22	0.83	1.39	0.34	0.39	ITO/PEDOT:PSS/absorber/C ₆₀ /BCP/Ag	[242]
MA ₃ Bi ₂ I ₉	2.1	0.67	1.0	0.62	0.42	ITO/TiO ₂ /mp-TiO ₂ /absorber/Spiro-OMeTAD/Ag	[240]
MA ₃ Bi ₂ I ₉	2.9	0.66	0.22	0.49	0.07	ITO/PEDOT:PSS/absorber/PCBM/Ca/Al	[143]
MA ₃ Bi ₂ I _{9-x} Cl _x	2.4	0.04	0.18	0.38	0.003	FTO/TiO ₂ /mp-TiO ₂ /absorber/Spiro-OMeTAD/Au	[111]
(MA ₃ Bi ₂ I ₉) _{0.2} (BiI ₃) _{0.8}	–	0.57	0.27	0.50	0.08	FTO/TiO ₂ /mp-TiO ₂ /absorber/PTAA/PIDT-DFBT/Ag	[128]
HDABiI ₅	–	0.40	0.12	0.43	0.027	FTO/c-TiO ₂ /HDABiI ₅ /mp-TiO ₂ /Spiro-OMeTAD/Au	[253]
Cs ₃ Bi ₂ I ₉	2.1	–	–	–	8.0	Glass/FTO/TiO ₂ /Cs ₃ Bi ₂ I ₉ /PTAA/Au	[141]
MA ₃ Bi ₂ I ₉ +FPDI	2.1	0.61	0.37	0.27	0.06	ITO/MA ₃ Bi ₂ I ₉ /Spiro-OMeTAD/MoO ₃ /Ag	[245]
AgBi ₂ I ₇	1.87	0.56	3.30	0.67	1.22	ITO/TiO ₂ /mp-TiO ₂ /absorber/P3HT/Ag	[265]
Cs ₂ AgBiBr ₆	2.21	0.98	3.93	0.63	2.43	FTO/c-TiO ₂ /mp-TiO ₂ /absorber/Spiro-OMeTAD/Au	[266]
CsBi ₃ I ₆	1.77	0.31	3.4	0.38	0.40	FTO/c-TiO ₂ /mp-TiO ₂ /absorber/P3HT/Ag	[143]
C ₆ H ₅ NBiI ₄	1.98	0.62	2.71	0.54	0.9	FTO/c-TiO ₂ /mp-TiO ₂ /absorber/ZrO ₂ /C	[242]
(H ₃ NC ₆ H ₁₂ NH ₃)BiI ₅	2.1	0.40	0.12	0.43	0.03	FTO/c-TiO ₂ /mp-TiO ₂ /absorber/Spiro-OMeTAD/Au	[143]
Cs ₃ Bi ₂ I ₉	2.03	0.02	0.18	0.37	0.02	FTO/TiO ₂ /mp-TiO ₂ /absorber/P3HT/Ag	[143]
Cs ₃ Bi ₂ I ₉	2.2	0.85	2.15	0.6	1.09	FTO/TiO ₂ /mp-TiO ₂ /absorber/Spiro-OMeTAD/Ag	[111]

perovskite (MA)₂TlBiI₆ has a bandgap of 2.00 V potential to be used as a lead-free perovskite material due to similar property as that of MAPbI₃ but Tl is toxic in nature.^[259] The bimetal iodide thin films AgBi₂I₇ show a SPCE of 1.22%, V_{OC} of 0.56 V, J_{SC} of 3.30 mA cm⁻², and FF of 1.87 with a better stability under ambient conditions.^[260] Using first principle calculations, a 3D double perovskite family has been revealed with optical bandgaps in the visible range and low carrier effective masses. The members of this family Cs₂CuBiX₆, Cs₂AgBiX₆, and CsAuBiX₆ have optical bandgaps in the range of 1.3–2.0, 1.6–2.7, and 0.5–1.6 eV, respectively.^[261]

The bismuth-based perovskite solar cells Cs₃Bi₂I₉ fabricated by glass/FTO/TiO₂/Cs₃Bi₂I₉/PTAA/Au architecture displayed an efficiency of 8%. The perovskite film of Cs₃Bi₂I₉ exhibited a pure crystalline phase and excellent thermal stability. The encapsulated perovskite cell displayed constant efficiency for more than 500 h as light absorber at 65 °C with humidity at 60–70% level. The stability is attributed to the large size of bismuth-based perovskite structure than lead-based perovskite structure.^[141] The lattice compression of 0D perovskite Cs₃Bi₂I₉ results in change in their structural, optical, and electrical properties. It is a result of lattice compression that there is an increase in exciton binding energy leading to an enhancement in emission under mild pressure. Bi–I bond contraction causes bandgap narrowing and an increase in metal halide orbital overlapping resulting from decrease in bridging Bi–I–Bi angle. These changes are reversible on decomposition. There is a semiconductor to conductor transition at ≈28 GPa due to decrease

in resistance thus leading to metallization of Cs₃Bi₂I₉.^[262] The high-quality polycrystalline films of Cs₃Bi₂I₉, Rb₃Bi₂I₉, and AgBi₂I₇ can be fabricated by two-step Co-evaporation process involving two square evaporation of CsI, RbI or AgI and BiI₃ and further annealing under BiI₃ vapors producing films with better pinhole-free morphology of films with average grain size >200 nm.^[263] Bismuth-based perovskite films can be further engineered to produce pinhole-free films of MA₃Bi₂I₉ and Cs₃Bi₂I₉. The MA₃Bi₂I₉ films are more suitable for perovskite solar cells than the pristine.^[141] **Table 9** shows some photovoltaic parameters of bismuth-based perovskites. **Figure 14** shows the SEM images of (MA)₃Bi₂I₉ without and with different concentration of NMP additives.^[244]

7.4. Antimony-Based Perovskites

Antimony is another potential candidate for replacing lead in perovskite solar cells. Antimony has the ability to form +3 ions with valence electronic configuration similar to that of divalent Pb²⁺. The trivalent Sb³⁺ has a small ionic radius (76 pm) as compared to that of divalent metal cation Pb²⁺ (119 pm) and Sn²⁺ (110 pm), having comparable electronegativity of (2.05) in comparison to Pb (2.33) and Sn (1.96). Antimony-based lead-free perovskites form a 0D dimer or a 2D layered structure with the typical basic formula A₃Sb₂X₆ where A is an organic or inorganic cation and X is a halogen.^[140] The choice of cationic or anionic species determines the structure and dimensions

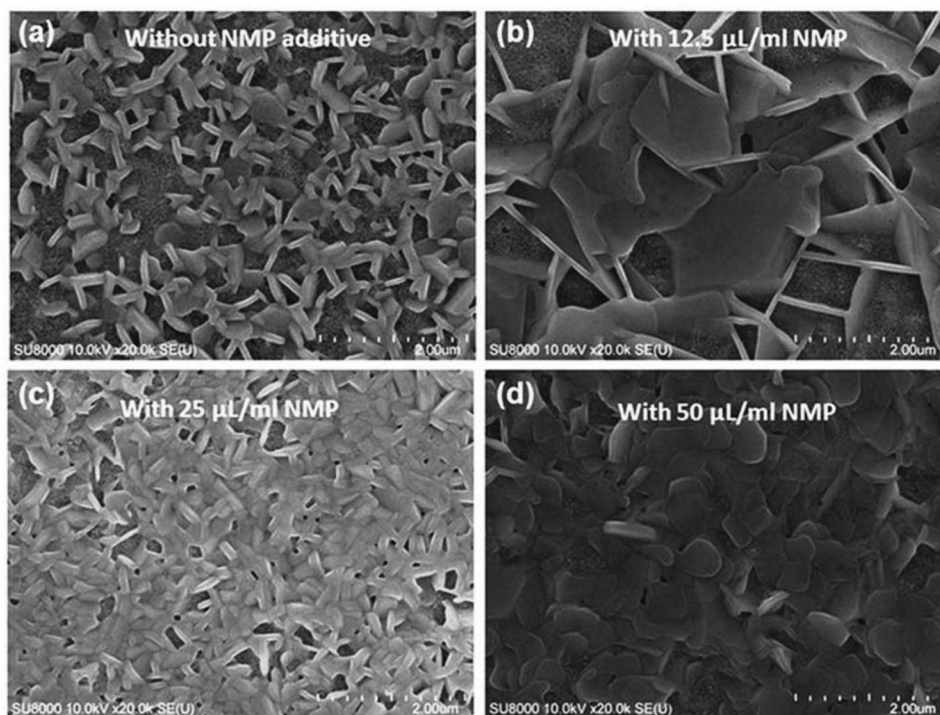


Figure 14. SEM images of $(\text{MA})_3\text{Bi}_2\text{I}_9$ without and with different concentration of NMP additives. Reproduced with permission.^[244] Copyright 2017, Royal Society of Chemistry.

of antimony-based perovskites used as light absorbers. In addition to it, the employed processing technique also effects the dimensions of the synthesized products. $\text{Cs}_3\text{Sb}_2\text{I}_9$ has an inclination to a 0D dimer form if it is prepared by solution process whereas it prefers a 3D layered structure when prepared through a solid-state or gas phase reaction. Saporov et al.^[140] carried out thin film preparation and characterization of $\text{Cs}_3\text{Sb}_2\text{I}_9$ thin films as light absorber in perovskites solar cell. $\text{Cs}_3\text{Sb}_2\text{I}_9$ film exists in two forms, viz., a 0D dimer form and a 2D layered form. The 0D dimer form of $\text{Cs}_3\text{Sb}_2\text{I}_9$ is prepared through reactions of CsI and SbI₃ in stoichiometric ratio of 3:2 in polar solvents. This film has an intense orange color and is stable under ambient air with an indirect bandgap of 2.06 eV whereas 2D layered films of $\text{Cs}_3\text{Sb}_2\text{I}_9$ are obtained through a solid-state or gas phase reactions, that is, by sequential deposition of CsI film through evaporation followed by annealing in SbI₃ vapor. The layered films display red color with a direct bandgap of 2.05 eV, high absorption coefficient of 10^5 cm^{-1} , and ionization energy of 5.6 eV with better stability in air. However, SPCE values of the perovskites solar device with layered forms of $\text{Cs}_3\text{Sb}_2\text{I}_9$ as light absorber have minimal values of SPCE close to 1% with V_{OC} of 0.30 V and a J_{SC} below 0.1 mA cm^{-2} indicating a very low overall photovoltaic performance attributed to the presence of deep defects that promote nonradiative recombination. Boopathi et al.^[181] synthesized 0D dimer form of $\text{Cs}_3\text{Sb}_2\text{I}_9$ as a light absorber and reported a SPCE of 0.84%, J_{SC} of 2.91 mA cm^{-2} , V_{OC} of 0.60 V, and FF of 0.48 for $\text{Cs}_3\text{Sb}_2\text{I}_9$ with addition of HI.^[181]

A 2D layered perovskite was synthesized by using the mixture Cs^+ and MA^+ as the A-site cation via solution process as opposite to reported by Saporov et al. where A-site cation

is substituted by a smaller cation Rb^+ , a 2D layered phase is achieved due to smaller radius of Rb^+ (1.72 \AA) as compared to that of Cs^+ (1.88 \AA) via solution processing through the reaction of RbI and SbI₃. Using DFT calculations, the comparison of formation energies of 2D layered and 1D dimer forms of $\text{A}_3\text{Sb}_2\text{I}_9$ (A-Cs, Rb) reveals that the formation energy difference of 0.25 eV is higher for Rb-based perovskites than that of cesium-based counterparts having this difference equal to 0.1 eV thus clearly indicating the increased inclination of $\text{Rb}_3\text{Sb}_2\text{I}_9$ for layered phase. The layered perovskites $\text{Rb}_3\text{Sb}_2\text{I}_9$ achieved a SPCE of 0.66% with V_{OC} of 0.55 V, J_{SC} of 2.11 mA cm^{-2} , and FF of 0.57.^[267] In addition, they show thermal stability up to 250 °C and no phase transition is reported in between -40 and 200 °C. The light absorption coefficient of $\text{Rb}_3\text{Sb}_2\text{I}_9$ films is greater than $1 \times 10^5 \text{ cm}^{-1}$ with an indirect bandgap of 2.1 eV. A direct transition at 2.24 eV was calculated for $\text{Rb}_3\text{Sb}_2\text{I}_9$ as compared to 2.05 eV for the bandgap of cesium. $\text{MA}_3\text{Sb}_2\text{I}_9$ only forms a 0D dimer structure. The octahedral anionic metal halide $[\text{Sb}_2\text{I}_9]^{3-}$ surround the MA^+ cations. Hebig et al. first prepared the flat and thin films of $\text{MA}_3\text{Sb}_2\text{I}_9$ by spin-coating process followed by toluene treatment. The obtained thin films show a peak absorption coefficient above 10^5 cm^{-1} and an optical bandgap of 2.14 eV. The fabricated planar perovskite cell achieved SPCE of 0.49%, V_{OC} of 0.90 V, J_{SC} of 1.0 mA cm^{-2} , and FF of 0.55.^[147] Boopathi et al.^[181] synthesized 0D $(\text{MA})_3\text{Sb}_2\text{I}_9$ films for use as light absorbers in perovskite solar cells with HI as an additive. The addition of HI into the films resulted in an increase in light absorption in the visible wavelength regions about 400 nm. The XRD spectra studies revealed that the addition of HI leads to a better crystallinity, phase purity, and quality of the film. It reduces the bandgap thereby enhancing the light

absorption toward higher wavelength regions. The achieved values of photovoltaic parameters with or without addition of HI are shown in Table 9. The nonsolvent treatment was investigated to enhance the surface morphology of Sn-based dimer by using HI-CB to enhance the heterogenous nucleation of Sb-based perovskite used as light absorber.^[268] The interlayer of HI-CB acted as a hydrophobic scaffold for the growth of $(\text{CH}_3\text{NH}_3)_3\text{Sb}_2\text{I}_9$ crystals. The interlayer decreases the number of voids and enhances the quality of film. The fabricated films achieved a SPCE of 2.77%.^[268] The DFT calculations have revealed that the most stable mixed metal organic-inorganic perovskite MA_2SbI_6 has a bandgap of 2.0 eV which is further confirmed by using XRD characterization of MA_2SbI_6 as a light absorber that has displayed an optical bandgap of 1.93 eV and good stability in air.^[269]

A larger A-site cation was used to synthesize high-quality films of 2D layered phase in $(\text{CH}_3\text{NH}_3)_3\text{Sb}_2\text{Cl}_x\text{I}_{9-x}$. The induction of methylammonium chloride into precursor solutions inhibits the formation of the undesirable 0D dimer phase leading to synthesis of high-quality films of 2D layered phase that is favorable for application in lead-free perovskite solar cells. These films achieved a SPCE of 2%.^[270] Similarly, Zuo and Ding synthesized a family of perovskite light absorbers $(\text{NH}_4)_3\text{Sb}_2\text{I}_x\text{Br}_{9-x}$ ($0 \leq x \leq 9$).^[116] These materials display good solubility in ethanol. The optical light absorption can be adjusted by adjusting the ratio of I and Br content. The absorption onset for films changes from 558 to 453 nm as x changes from 9 to 0. The single crystals of $(\text{NH}_4)_3\text{Sb}_2\text{I}_9$ showed a hole mobility of $12.3 \text{ cm}^2 \text{ V}^{-1} \text{ s}^{-1}$ and electron mobility of $12.3 \text{ cm}^2 \text{ V}^{-1} \text{ s}^{-1}$ achieving a V_{OC} of 1.03 V and SPCE of 0.51% only.^[116] The use of methylammonium antimony sulfur diiodide (MASbSI_2) as light absorber for lead-free perovskite solar cells was first reported by Nie et al.^[271] The MASbSI_2 is prepared through spin-coating and thermal annealing of MAI solution on SbSI under mild temperature conditions. The fabricated MASbSI_2 as light absorber achieved SPCE of 3.08% under the standard illumination condition of 100 mW cm^{-2} . They achieved photovoltaic performance in MASbSI_2 solar cells as of J_{SC} (8.12 mA cm^{-2}), V_{OC} (0.65 V), FF (0.58), and SPCE of 3.08%. Unencapsulated cells stored in dark ambient conditions (humidity $\approx 60\%$, temperature 25°C) retained 90% of their initial efficiency. The use of chalcogenide and halide mixed perovskite materials can be an effective strategy for fabrication of efficient, cheap, and stable solar cells. A mixed metal layered perovskite $\text{Cs}_4\text{CuSb}_2\text{Cl}_{12}$ as a light absorber for perovskite solar cells has been reported.^[272] The layered perovskite $\text{Cs}_4\text{CuSb}_2\text{Cl}_{12}$ is formed by incorporating Cu^{2+} and Sb^{2+} cations into layers that has a bandgap of 1 eV and conductivity is one order of magnitude greater than MAPbI_3 . $\text{Cs}_4\text{CuSb}_2\text{Cl}_{12}$ has high photo and thermal stability and resistance to humidity. The achieved photovoltaic properties promise the excellent use of this material in optical light absorbing layer for perovskite solar cells.^[272]

The normal (n-i-p) structured solar cells show better photovoltaic performance as compared to inverted structures. Baranwal et al. have proved it by making a comparison between the normal [n-i-p-TiO₂-perovskite-Spiro-OMeTAD] and inverted [p-i-n-NiO-perovskite-PCBM] structures.^[273] ABX_3 compounds can form perovskite like 3D crystals frameworks like bromoantimonate (V) (N-EtPY) (SbBr_6) with short interhalide contacts.^[295]

ASbBr_2 is a black crystalline solid with an optical bandgap of 1.65 eV that is much lower than that of conventional MAPbBr_3 of 2.3 eV. The planar cells with standard architecture using P3HT as a HTM layer displayed better photovoltaic parameters as J_{SC} (5.1 mA cm^{-2}), V_{OC} (1.285 V), FF (0.58), and SPCE of 3.8% whereas the inverted architecture using a double-layer PDI as ETL films is fabricated by depositing first by spin-coating from chlorobenzene solution followed by evaporation of additional layers of the material in vacuum and has shown J_{SC} of 5.1 mA cm^{-2} , V_{OC} of 1.030 V, FF of 0.58, and SPCE of 3.1% only.^[274] The effect of substitution of antimony (Sb) with bismuth (Bi) in a 2D mixed layered perovskite $(\text{NH}_4)_3(\text{Sb}_{1-x}\text{Bi}_x)_2\text{I}_9$ as light absorber has been investigated extensively. The partial substitution of Sb with Bi did not change the structure of the crystal but enhanced the volume of the unit cell. The XRD patterns did not show any impurity phase with Bi addition but peaks shift toward lower angles as content of Bi increases showing an increase in unit cell size due to induction of bulkier bismuth cation. The films showed typical features of direct bandgaps due to strong absorption above 2.7 eV and indirect bandgaps because of absence of photoluminescence with long carrier lifetimes. The absorption coefficient increases due to increase in density of states in conduction band whereas bandgap reduces from 2.27 to 2.16 eV^[275] for 5% Bi film due to higher spin-orbit coupling. Bismuth pushes the conduction band downward as predicted by DFT calculations. It also shifts the valence band downward, thereby enhancing the ionization potential values from 5.78 to 5.9 eV for incorporation of 50% bismuth content. The Urbach energies also showed a decrease with an increase in bismuth content. The carrier lifetimes do not follow a particular trend with increase in Bi incorporation in the perovskite film as $184 \pm 8 \text{ ns}$ (0% Bi), $94 \pm 25 \text{ ns}$ (20% Bi), $149 \pm 12 \text{ ns}$ (40% Bi), $91 \pm 13 \text{ ns}$ (50% Bi) as there is decrease in deep defects near the conduction band side due to addition of Bi but simultaneously there is an increase in defects near the valence band. The AC Hall measurements predicted the p-type conduction band behavior for $(\text{NH}_4)_3\text{Sb}_2\text{I}_9$ with a carrier concentration of $3.95 \times 10^{15} \text{ cm}^{-3}$ and mobility of $0.5 \pm 0.5 \text{ cm}^2 \text{ V}^{-1} \text{ s}^{-1}$. The carrier density is reduced by incorporating 10 and 20% of Bi owing to increase in mobility that got doubled to more than $1 \text{ cm}^2 \text{ V}^{-1} \text{ s}^{-1}$ thus the material undergoes a p-to-n transition for higher Bi contents (40%, 50%) that clearly indicates the changing nature of defects in the material. Therefore, the films show both p and n-type regions. In order to increase p and n regions, electrical poling was used to adjust the load composition of the film by creating ionic drift. The unpoled $(\text{NH}_4)_3\text{Sb}_2\text{I}_9$ (p-type) showed linear photocurrent voltage relationship. The device was negatively poled by applying a bias of $-2 \text{ V } \mu\text{m}^{-1}$ to electrode B under illumination by a blue LED (455 nm , power 1.4 mW mm^{-2}) for 2 min.^[275] The V - I curves after negative poling indicates photovoltaic effect with V_{OC} close to 200 mV which flipped to -0.2 V on \pm poling.^[275] The material exhibited measurable photocurrent densities at short-circuit conditions. The directions of dark and photocurrent densities were opposite resulting in a switch of current direction on illumination due to presence of opposite fields in the same compound. A negative voltage close to -0.6 V is required to achieve zero current condition in dark as opposed to $+0.2 \text{ V}$ required under illumination. Table 10 shows some photovoltaic parameters of

Table 10. Antimony-based lead-free perovskites used as light absorber.

Light absorber	E_g	J_{sc}	V_{oc}	FF	SPCE	Architecture	Ref.
$Cs_3Sb_2I_9$	2.05	<0.1	0.31	–	<1.0	FTO/C-TiO ₂ /absorber/PTAA/Au	[140]
$Cs_3Sb_2I_9$	2.30	2.34	0.62	0.46	0.67	ITO/PEDOT:PSS/absorber/PC ₆₁ BM/C ₆₀ /BCP/Al	[181]
$Cs_3Sb_2I_9$ +HI	2.0	2.91	0.60	0.48	0.84	ITO/PEDOT:PSS/absorber/PC ₆₁ BM/C ₆₀ /BCP/Al	[181]
$Rb_3Sb_2I_9$	2.1	2.11	0.55	0.57	0.66	FTO/C-TiO ₂ /mp-TiO ₂ /absorber/PolyTPD/Au	[267]
$MA_3Sb_2I_9$	2.14	1.0	0.90	0.55	0.49	ITO/PEDOT:PSS/absorber/PC ₆₁ BM/nano-ZnO/Al	[147]
$MA_3Sb_2I_9$	2.20	3.81	0.64	0.45	1.11	ITO/PEDOT:PSS/absorber/PC ₆₁ BM/CO ₆₀ /BCP/Al	[181]
$MA_3Sb_2I_9$ +HI	1.95	5.41	0.62	0.60	2.04	ITO/PEDOT:PSS/absorber/PC ₆₁ BM/CO ₆₀ /BCP/Al	[181]
$(NH_4)_3Sb_2IXBr_{9-x}$	2.27	1.15	1.03	0.42	0.51	ITO/PEDOT:PSS/absorber/PC ₆₁ BM/Al	[116]
MASbI ₂	2.03	8.12	0.65	0.58	3.08	FTO/BL/mp-TiO ₂ /absorber/PCPD/TBT/PEDOT:PSS/Au	[271]
$Cs_4CuSb_2Cl_{12}$	1.0	–	–	–	0.30	–	[272]
(N-EtPY)SbBr ₆ (standard)	1.65	5.1	1.285	0.58	3.8	ITO/C-TiO _x /absorber/P3HT/Au	[274]
(N-EtPY)SbBr ₄ (inverted)	1.65	5.1	1.030	0.58	3.1	ITO/PEDOT:PSS/absorber/PD1/Ag	[274]
$CH_3Sc(NH_2)_2SbA_3$	2.41–3.34	–	–	–	–	–	[275]

antimony-based lead-free perovskites. The device configuration is shown in **Figure 15** for the switchable photovoltaic device containing $(NH_4)_3(Sb_{(1-x)}Bi_x)_2I_9$ perovskite material.^[275]

7.5. Copper-Based Perovskites

The divalent Cu^{2+} cation is another suitable element for Pb^{2+} substitution as Cu^{2+} has nontoxic nature. Cu^{2+} has a small ionic radius (73 pm) as compared to Pb^{2+} (119 pm) and Sn^{2+} (110 pm). The divalent Cu^{2+} is more stable in air than Sn^{2+} and Ge^{2+} .^[135,136] Cu-based perovskites usually form 2D layered perovskite structures owing to their smaller ionic radii with general formula $(RNH_3)_2CuX_4$ where RNH_3^+ can be aliphatic or aromatic cation and X is a halogen. They can be easily prepared under suitable conditions by solution method. A 2D cupric perovskite solar cell $[p-F-C_6H_5C_2H_4-NH_3]_2CuBr_4$ and $(CH_3(CH_2)_3NH_3)_2-CuBr_4$ with absorption range from 300 to 750 nm has been reported. The achieved SPCE values of the fabricated perovskite solar cell are 0.51 and 0.63%, respectively,

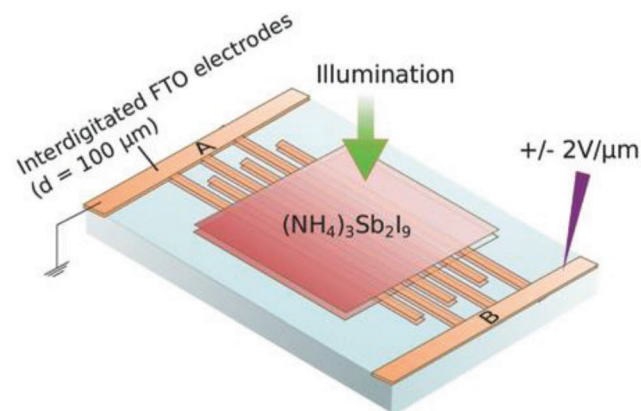


Figure 15. Schematic of the device configuration used for switchable photovoltaic study using $(NH_4)_3(Sb_{(1-x)}Bi_x)_2I_9$ perovskite material. Reproduced with permission.^[275] Copyright 2018, Wiley-VCH.

with good air stability of less than 5% decrease of efficiencies after 1 d in air with humidity of 50% without encapsulation. The reported photovoltaic parameters of the fabricated device are shown in Table 10.^[135] The solar cells based on $MA_2CuCl_xBr_{4-x}$ have been investigated in order to study the photovoltaic performance and stability of Cu-based mixed halides. By tuning Cl/Br ratio, the optical absorption can be extended in the near-infrared region. The small quantity of Cl^- enhances the stability and crystallization of the perovskite material. Among all the investigated light absorbers, the highest SPCE of 0.17% is achieved using $MA_2CuCl_2Br_2$ as light absorber. The minimal values of SPCE are attributed to reduction of Cu^{2+} and low absorption coefficient. The formation of Cu^{2+} ions was found to be responsible for the green photoluminescence of this material. $(MA)_2CuCl_2Br_2$ and $(MA)_2CuCl_{0.5}Br_{3.5}$ are found to be more stable under ambient conditions. The achieved values of photovoltaic parameters are shown in Table 10.^[136] It has been found that adding a small amount of $CuBr_2$ into $MAPbI_3$ remarkably enhances its morphology and efficiency but it is still under investigation whether Cu^{2+} can actually act as substitute for Pb^{2+} .^[276]

Li et al. investigated and characterized highly stable Cu-based perovskite films $C_6H_4NH_2CuBr_2I$ exhibiting extraordinary hydrophobic behavior with a contact angle of $\approx 90^\circ$. The XRD patterns of the perovskite films did not report any change even after 4 h of being immersed in water. The UV absorption of these films revealed their excellent absorption over the entire visible spectrum with low values of SPCE of $\approx 0.5\%$ attributed to low absorption coefficient and heavy mass of holes.^[137] The other Cu-based perovskite solar cells $(CH_3NH_3)_2CuCl_4$ and $(CH_3NH_3)_2CuCl_2X_2$ [X = I, Br] were fabricated through grinding milling process by Elseman and team and on characterization by XRD reveals that $(CH_3NH_3)_2CuCl_4$ has monoclinic crystal structure and $(CH_3NH_3)_2CuCl_2Br_2$ is crystallized with an orthorhombic structure. The tolerance factor and octahedral factor calculated for $(CH_3NH_3)_2CuCl_4$ were found to be 1.004 and 0.403, respectively, by assuming the ionic radius of methylammonium to be 18 pm. The calculated values are out of the optimum range of $0.8 < t < 0.9$ and $0.42 < u < 0.895$ for a stable 3D

Table 11. Photovoltaic parameters of reported Cu-based perovskites.

Light absorber	J_{SC} [mA cm^{-2}]	V_{OC}	PCE	FF	E_g	Architecture	Ref.
$(\text{CH}_3(\text{CH}_2)_3\text{NH}_3)_2\text{CuBr}_4$	1.78	0.88	0.63	0.40	1.76	FTO/C-TiO ₂ /mp-TiO ₂ /absorber/Spiro-OMeTAD/Ag	[135]
$(p\text{-F-C}_6\text{H}_5\text{C}_2\text{H}_4\text{-NH}_3)_2\text{CuBr}_4$	1.46	0.87	0.51	0.40	1.74	FTO/TiO ₂ /absorber/Spiro-OMeTADLiTFSI/Ag	[135]
$\text{MA}_2\text{CuCl}_2\text{Br}_2$	0.22	0.26	0.02	0.32	2.12	FTO/C-TiO ₂ /mp-TiO ₂ /absorber/Spiro-OMeTAD/Au	[136]
$\text{MA}_2\text{CuCl}_{0.5}\text{Br}_{3.5}$	0.21	0.29	0.002	0.28	1.8	FTO/C-TiO ₂ /mp-TiO ₂ /absorber/Spiro-OMeTAD/Au	[136]
$\text{C}_6\text{H}_4\text{NH}_2\text{CuBr}_2\text{I}$	6.20	0.20	0.46	0.46	1.64	FTO/C-TiO ₂ /mp-TiO ₂ /absorber/ZrO ₂ /C	[137]
$(\text{CH}_3\text{NH}_3)_2\text{CuCl}_4$	8.12	0.56	2.41	0.52	2.36	Glass/FTO/TiO ₂ /absorber/Spiro-OMeTAD/Au	[277]
$(\text{CH}_3\text{NH}_3)_2\text{CuCl}_2\text{I}_2$	6.78	0.54	1.75	0.47	1.90	Glass/FTO/TiO ₂ /absorber/Spiro-OMeTAD/Au	[277]
$(\text{CH}_3\text{NH}_3)_2\text{CuCl}_2\text{Br}_2$	3.35	0.58	0.99	0.50	1.04	Glass/FTO/TiO ₂ /absorber/Spiro-OMeTAD/Au	[277]

perovskite structure thus it crystallizes into 2D structures.^[277] It has been observed that the substitution of Cl⁻ with I⁻ or Br⁻ has different effects on bond angles, unit cell dimensions, and ionic radius. The achieved photovoltaic parameters are depicted in **Table 11**. The low SPCE values of $(\text{CH}_3\text{NH}_3)_2\text{CuCl}_2\text{Br}_2$ are due to reduction of Cu²⁺ caused by the higher trap density. The chemical structures and the performance of Cu-based perovskite solar cells (a) $(\text{CH}_3\text{NH}_3)_2\text{CuCl}_4$, (b) $(\text{CH}_3\text{NH}_3)_2\text{CuCl}_2\text{I}_2$, and (c) $(\text{CH}_3\text{NH}_3)_2\text{CuCl}_2\text{Br}_2$ powders, (d) current–voltage curve, and (e) EQE spectra of solar cells are shown in **Figure 16**.^[277]

7.6. Other Potential Candidates for Lead-Free Perovskites

The alkaline earth metals Be²⁺, Mg²⁺, Ca²⁺, Sr²⁺, and Ba²⁺ have been investigated as an alternative to lead in lead-free

perovskite. However, the optical bandgap of Be²⁺ is too high to be used for PV applications. Mg²⁺ despite having a smaller ionic radius (72 pm) can replace Pb²⁺ (119 pm) to form a stable magnesium-based perovskite.^[278,279] The replacement of Pb²⁺ by Mg²⁺ results in a lead-free magnesium-based AMG₃ perovskite that exhibits low effective masses, direct optical absorption coefficients, and direct bandgap tunable within the visible region of electromagnetic spectrum depending upon the size of A-site cation.^[278,279] The bandgaps of magnesium-based perovskite AMgI₃ featured an increasing trend with A-site cations such as FA⁺, MA⁺, and Cs⁺ having values 0.9, 1.5, and 1.7 eV, respectively.^[278] The study of photoluminescence properties of Eu²⁺-doped CsMI₃[M=Mg, Ca, Sr] perovskite has revealed that the Eu²⁺-doped CsMgI₃ and CsSrI₃ displayed a redshift emission with respect to Eu²⁺-doped CsCaI₃ perovskite. Eu²⁺-doped CsMgI₃ crystallizes in a distorted hexagonal CsNiCl₃ structure

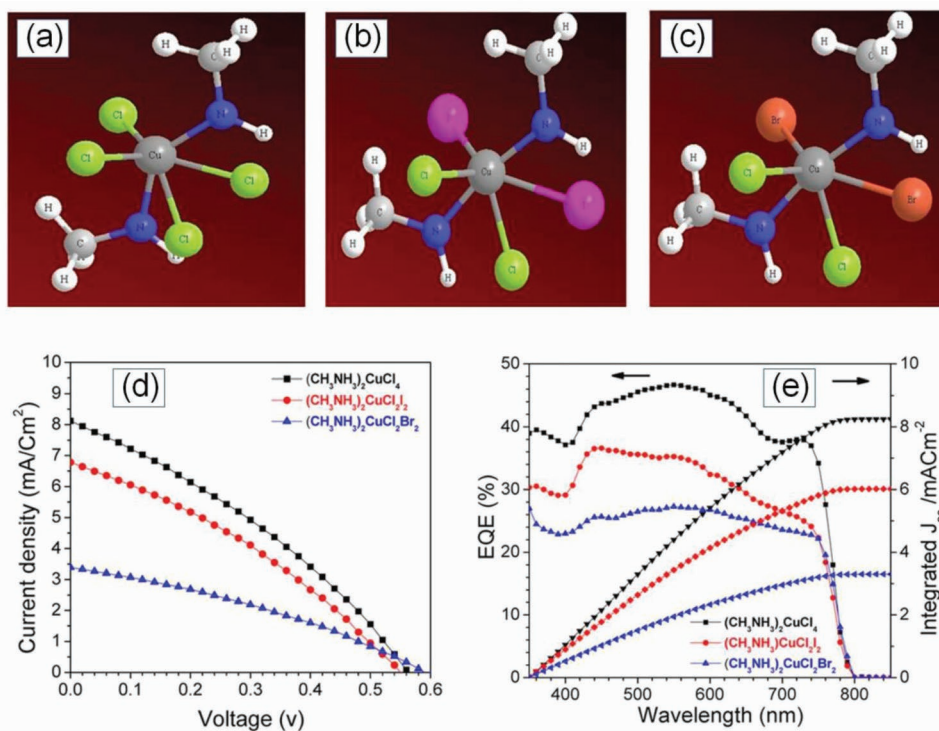


Figure 16. Chemical structures of perovskite solar cells using a) $(\text{CH}_3\text{NH}_3)_2\text{CuCl}_4$, b) $(\text{CH}_3\text{NH}_3)_2\text{CuCl}_2\text{I}_2$, and c) $(\text{CH}_3\text{NH}_3)_2\text{CuCl}_2\text{Br}_2$ powders. d) Current–voltage curve and e) EQE spectra of solar cells. Reproduced with permission.^[277] Copyright 2018, American Chemical Society.

whereas CsCaI₃ crystallizes in an orthorhombic GdFeO₃ structure and CsSrI₃ crystallizes in a filled PuBr₃ structure.^[280]

The divalent Ca²⁺ has an ionic radius (100 pm) comparable to that of Pb²⁺ (119 pm)^[281,282] whereas Sr²⁺ (118 pm) has a similar ionic radii to Pb²⁺ (119 pm).^[283] The divalent Ba²⁺ has an ionic radii of 135 pm larger than that of Pb²⁺ (119 pm).^[283] The DFT calculations have reported bandgaps of MACaI₃, MASrI₃, and MABaI₃ to be 2.95, 3.6, and 3.3 eV, respectively.^[281,283] However, MASrI₃ and MABaI₃ do have large bandgaps leading to light absorption in UV region.^[281,283] The replacement of Pb²⁺ by Ca²⁺ and Sr²⁺ in MAPbI₃ perovskite thin films has reported an increase in long carrier lifetime and fill factors of the devices reaching 0.85.^[284] Transition metals such as Ti, V, Mn, Ni, Pd, Fe, Cu, Zn, Cd, and Hg have been researched extensively for lead replacement in lead-free perovskite. The crystals of CsNiX₃ perovskite have been synthesized by hydrothermal method having BaNiO₃ structure consisting of a face-sharing NiX₆ octahedral separated by CsX₁₂ cuboctahedra.^[285] The 2D layered perovskite structure of bis(alkyl ammonium)metal(II) tetrahalide (C_nH_{2n-1}NH₃)₂MX₄ and (α,w) polymethylene diammonium metal (II) tetrahalide NH₃(CH₂)_mNH₃MX₄ with M—Cd, Cu, Fe, Mn, or Pd and X—Br, Cl have been synthesized and a large single perovskite crystal has been obtained.^[286] The divalent Fe²⁺ has a smaller ionic radius (78 pm) as compared to Pb²⁺ (119 pm) that does not allow the formation of 3D perovskite structure. Iron-based 2D layered perovskite (CH₃NH₃)₂(FeCl₄) exhibits a canted anti-ferromagnetism in a magnetic field of strength greater than 2000 Oe and it also exhibits the phase transition from a high symmetry to a low symmetry.^[287] The magnetic susceptibility of (CH₃NH₃)₂FeCl₃Br perovskite depends upon the strength of applied magnetic field. Also, the size of halide anion has a direct effect on the canted spin.^[288] Just like Sn-based perovskite, iron-based perovskite is also unstable due to oxidation of Fe²⁺ to Fe³⁺.^[289] The divalent rare earth Eu²⁺-based perovskite (C₄H₉NH₃)₂EuI₄ has been synthesized through low-temperature solid-state reactions.^[290] The effect of doping of rare earth metal ions such as Eu²⁺, Tm²⁺, and Yb²⁺ in CsAX₃(A—Ca, Mg, Sr) perovskite has been investigated extensively.^[280,291,292] Another transition metal gold has been investigated for its potential in a perovskite framework. The optical properties of gold-based 2D organic mixed Au^I/Au^{III} layered perovskite have been reported with [AuI₂]⁻/[AuI₄]⁻ layers supported by I₃⁻ ions and appropriate organic dications.^[293] The [NH₃(CH₂)₇NH₃]₂ [Au^I I₂] [Au^{III} I₄](I₃)₂ and [NH₃(CH₂)₈NH₃]₂ (Au^I I₂) (Au^{III} I₄)(I₃)₂ perovskite exhibited a bandgap of 0.95 and 1.14 eV, respectively. The low bandgaps are attributed to the induced electronic interactions between [Au^I I₂]⁻ and [Au^{III} I₄]⁻ units and I₃⁻ ions.^[293] Another transition metal tellurium-based vacancy order perovskite Cs₂TeI₆ has been reported that consists of a face-centered lattice of [TeI₆]⁴⁻ units with Cs²⁺ cations occupying the cuboctahedral position. This material do possess an indirect bandgap, electronic dispersion, and is intolerant to formation of defects that is not suitable for PV applications as per current research.^[210] Transition metal titanium-based perovskite thin films Cs₂TiBr₆ have been prepared through low-temperature-based method having a bandgap of 1.8 eV that is comparable to eV of lead halide perovskite, balanced carrier diffusion lengths > 100 nm, and highly stable under environmental stresses. The fabricated device exhibited a SPCE of 3.3%. The

incorporation of C₆₀ interfacial layer between the Cs₂TiBr₆ light absorber thin films and TiO₂ ETM resulted in a V_{OC} of 1.02 V in a reverse scan direction and also enhanced other photovoltaic parameters. The thin films are highly stable under ambient conditions.^[294] By the application of split anion approach to MAPbI₃, the replacement of Pb²⁺ with Bi³⁺ and I⁻ with Se⁻ or S⁻ is done to maintain the charge neutrality thus resulting in lead-free perovskite CH₃NH₃BiSeI₂, and CH₃NH₃BeSI₂ has been reported exhibiting a direct bandgap of 1.3–1.4 eV suitable for photovoltaic applications.^[295] **Figure 17** shows the atomic structure and bandgap diagram of CH₃NH₃PbI₃ and MABiSeI₂ and a schematic illustrating the split-anion approach to replace Pb in CH₃NH₃PbI₃.^[295]

Lead-free perovskite with mixed chalcogen and halogen anion AB(Ch, X)₃ where A: Ca or Ba, B: Sb or Bi, X: halogen, Ch: chalcogen has been investigated by using DFT calculations and solid-state reactions that revealed their thermodynamically unstable nature, that is, their liability to decompose into ternary or binary secondary phases or form phases with nonperovskite structure. The synthesis of mixed perovskite with chalcogen and halogen anions has not been possible due to their unstable nature.^[296] The bandgaps of chalcogenide perovskite CaTiS₃, BaZrS₃, CaZrSe₃, and CaHfSe₃ with a distorted structure are within the suitable range for photovoltaic performance. Due to their suitable optical absorption properties, chalcogenide perovskite can be the potential candidates to combat the instability and toxicity issues.^[297] The synthesis of polycrystalline chalcogenide perovskite BaZrO₃, CdZrO₃, SrTiS₃, SrZrS₃, and BsZr(O_xI_{3-x})₃ has been reported by sulfonation of oxide perovskite by CS₂. The BaZrS₃ exhibited a distorted perovskite structure as evident from XRD pattern, with an optical absorption from UV to visible region. The perovskite material displayed photoluminescence in visible region and has an excellent stability in ambient air as compared to lead-based halide perovskites.^[298] The quaternary halide double perovskite employing lanthanides (La³⁺, Ce³⁺, Pr³⁺, Nd³⁺, Sm³⁺, Eu³⁺, Gd³⁺, Dy³⁺, Er³⁺, Tm³⁺, Lu³⁺) and actinides (Pu³⁺, Am³⁺, Bk³⁺) has been investigated but no PV performance has been reported.^[299,300] **Table 12** summarizes the stability of lead-free perovskites.

8. Recent Research on Lead-Free Perovskites

In order to explore the potential material whose properties can be tailored to be used as a light absorber in a perovskite solar cell, a lot of research is being carried out at present. Research is going on to explore a perovskite material that is lead-free, nontoxic, have low fabrication cost, easy fabrication technique, higher SPCE, and better stability in air, moisture, and heat. In an attempt to synthesize a low-cost lead-free perovskite solar cell, the CH₃NH₃SnBr_xCl_{3-x} crystals with a trigonal phase have been synthesized via aqueous solution based method by a reaction between HCl and H₃PO₂ without taking into account any protection against moisture. The synthesized crystals exhibit various low-frequency vibrational modes of Sn—Cl and Sn—Br.^[261] Recent studies of lead-free perovskite have shown that the hot antisolvent treatment of perovskite film increases its coverage and inhibits electrical shunting in photovoltaic device. Also, the average crystallite size increases due to

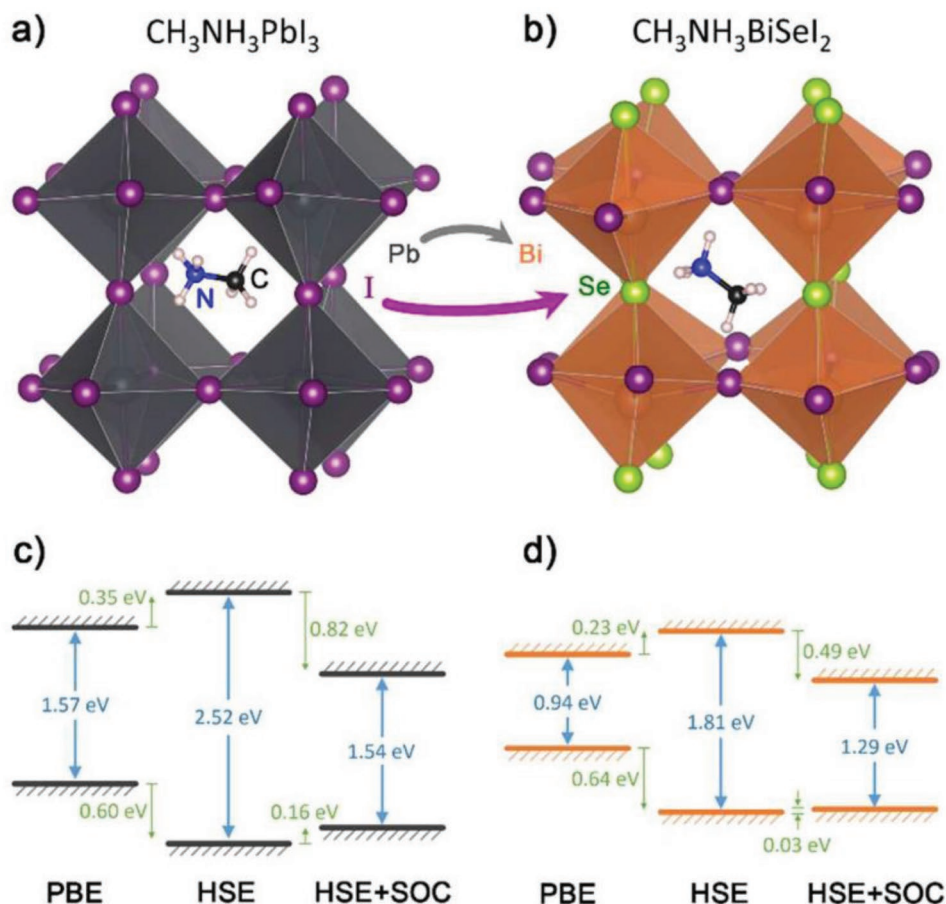


Figure 17. a,b) Atomic structures of $\text{CH}_3\text{NH}_3\text{PbI}_3$ and $\text{CH}_3\text{NH}_3\text{BiSe}_2$ and a schematic illustrating the split-anion approach to replacing Pb in $\text{CH}_3\text{NH}_3\text{PbI}_3$. c,d) The calculated bandgaps of $\text{CH}_3\text{NH}_3\text{PbI}_3$ and $\text{CH}_3\text{NH}_3\text{BiSe}_2$, respectively, using improved methods from PBE, HSE to HSE+SOC. The alignment of the band edge positions was obtained by assuming that the reference potentials from different methods are the same. Reproduced with permission.^[295] Copyright 2016, Royal Society of Chemistry.

annealing under a low partial pressure of dimethyl sulfoxide vapor. The topographical and electrical qualities of the perovskite film are enhanced facilitating the fabrication of tin-based perovskite solar cell with a SPCE of over 7%.^[301] The effect of additives on the stability of lead-free CsSnI_3 perovskite films has been studied by using first principle based calculations. It has been reported that the additives effectively passivate the surface and enhance the stability of CsSnI_3 films. The addition of SnBr_2 as an additive in CsSnI_3 films resulted in a SPCE of 4.3% with 100 h of stability.^[302]

An additional additive formamidinium thiocyanate into quasi-2D tin perovskite suppresses the oxidation of the material during film formation resulting in a highly crystalline structure with a coarser perovskite grain. The fabricated tin-based perovskite solar cell reported a SPCE of 8.17% under a reverse scan and a steady-state efficiency of 7.84%. The fabricated device retained 90% of its efficiency after 1000 h in a glove box filled with nitrogen.^[303] Another study on mixed tin-germanium perovskite solar cell $\text{FA}_{0.75}\text{MA}_{0.25}\text{Sn}_{1-x}\text{Ge}_x\text{I}_3$ has reported that most of the Ge atoms passivate the graded structure of tin perovskite. Upon doping with 5 wt% of Ge, the reported J_{SC} (19.8 mA cm^{-2}), FF (0.55), and SPCE (4.48%) have shown

an increasing trend as compared to 0 wt% of Ge. On further increasing the doping of Ge, the photovoltaic parameters have shown a decreasing trend. The doping of Ge also enhances the stability in air as compared to the nondoped sample.^[304] A recent research on Mn and Ni-doped CsGeI_3 perovskite has revealed the effect of doping of Mn and Ni in CsGeI_3 perovskite that has resulted in enhancement of optical absorption and photoconductivity in visible and UV light region. The optical absorption, dielectric constant, and photoconductivity of Mn-doped CsGeI_3 perovskite are larger than that of Ni-doped counterpart. The Mn-doped $\text{CsGe}_{1-x}\text{Mn}_x\text{Cl}_3$ perovskite exhibited the potential properties that make it best among all the inorganic pure and metal-doped CsGeI_3 perovskite. **Figure 18** shows the light absorption spectrum of pristine and metal-doped (Ni, Mn) CsGeI_3 perovskite as a function of: (a) photon-energy-dependent absorption coefficient, (b) wavelength-dependent absorption coefficient, (c) reflectivity, (d) conductivity, (e) dielectric constant (real part), and (f) dielectric constant (imaginary part).^[305]

In a recent study, lead-free bismuth-based perovskite $\text{CH}_3\text{NH}_3\text{BiX}_3$ ($\text{X}=\text{I}_2\text{Te}, \text{I}_2\text{S}, \text{I}_2\text{Se}$) as a light absorber has been investigated by using first principle calculations. The study has

Table 12. Stability of lead-free perovskites.

Light absorber	SPCE	Stability	Ref.
MASnI ₃ +SnF ₂	2.14%	200 h under 1 sun degradation conditions (AM 1.5, 100 mW cm ⁻²)	[194]
(FA) _{0.75} (MA) _{0.25} SnI ₃	8.12%	≈80% of SPCE over a period of 400 h, stored in a glove box filled with nitrogen	[150]
MASnIBr _{1.8} Cl _{0.2}	3.1%	Average lifetime less than 100 ps	[191]
FASnI ₃ +SnF ₂ pyrazine	4.8%	Stable performances for over 100 d having 98% of its initial efficiency	[195]
FASnI ₃	6.23%	Stable efficiency of 6% for more than 100 s	[172]
en[FASnI ₃]	7.14%	Unencapsulated device continues to have 96% of initial SPCE after 1000 h	[208]
(PEA) ₂ (FA) ₈ SnI ₉ I ₂₈	5.94%	Unencapsulated devices display performance without significant decay in SPCE over 100 h	[156]
FASnI ₃ +EDA1 ₂ (1%)	7.4%	Device stored in glove box displays maximum SPCE of 8.9% for over 1400 h with only slight reduction for storage beyond 2000 h	[203]
FASnI ₃	5.5%	Encapsulated devices exhibit stability over 1000 h under continuous 1 sun illumination encompassing UV region	[167]
CsSnIBr ₂ +HPA	3%	Exhibits stable efficiency for 77 d and power output within 9 h at high temperature up to 473 K	[193]
(PEA) ₂ GeI ₄	–	2D structure is more stable than 3D MAGeI ₃ in air.	[234]
BA ₂ MA _{n-1} MnI _{3n+1}	1.94–2.53%	2D structure is more stable as compared to 3D counterparts.	[235]
MA ₃ Bi ₂ I ₉	0.356%	Exhibits air and moisture stability for more than 60 d	[264]
MA ₃ Bi ₂ I ₉ + NMP	0.31%	Unencapsulated device exhibits 88% of SPCE to relative 50–60% humidity for 30 d	[244]
MA ₃ Bi ₂ I ₉	0.26%	Exhibits stability for more than ten weeks under ambient conditions	[174]
Cs ₃ Bi ₂ I ₉	8%	Unencapsulated device displays initial SPCE for more than 500 h under 1 sun at 65 °C and relative humidity of 60–70%	[141]
MA ₃ Bi ₂ I ₉ (with FPD1 ETM)	0.06%	Exhibits limited degradation in SPCE after 17 d storage in ambient atmosphere	[245]
MA ₃ Bi ₂ I ₉	0.17%	Exhibits 56% of peak SPCE after 300 h exposure to air	[262]
Cs ₂ AgBiBr ₆	2.43%	Unencapsulated device displays excellent stability to working conditions.	[266]
AgBi ₂ I ₇	1.22%	Exhibits excellent stability for at least 10 d under ambient conditions	[265]
Cs ₂ AgBiBr ₆	–	Degrades after light exposure for two weeks	[300]
KBiI ₄ H ₂ O	–	Exhibits considerable stability in air	[252]
Cs ₂ BiAgBr ₆	–	Exhibits stable SPCE in ambient conditions	[254]
Cs ₂ AgBiBr ₆	–	Exhibits degradation after a period of three weeks on exposure to ambient air and light	[256]
MA ₃ Bi ₂ I ₉ via (VASP)	3.17%	Unencapsulated devices display stability for 60 d with 0.1% loss in SPCE	[247]
Cs ₃ Sb ₂ I ₉	<1.00%	Increased stability under ambient air in comparison to MAPbI ₃ films stored in same condition	[140]
MA ₂ AgSbI ₆	–	Exhibits stability at room temperature in air with 20–60% humidity for 370 d	[269]
MA ₃ Bi ₂ I ₉	0.12%	Exhibits no degradation over a month in devices stored in dark in dry air with humidity less than 10%	[111]
Cs ₃ Bi ₂ I ₉	1.09%		
AgBi _x I _{3x+1}	0.60%	Unencapsulated devices exhibited SPCE decreasing at a slow pace, 75% of efficiency even after weeks of storage in a N ₂ filled glove box under ambient light	[186]
1 < x < 2.25 (Ag ₄ Bi ₇ I ₂₅)			
MA ₃ Bi ₂ I ₉	0.19%	Displayed excellent stability for more than 400 d upon contact with 50% humidity and air at room temperature	[127]
MASbSi ₂	3.08%	Unencapsulated devices continues to have 90% of initial SPCE for a period of 15 d when stored in dark with 60% humidity at 25 °C	[271]
(p-F-C ₆ H ₄ -NH ₂) ₂ CuBr ₄ (CH ₃ (CH ₂) ₃ NH ₃) ₂ CuBr ₄	1.74%	Encapsulated device displays stability in air after 1 d in air with 50% of humidity	[135]
	1.76%		
C ₆ H ₄ NH ₂ CuBrI	1.64%	Device exhibited hydrophobic behavior with a contact angle of 90° and unchanged XRD patterns after 4 h of water immersion	[137]
Cs ₂ TiBr ₆	3.3%	Unencapsulated films displayed 94% of SPCE after 14 d at 70 °C, 30% RH and ambient light illumination retained 85% of efficiency	[294]

Table 12. Continued.

Light absorber	SPCE	Stability	Ref.
RbSn _{0.5} Ge _{0.5} I ₃	–	The activation barrier for water penetration is 0.23 eV in a humid environment that is much higher than for MAPbI ₃ (0.09 eV).	[233]
CsGeI ₃	0.11%	Stable up to 350 °C	[144]
MAGeI ₃	0.20%	Stable up to 250 °C	
FAGeI ₃		Stable up to 250 °C	
MASnI ₃	5.8%	Continuous to have 80% of initial SPCE in first 12 h in a properly sealed nitrogen glove box	[106]
MA ₃ Bi ₂ I ₉	0.19%	Films display stability over 40 d on conditional exposure to 50% humidity level at room temperature	[127]
(NH ₄) ₃ Sb ₂ I ₉	0.51%	Films retained 80% of initial SPCE when stored in a glove box with O ₂ < 10 ppm and H ₂ O < 0.1 ppm for 40 d but when in air with 50% humidity, the films lost their PV performance completely	[116]

confirmed that CH₃NH₃BiX₃ (X₃-I₂Te, I₂S, I₂Se) perovskites are nontoxic in nature exhibiting a high optical absorption in the visible region. These properties pave the way for use of such bismuth-based perovskite as a light absorber as an alternative to lead-based CH₃NH₃PbI₃ perovskite in photovoltaic applications.^[306] In another study, lead-free mixed chalcogen halide perovskite material MABiI₂S have been synthesized and characterized for its physical and optical properties that revealed a low bandgap of 1.52 eV suitable for optical absorption in the visible spectrum. The fabricated material exhibited an absorption up to over 1000 nm.^[307] The concentration of perovskite solution (0.15–0.30 M) has an effect on the crystallization in

MA₃Bi₂I₉ films. Also, the speed of rotation during spin-coating process determines the layer coverage. The SPCE of the fabricated cells enhances from 0.004 to 0.17% after processing. The fabricated device has exhibited a V_{OC} of 0.72 V after 48 h.^[308] Lead-free inorganic AgBiI₄ as a light absorber has been prepared by solution method of thin films. The AgBiI₄ films have been fabricated by 0.6 M solution and annealed at 150 °C. The films exhibited a better morphology with a thermal stability and photostability than that of MAPbI₃. The fabricated PSC exhibited 2.1% efficiency. The devices displayed long-term stability and maintained 96% of initial SPCE even after 100 h at relative humidity of 26%.^[309] Lead-free copper halide perovskite Cs₃Cu₂I₅ have

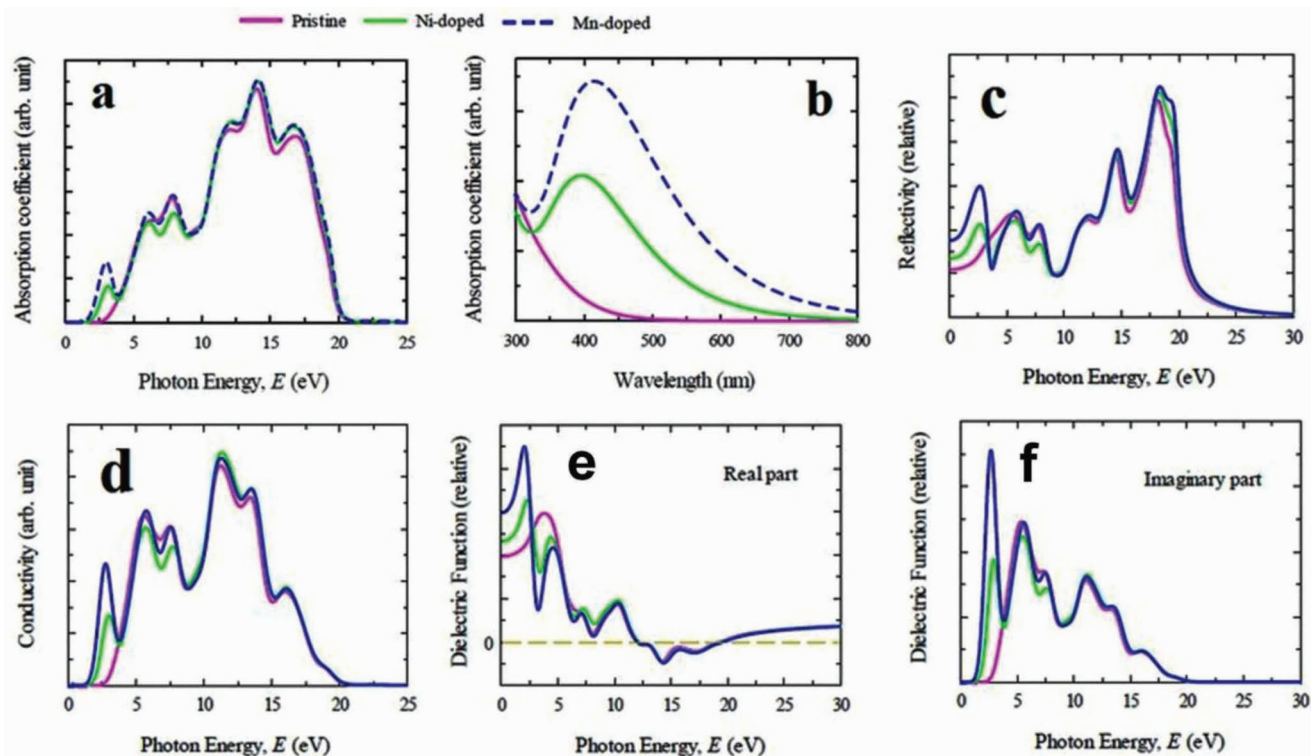


Figure 18. Light absorption spectrum of pristine and metal-doped (Ni, Mn) CsGeI₃ perovskite as a function of a) photon energy dependent absorption coefficient, b) wavelength-dependent absorption coefficient, c) reflectivity, d) conductivity, e) dielectric constant (real part), and f) dielectric constant (imaginary part). Reproduced with permission.^[305] Copyright 2018, Royal Society of Chemistry.

been reported with a 0D structure exhibiting a blue emission (≈ 445 nm) with a high quantum yield of 90 and 60% for single crystals and thin films. The 0D electronic nature of $\text{Cs}_3\text{Cu}_2\text{I}_5$ is attributed to a large exciton binding energy of 49 meV and blue emission is demonstrated using solution method $\text{Cs}_3\text{Cu}_2\text{I}_5$ thin films.^[310] Zinc-based lead-free CsZnCl_2I perovskite 3D thin films have been reported that were deposited at 100 °C by aerosol-assisted chemical vapor deposition method. The fabricated film displayed absorption peaks at 325 nm excitation covering the entire visible spectrum range.^[311] In another study, perovskite solar cells based on transition metal Ti, Ni, and Cd-doped BiFeO_3 as a light absorber with graphene electrode have been investigated. The V_{OC} of pure BiFeO_3 , Ti, Ni, Cd-doped BiFeO_3 have been reported to be 0.49, 0.77, 0.56, and 0.49 V, respectively. A study of formation of thin films of pure and doped perovskites through three different processes—spinning, dipping, and spray process—has been carried out that revealed that Ti-based BiFeO_3 in spinning process have given the best results.^[312] Lead-free Ti-based perovskites have been investigated for their photovoltaic behavior.^[313] Transition metal palladium-based lead-free perovskite Cs_2PdBr_6 nanocrystals have been reported with an average particle diameter of 2.8 nm and a thickness of 1–2 units cells exhibiting a narrow bandgap of 1.69 eV and outstanding stability toward light humidity and heat. The fast anion exchange method has been employed to synthesize Cs_2PdI_6 nanocrystals.^[314]

Lead-free $(1-x)$ $(\text{K}_{0.44}\text{Na}_{0.52}\text{Li}_{0.04})(\text{Nb}_{0.91}\text{Ti}_{0.05}\text{Sb}_{0.04})\text{O}_3-x\text{SmAlO}_3$ [$x = 0, 0.001, 0.004, 0.004, 0.008$] ceramics have been synthesized by a solid-state sintering method. The effect of doping of SmAlO_3 on the phase structure and electrical properties of all the perovskite composition for reported values of x have been investigated thoroughly. From the study of XRD analysis, all the investigated composition reported a perovskite structure at the suitable sintering temperature. The enhanced electrical properties were obtained at the sintering temperature of 1180 °C.^[315] Lead-free multiferroic $(1-x)$ $\text{KNbO}_3-(x)\text{CoFe}_2\text{O}_4$ composites have been synthesized by employing solid-state reaction method with x (0, 0.25, 0.5, 0.75, 1.0) mol. The careful study of XRD reveals that KNbO_3 perovskite belong to an orthorhombic system, spinal CoFe_2O_4 belong to cubic system, and other compositions of x belong to mixed phase of KNbO_3 and CoFe_2O_4 . The high-resolution SEM analysis has shown that the morphology of KNbO_3 and CoFe_2O_4 was modified by CoFe_2O_4 content. The composite 0.5KNbO_3 0.5 CoFe_2O_4 displayed a high value of coercivity and 0.5KNbO_3 $0.5\text{CoFe}_2\text{O}_4$ and 0.75KNbO_3 0.75 CoFe_2O_4 displayed an enhanced value of dielectric constant.^[316] At present, a lot of research is going on lead-free double perovskite materials to explore their potential as a light absorber in perovskite solar device. Double perovskite $\text{A}_2\text{B}'\text{B}''\text{X}_6[\text{A-Cs, MA, B}'\text{-Bi, Sb, B}''\text{-Cu, Ag, X-Cl, Br, I}]$ have been investigated for their structural, optical, and stability properties.^[317] The vapor-assisted method has been employed to synthesize double perovskite $\text{Cs}_2\text{AgBiB}_6$ thin films with better morphology. The better quality of $\text{Cs}_2\text{AgBiB}_6$ films has a photoluminescence lifetime of 117 ns. The fabricated n-i-p perovskite solar cell has reported a SPCE of 1.37% with a better stability of 90% after 240 h of storage under ambient conditions.^[318] The diffusion of X halide anion in lead-free double perovskite $\text{Cs}_2\text{AgBiX}_6$ [X-Cl, Br], $\text{Cs}_2\text{AgSbCl}_6$, $\text{Cs}_2\text{AgInCl}_6$ has been investigated by using first principle calculations. The calculated values of formation energy of X-site

vacancies are related to electronic configuration of B-site cations. The double perovskite $\text{Cs}_2\text{AgInCl}_6$ is having lowest vacancy formation energy due to unfilled s-orbital of In^{3+} . The hysteresis loss in $\text{Cs}_2\text{AgBiBr}_6$ solar cells is attributed to the lowest energy barrier for X-site migration.^[319] Double perovskite lead-free layered $\text{Cs}_4\text{CuSb}_2\text{Cl}_{12}$ have been reported with a bandgap of 1 eV prepared by grinding of precursor salts at ambient conditions. A long range magnetic ordering is displayed by the synthesized perovskite at room temperature that plays a pivotal role in controlling the electronic properties of double perovskite $\text{Cs}_4\text{CuSb}_2\text{Cl}_{16}$.^[320] By using first principle calculations, lead-free double perovskite $\text{Cs}_2\text{NaBX}_6[\text{B-Sb, Bi, X-Cl, Br, I}]$ have been synthesized and characterized for their electronic and optical properties. The simple solution method has been employed to prepare a layered $\text{MA}_3\text{Bi}_2\text{I}_9$ perovskite and a composite layer of bismuth tri iodide (BiI_3). By employing SEM and XRD techniques, the morphology of the active layer has been investigated that has a direct influence on performance of the perovskite device.^[321] The high-temperature solid-state reaction method has been employed to prepare polycrystalline material of double perovskite $\text{Dy}_2\text{NiMnO}_6$ with a monoclinic structure. The high-temperature condition of the material is attributed to the presence of oxygen vacancies making it viable to use at different temperatures.^[322]

9. Conclusion

The research in tin-based perovskites MASnX_3 has revealed a direct bandgap of 1.20–1.35 eV, electron mobility of $2320 \text{ cm}^2 \text{ V}^{-1} \text{ s}^{-1}$, hole carrier mobility of $322 \text{ cm}^2 \text{ V}^{-1} \text{ s}^{-1}$, and long charge carrier diffusion length of more than 500 nm. The alteration of Br^-/I^- ratio in $\text{MASnI}_{3-x}\text{Br}_x$ has resulted in large value of V_{OC} (0.88 V) in MASnBr_3 and J_{SC} (12.33 mA cm^{-2}) in MASnIBr_2 . The absorption band can be tuned by altering the composition of halide anions in MASnX_3 perovskites. However, Sn-based perovskites suffer from degradation in air due to oxidation of Sn^{2+} into Sn^{4+} . The incorporation of additives has resulted in reduced oxidation and better stability in air. The A-site cation has a significant effect on photovoltaic performance. The use of diethylammonium (en) and FA^+ at the A-site of ASnX_3 has resulted in wider bandgaps and improved stability. An efficiency of 8% has been achieved for $(\text{FA})_{0.75}(\text{MA})_{0.25}\text{SnI}_3$ with a V_{OC} (0.61 V) and bandgap (1.33 eV). Germanium-based perovskites do have an optical bandgap of 1.63 eV, excellent hole and electron conducting behavior, and better stability in air. Using DFT calculations, it has been reported that with increase of size of halide anion, the bandgaps have decreasing values of 3.7, 2.81, and 1.61 eV, respectively. The replacement of the iodide content in AGeI_3 by bromide results in enhanced photovoltaic performance and stability to a slight extent. Mixed Ge-based perovskite $\text{RbSn}_{0.5}\text{Ge}_{0.5}\text{I}_3$ exhibits a better optical absorption and effective masses for higher carrier mobility and good stability in water. By engineering the size of A-site cation, its doping with another suitable cation and size of halide anion, it is possible to fabricate a Ge-based perovskite as an efficient light absorber. Although, bismuth-based perovskite $(\text{MA})_3\text{Bi}_2\text{I}_9$ has displayed low values of solar power conversion efficiencies up to 1.64 eV up to now, yet they have exhibited excellent stability in ambient air at room temperature and against exposure to humidity. The morphology of $(\text{MA})_3\text{Bi}_2\text{I}_9$ films can

be enhanced by addition of various concentration of NMP into the precursor solution that not only controlled the rate of crystallization but also enhanced the efficiency and stability in a relative humidity of 50–60%. The concentration of perovskite solution and substrate temperature also impacts its efficiency and stability. The wide bandgaps of lead-free perovskites can be engineered to a narrow bandgap by incorporating triiodide into P(4-methyl piperidinium)₃Bi₂I₉(MP-Bi₂I₉) that exhibited a bandgap of 1.58 eV in comparison to 1.5 eV of MAPbI₃. The various deposition methods have a direct influence on morphology of films. Cs₃Bi₂I₉ has displayed an efficiency of 8% with a pure crystalline phase and stability. Bismuth-based double perovskite like Cs₂AgBiBr₆ exhibited an indirect bandgap of 2.19 eV. The DFT calculations have further revealed that the family of 3D double perovskites have optical bandgap in the visible range and low carrier effective masses. Bismuth-based perovskites can be thoroughly investigated for enhancement in their efficiency as these materials have excellent stability in ambient air and in relative humidity. In antimony-based perovskites, the size of cationic or anionic species and the employed processing technique determine the structure. When A-site cation Cs⁺ is replaced by a smaller cation Rb⁺, a 2D layered phase is achieved with a formation energy difference of 0.25 eV in comparison to Cs-based counterparts. The addition of additive in 0D (MA)₃Sb₂I₉ films has resulted in enhanced light absorption in the visible wavelength regions up to 400 nm. The use of chalcogenide and mixed perovskite materials can be an effective strategy for formation of efficient, cheap, and stable solar cells. Cs₄CuSb₂Cl₁₂, besides having photo and thermal stability and resistance to humidity, have exhibited excellent photovoltaic properties. There has been a significant effect on photovoltaic parameters on substitution of Sb with Bi in 2D mixed layered perovskites (NH₄)₃(Sb_{1-x}Bi_x)₂I₉. By proper substitution of Bi into antimony-based perovskites, it is possible to fabricate light harvesters with high efficiency and stability. Copper-based perovskites usually form 2D layered structure owing to their smaller ionic radii. By proper tuning of Cl⁻/Br⁻ ratio, the optical absorption of Cu-based perovskites can be extended in the near-infrared region. The (MA)₂CuCl₂Br₂ and (MA)₂CuCl_{0.5}Br_{3.5} have reported better stability under ambient conditions. The divalent cations of alkaline earth metals like Mg²⁺, Ca²⁺, and Sr²⁺ can be effective replacement for lead. The perovskite solar cells based on transition metals Ti, Ni, and Cd-doped BiFeO₃ as a light absorber have displayed V_{OC} values of 0.77, 0.56, and 0.49 V, respectively. By suitable selection of A and B-site cations and halide anions, their alteration in composition and synthesis method, it is possible to fabricate lead-free perovskites with maximum efficiency and stability without any toxic influence on environment.

Conflict of Interest

The authors declare no conflict of interest.

Keywords

lead-free perovskites, photovoltaic parameters, stability

Received: May 29, 2019
Published online: July 22, 2019

- [1] H. Tanaka, M. Misono, *Curr. Opin. Solid State Mater. Sci.* **2001**, 5, 381.
- [2] Z. Yi, N. H. Ladi, X. Shai, H. Li, Y. Shen, M. Wang, *Nanoscale Adv.* **2019**, 1, 1276.
- [3] T. He, Q. Huang, A. Ramirez, Y. Wang, K. Regan, N. Rogado, M. A. Hayward, M. K. Haas, J. S. Slusky, K. Inumara, H. W. Zandbergen, N. P. Ong, R. J. Cava, *Nature* **2001**, 411, 54.
- [4] V. M. Goldschmidt, *Die Naturwiss.* **1926**, 14, 477.
- [5] X. Liu, R. Hong, C. Tian, *J. Mater. Sci.: Mater. Electron.* **2009**, 20, 323.
- [6] H. Kronmuller, S. Parkin, *Handbook of Magnetism and Advanced Magnetic Materials*, Wiley, Hoboken, NJ **2007**.
- [7] R. H. Buttner, E. N. Maslen, *Acta Crystallogr., Sect. B: Struct. Sci.* **1992**, 48, 764.
- [8] P. Szuromi, B. Grocholski, *Science* **2017**, 358, 732.
- [9] B. Saparov, D. B. Mitzi, *Chem. Rev.* **2016**, 116, 4558.
- [10] G. Kieslich, S. Sun, A. K. Cheetham, *Chem. Sci.* **2014**, 5, 4712.
- [11] G. Kieslich, S. Sun, A. K. Cheetham, *Chem. Sci.* **2015**, 6, 3430.
- [12] R. D. Shannon, *Acta Crystallogr., Sect. A: Found. Adv.* **1976**, 32, 751.
- [13] Q. Chen, N. De Marco, Y. Wang, Y. Song, C. C. Chen, H. Zhao, Z. Hong, H. Zhou, Y. Yang, *Nano Today* **2015**, 10, 355.
- [14] Z. Li, M. Yang, J. S. Park, S. H. Wei, J. J. Berry, K. Zhu, *Chem. Mater.* **2016**, 28, 284.
- [15] Q. Wang, N. Phung, D. D. Girolamo, P. Vivoc, A. Abate, *Energy Environ. Sci.* **2019**, 12, 865.
- [16] J. W. Lee, D. H. Kim, H. S. Kim, S. W. Seo, S. M. Cho, N. G. Park, *Adv. Energy Mater.* **2015**, 5, 1501310.
- [17] D. P. McMeekin, G. Sadoughi, W. Rehman, G. E. Eperon, M. Saliba, M. T. Hörlantner, A. Haghighirad, N. Sakai, L. Korte, B. Rech, M. B. Johnston, L. M. Herz, H. J. Snaith, *Science* **2016**, 351, 151.
- [18] S. Shah, Thin Film Share to Decline to 7% in 2015—The Lowest so Far!, <http://www.greenworldinvestor.com/2015/03/24/thin-film-share-to-decline-to-7-in-2015-the-lowest-so-far/> (accessed: June 2017).
- [19] S. Rühle, *Sol. Energy* **2016**, 130, 139.
- [20] K. Bullis, *Record-Breaking Solar Cell Points the Way to Cheaper Power*, MIT Technology Review, **2014**.
- [21] F. Dimroth, T. N. D. Tibbits, M. Niemeyer, F. Predan, P. Beutel, C. Karcher, E. Oliva, G. Siefert, D. Lackner, P. Fuß-Kailuweit, A. W. Bett, R. Krause, C. Dräke, E. Guio, J. Wassel, A. Tauzin, T. Signamarche, *IEEE J. Photovoltaics* **2016**, 6, 343.
- [22] L. Zyg, "Solar cell sets world record with a stabilized efficiency of 13.6%," <https://Phys.org> (accessed: June 2015).
- [23] S. Essig, C. Allebe, T. Remo, J. F. Geisz, M. A. Steiner, K. Horowitz, L. Barraud, J. S. Ward, M. Schnabel, *Nat. Energy* **2017**, 2, 17144.
- [24] M. A. Green, K. Emery, Y. Hishikawa, W. Warta, E. D. Dunlop, *Prog. Photovoltaics* **2013**, 21, 1.
- [25] B. Parida, S. Iniyar, R. Goic, *Renewable Sustainable Energy Rev.* **2011**, 15, 1625.
- [26] S. Mathew, A. Yella, P. Gao, R. Humphry-Baker, B. F. E. Curchod, N. Ashari-Astani, I. Tavernelli, U. Rothlisberger, M. K. Nazeeruddin, M. Grätzel, *Nat. Chem.* **2014**, 6, 242.
- [27] Perovskite Offers Shot at Cheaper Solar Energy, <http://www.wsj.com/articles/perovskite-offers-shot-at-cheaper-solar-energy-1411937799> (accessed: May 2015).
- [28] A. Kojima, K. Teshima, Y. Shirai, T. Miyasaka, *J. Am. Chem. Soc.* **2009**, 131, 6050.
- [29] D. A. Egger, E. Edri, D. Cahen, G. Hodes, *J. Phys. Chem. Lett.* **2015**, 6, 279.
- [30] M. Zhang, M. Lyu, H. Yu, J. H. Yun, Q. Wang, L. Wang, *Chem. - Eur. J.* **2015**, 21, 434.
- [31] H. Shen, T. Duong, Y. Wu, J. Peng, D. Jacobs, N. Wu, K. Weber, T. White, K. Catchpole, *Sci. Technol. Adv. Mater.* **2018**, 19, 53.

- [32] M. Liu, M. B. Johnston, H. J. Snaith, *Nature* **2013**, *501*, 395.
- [33] H. Zhou, Q. Chen, G. Li, S. Luo, T. Song, H. S. Duan, Z. Hong, J. You, Y. Liu, Y. Yang, *Science* **2014**, *345*, 542.
- [34] N. J. Jeon, H. G. Lee, Y. C. Kim, J. Seo, J. H. Noh, J. Lee, S. Seok, *J. Am. Chem. Soc.* **2014**, *136*, 7837.
- [35] J. H. Heo, D. H. Song, H. J. Han, S. Y. Kim, J. H. Kim, D. Kim, H. W. Shin, T. K. Ahn, C. Wolf, T. W. Lee, S. H. Im, *Adv. Mater.* **2015**, *27*, 3424.
- [36] M. A. Green, T. Bein, *Nat. Mater.* **2015**, *14*, 559.
- [37] S. D. Stranks, H. J. Snaith, *Nat. Nanotechnol.* **2015**, *10*, 391.
- [38] M. A. Green, A. H. Ho-Baillie, H. J. Snaith, *Nat. Photonics* **2014**, *8*, 506.
- [39] S. D. Stranks, G. E. Eperon, G. Grancini, C. Menelaou, Marcelo, J. P. Alcocer, T. Leijtens, L. M. Herz, A. Petrozza, H. J. Snaith, *Science* **2013**, *342*, 341.
- [40] K. Song, Y. Wu, X. Chen, Y. He, L. Liu, G. Chen, R. Liu, *AIP Adv.* **2018**, *8*, 035114.
- [41] H. S. Kim, C. R. Lee, J. H. Im, K. B. Lee, T. Moehl, A. Marchioro, S. J. Moon, R. H. Baker, J. H. Yum, J. E. Moser, M. Grätzel, N. G. Park, *Sci. Rep.* **2012**, *2*, 591.
- [42] J. H. Noh, S. H. Im, J. H. Heo, T. N. Mandal, S. I. Seok, *Nano Lett.* **2013**, *13*, 1764.
- [43] J. M. Ball, M. M. Lee, A. Hey, H. J. Snaith, *Energy Environ. Sci.* **2013**, *6*, 1739.
- [44] J. Burschka, N. Pellet, S.-J. Moon, R. Humphry-Baker, P. Gao, M. K. Nazeeruddin, M. Grätzel, *Nature* **2013**, *499*, 316.
- [45] A. Abrusci, S. D. Stranks, P. Docampo, H.-L. Yip, A. K.-Y. Jen, H. J. Snaith, *Nano Lett.* **2013**, *13*, 3124.
- [46] A. Kojima, K. Teshima, Y. Shirai, T. Miyasaka, presented at *210th ECS Meeting Abstract*, **2006**.
- [47] A. Kojima, K. Teshima, Y. Shirai, T. Miyasaka, presented at *210th ECS Meeting Abstract*, **2008**.
- [48] J. H. Im, C. R. Lee, J. W. Lee, S. W. Park, N. G. Park, *Nanoscale* **2011**, *3*, 4088.
- [49] U. Bach, D. Lupo, P. Comte, J. E. Moser, F. Weissortel, J. Salbeck, H. Spreitzer, M. Grätzel, *Nature* **1998**, *395*, 583.
- [50] J. Burschka, A. Dualeh, F. Kessler, E. Baranoff, N. L. Cevy-Ha, C. Y. Yi, M. K. Nazeeruddin, M. Grätzel, *J. Am. Chem. Soc.* **2011**, *133*, 18042.
- [51] M. M. Lee, J. Teuscher, T. Miyasaka, T. N. Murakami, H. J. Snaith, *Science* **2012**, *338*, 643.
- [52] J. Burschka, N. Pellet, S. J. Moon, R. H. Baker, P. Gao, M. K. Nazeeruddin, M. Grätzel, *Nature* **2013**, *499*, 316.
- [53] X. Liu, C. C. Chueh, Z. Zhu, S. B. Jo, Y. San, A. K. Y. Jen, *J. Mater. Chem. A* **2016**, *4*, 15294.
- [54] J. You, L. Meng, T.-B. Song, T.-F. Guo, Y. (Michael) Yang, W.-H. Chang, Z. Hong, H. Chen, H. Zhou, Q. Chen, Y. Liu, N. De Marco, Y. Yang, *Nat. Nanotechnol.* **2016**, *11*, 75.
- [55] W. S. Yang, B. W. Park, E. H. Jung, N. J. Jeon, Y. C. Kim, D. U. Lee, S. S. Shin, J. Seo, E. K. Kim, J. H. Noh, S. I. Seok, *Science* **2017**, *356*, 1376.
- [56] X. Dong, X. Fang, M. Lv, B. Lin, S. Zhang, J. Ding, N. Yuan, *J. Mater. Chem. A* **2015**, *3*, 5360.
- [57] Y. Han, S. Meyer, Y. Dkhissi, K. Weber, J. M. Pringle, U. Bach, L. Spiccia, Y. B. Cheng, *J. Mater. Chem. A* **2015**, *3*, 8139.
- [58] J. Yang, B. D. Siempelkamp, D. Liu, T. L. Kelly, *ACS Nano* **2015**, *9*, 1955.
- [59] T. Leijtens, G. E. Eperon, S. Pathak, A. Abate, M. M. Lee, H. J. Snaith, *Nat. Commun.* **2013**, *4*, 2885.
- [60] L. K. Ono, S. R. Raga, S. Wang, Y. Kato, Y. Qi, *J. Mater. Chem. A* **2015**, *3*, 9074.
- [61] S. N. Habisreutinger, T. Leijtens, G. E. Eperon, S. D. Stranks, R. J. Nicholas, H. J. Snaith, *Nano Lett.* **2014**, *14*, 5561.
- [62] H. J. Snaith, A. Abate, J. M. Ball, G. E. Eperon, T. Leijtens, N. K. Noel, S. D. Stranks, J. T. Wang, K. Wojciechowski, W. J. Zhang, *J. Phys. Chem. Lett.* **2014**, *5*, 1511.
- [63] N. G. Park, M. Grätzel, T. Miyasaka, K. Zhu, K. Emery, *Nat. Energy* **2016**, *1*, 16152.
- [64] Y. Yuan, J. Huang, *Acc. Chem. Res.* **2016**, *49*, 286.
- [65] J. Liu, N. Li, J. Jia, J. Dong, Z. Qiu, S. Iqbal, B. Cao, *Sol. Energy* **2019**, *181*, 285.
- [66] P. Da, G. Zheng, *Nano Res.* **2017**, *10*, 1471.
- [67] J. Y. Jeng, Y. F. Chiang, M. H. Lee, S. R. Peng, T. F. Guo, P. Chen, T. C. Wen, *Adv. Mater.* **2013**, *25*, 3727.
- [68] H. Peng, W. Sun, Y. Li, S. Ye, H. Rau, W. Yan, H. Zhou, Z. Bian, C. Huang, *Nano Res.* **2016**, *9*, 2960.
- [69] Y. Bai, S. Meng, S. Yang, *Adv. Energy Mater.* **2018**, *8*, 1701883.
- [70] T. Liu, K. Chen, Q. Hu, R. Zhu, Q. Gong, *Adv. Energy Mater.* **2016**, *6*, 1600457.
- [71] T. S. Atabaev, *Mater. Today: Proc.* **2017**, *4*, 4919.
- [72] Y. Liu, S. Ji, S. Li, W. He, K. Wang, H. Hu, C. Ye, *J. Mater. Chem. A* **2015**, *3*, 14902.
- [73] N. J. Jeon, J. H. Noh, W. S. Yang, Y. C. Kim, S. Ryu, J. Seo, S. I. Seok, *Nature* **2015**, *517*, 476.
- [74] W. S. Yang, J. H. Noh, N. J. Jeon, Y. C. Kim, S. Ryu, J. Seo, S. Seok, *Science* **2015**, *348*, 1234.
- [75] D. Bi, W. Tress, M. I. Dar, P. Gao, J. Luo, C. Renevier, K. Schenk, A. Abate, F. Giordano, J.-P. C. Baena, J.-D. Decoppet, S. M. Zakeeruddin, M. K. Nazeeruddin, M. Grätzel, A. Hagfeldt, *Sci. Adv.* **2016**, *2*, e1501170.
- [76] H. J. Snaith, *J. Phys. Chem. Lett.* **2013**, *4*, 3623.
- [77] C. Wehrenfennig, G. E. Eperon, M. B. Johnston, H. J. Snaith, L. M. Herz, *Adv. Mater.* **2014**, *26*, 1584.
- [78] G. E. Eperon, S. D. Stranks, C. Menelaou, M. B. Johnston, L. M. Herz, H. J. Snaith, *Energy Environ. Sci.* **2014**, *7*, 982.
- [79] A. Sadhanala, F. Deschler, T. H. Thomas, S. E. Dutton, K. C. Goedel, F. C. Hanusch, M. L. Lai, U. Steiner, T. Bein, P. Docampo, D. Cahen, R. H. Friend, *J. Phys. Chem. Lett.* **2014**, *5*, 2501.
- [80] A. Sadhanala, A. Kumar, S. Pathak, A. Rao, U. Steiner, N. C. Greenham, H. J. Snaith, R. H. Friend, *Adv. Electron. Mater.* **2015**, *1*, 1500008.
- [81] S. De Wolf, J. Holovsky, S. J. Moon, P. Loper, B. Niesen, M. Ledinsky, F. J. Haug, J. H. Yum, C. Ballif, *J. Phys. Chem. Lett.* **2014**, *5*, 1035.
- [82] F. Giustino, H. J. Snaith, *ACS Energy Lett.* **2016**, *1*, 1233.
- [83] G. Xing, N. Mathews, S. Sun, S. S. Lim, Y. M. Lam, M. Grätzel, S. Mhaisalkar, T. C. Sum, *Science* **2013**, *342*, 344.
- [84] Q. Dong, Y. Fang, Y. Shao, P. Mulligan, J. Qiu, L. Cao, J. Huang, *Science* **2015**, *347*, 967.
- [85] A. Miyata, A. Mitioglu, P. Plochocka, O. Portugall, J. T. W. Wang, S. D. Stranks, H. J. Snaith, R. J. Nicholas, *Nat. Phys.* **2015**, *11*, 582.
- [86] C. C. Stoumpos, C. D. Malliakas, M. G. Kanatzidis, *Inorg. Chem.* **2013**, *52*, 9019.
- [87] P. V. Kamat, J. Bisquert, J. Buriak, *ACS Energy Lett.* **2017**, *2*, 904.
- [88] A. Wang, X. Yan, M. Zhang, S. Sun, M. Yang, W. Shen, X. Pan, P. Wang, Z. Deng, *Chem. Mater.* **2016**, *28*, 8132.
- [89] D. W. de Quilletes, S. M. Vorpahl, S. D. Stranks, H. Nagaoka, G. E. Eperon, M. E. Ziffer, H. J. Snaith, D. S. Ginger, *Science* **2015**, *348*, 683.
- [90] M. R. Filip, G. E. Eperon, H. J. Snaith, F. Giustino, *Nat. Commun.* **2014**, *5*, 5757.
- [91] L. M. P. Pazos-Outon, M. Szumilo, R. Lamboll, J. M. Richter, M. Crespo-Quesada, M. Abdi-Jalebi, H. J. Beeson, M. Vrućinić, M. Alsari, H. J. Snaith, B. Ehrler, R. H. Friend, F. Deschler, *Science* **2016**, *351*, 1430.
- [92] World Health Organisation, Exposure to Lead: A Major Public Health Concern, 2010, <http://www.who.int/ipcs/features/lead.pdf> (accessed: July 2017).
- [93] World Health Organisation, International Program on Chemical Safety: Ten Chemicals of Major Public Health Concern,

- 2010, http://www.who.int/ipcs/assessment/public_health/chemicals_phc/en/.
- [94] H. Needleman, *Annu. Rev. Med.* **2004**, *55*, 209.
- [95] A. Babayigit, A. Ethirajan, M. Muller, B. Conings, *Nat. Mater.* **2016**, *15*, 247.
- [96] G. F. Nordberg, B. A. Fowler, M. Nordberg, *Handbook on the Toxicology of Metals*, Elsevier, Amsterdam **2015**.
- [97] L. Patrick, *Med. Rev.* **2006**, *11*, 2.
- [98] T. A. Berhe, W. N. Su, C. H. Chen, C. J. Pan, J. H. Cheng, H. M. Chen, M. C. Tsai, L. Y. Chen, A. A. Dubale, B. J. Hwang, *Energy Environ. Sci.* **2016**, *9*, 323.
- [99] T. Leijtens, G. E. Eperon, N. K. Noel, S. N. Habisreutinger, A. Petrozza, H. J. Snaith, *Adv. Energy Mater.* **2015**, *5*, 1500963.
- [100] F. U. Kosasih, C. Ducati, *Nano Energy* **2018**, *47*, 243.
- [101] B. Hailegnaw, S. Kirmayer, E. Edri, G. Hodes, D. Cahen, *J. Phys. Chem. Lett.* **2015**, *6*, 1543.
- [102] S. Gupta, T. Bendikov, G. Hodes, D. Cahen, *ACS Energy Lett.* **2016**, *1*, 1028.
- [103] W. E. Sha, X. Ren, L. Chen, W. C. Choy, *Appl. Phys. Lett.* **2015**, *106*, 221104.
- [104] J. Bisquert, *J. Phys. Chem. Lett.* **2013**, *4*, 2597.
- [105] S. Tsarev, A. G. Boldyreva, S. Yu. Luchkin, M. Elshobaki, M. I. Afanasov, K. J. Stevenson, P. A. Troshinab, *J. Mater. Chem. A* **2018**, *6*, 21389.
- [106] F. Hao, C. C. Stoumpos, D. H. Cao, R. P. H. Chang, M. G. Kanatzidis, *Nat. Photonics* **2014**, *8*, 489.
- [107] Y. Takahashi, H. Hasegawa, Y. Takahashi, T. Inabe, *J. Solid State Chem.* **2013**, *205*, 39.
- [108] L. M. Herz, *ACS Energy Lett.* **2017**, *2*, 1539.
- [109] T. M. Koh, T. Krishnamoorthy, N. Yantara, C. Shi, W. L. Leong, P. P. Boix, A. C. Grimsdale, S. G. Mhaisalkar, N. Mathews, *J. Mater. Chem. A* **2015**, *3*, 14996.
- [110] K. Shum, Z. Chen, J. Qureshi, C. Yu, J. J. Wang, W. Pfenninger, N. Vockic, J. Midgley, J. T. Kenney, *Appl. Phys. Lett.* **2010**, *96*, 221903.
- [111] B. W. Park, B. Phitippe, S. Zhang, H. Rensmo, G. Boschiloo, E. M. J. Johansson, *Adv. Mater.* **2015**, *27*, 6806.
- [112] B. Ghosh, B. Wu, H. K. Mulmudi, C. Guet, K. Weber, T. C. Sum, S. Mhaisalkar, N. Mathews, *ACS Appl. Mater. Interfaces* **2018**, *10*, 35000.
- [113] Y. Q. Zhao, X. Wang, B. Liu, Z.-L. Yu, P.-B. He, Q. Wan, M. Q. Cai, H. L. Yu, *Org. Electron.* **2018**, *53*, 50.
- [114] M. I. Saidaminov, A. L. Abdelhady, B. Murali, E. Alarousu, V. M. Burlakov, W. Peng, I. Dursun, L. Wang, Y. He, G. Maculan, A. Goriely, T. Wu, O. F. Mohammed, O. M. Bakr, *Nat. Commun.* **2015**, *6*, 7586.
- [115] Z. Xiao, Y. Zhou, H. Hosono, T. Kamiya, *Phys. Chem. Chem. Phys.* **2015**, *17*, 18900.
- [116] C. Zuo, L. Ding, *Angew. Chem.* **2017**, *129*, 6628.
- [117] L. Ma, F. Hao, C. C. Stoumpos, B. T. Phelan, M. R. Wasielewski, M. G. Kanatzidis, *J. Am. Chem. Soc.* **2016**, *138*, 14750.
- [118] B. Wu, Y. Zhou, G. Xing, Q. Xu, H. F. Garces, A. Solanki, T. W. Goh, N. P. Padture, T. C. Sum, *Adv. Funct. Mater.* **2017**, *27*, 1604818.
- [119] Z. Chen, C. Yu, K. Shum, J. J. Wang, W. Pfenninger, N. Vockic, J. Midgley, J. T. Kenney, *J. Lumin.* **2012**, *132*, 345.
- [120] N. K. Noel, S. D. Stranks, A. Abate, C. Wehrenfennig, S. Guarnera, A.-A. Haghighirad, A. Sadhanala, G. E. Eperon, S. K. Pathak, M. B. Johnston, A. Petrozza, L. M. Herz, H. J. Snaith, *Energy Environ. Sci.* **2014**, *7*, 3061.
- [121] D. B. Mitzi, C. A. Feild, Z. Schlesinger, R. B. Laibowitz, *J. Solid State Chem.* **1995**, *114*, 159.
- [122] R. L. Milot, G. E. Eperon, T. Green, H. J. Snaith, M. B. Johnston, L. M. Herz, *J. Phys. Chem. Lett.* **2016**, *7*, 4178.
- [123] I. Chung, J. H. Song, J. Im, J. Androulakis, C. D. Malliakas, H. Li, A. J. Freeman, J. T. Kenney, M. G. Kanatzidis, *J. Am. Chem. Soc.* **2012**, *134*, 8579.
- [124] C. R. Kagan, D. B. Mitzi, C. D. Dimitrakopoulos, *Science* **1999**, *286*, 945.
- [125] T. Matsushima, S. Hwang, A. S. D. Sandanayaka, C. Qin, S. Terakawa, T. Fujihara, M. Yahiro, C. Adachi, *Adv. Mater.* **2016**, *28*, 10275.
- [126] A. Bhatia¹, G. Hautier, T. Nilgiansku, A. Miglio, G. M. Rignanese, X. Gonze, J. Suntivich, *Chem. Mater.* **2016**, *28*, 30.
- [127] M. Lyu, J.-H. Yun, M. Cai, Y. Jiao, P. V. Bernhardt, M. Zhang, Q. Wang, A. Du, H. Wang, G. Liu, L. Wang, *Nano Res.* **2016**, *9*, 692.
- [128] M. Abulikemu, S. O. Chikh, X. Miao, E. Alarousu, B. Murali, G. O. N. Ndjawa, J. Barbé, A. El Labban, A. Amassian, S. D. Gobbo, *J. Mater. Chem. A* **2016**, *4*, 12504.
- [129] F. Funabiki, Y. Toda, H. Hosono, *J. Phys. Chem. C* **2018**, *122*, 10749.
- [130] R. S. Sanchez, E. Mas-Marza, *Sol. Energy Mater. Sol. Cells* **2016**, *158*, 189.
- [131] M. Chen, M.-G. Ju, H. F. Garces, A. D. Carl, L. K. Ono, Z. Hawash, Y. Zhang, T. Shen, Y. Qi, R. L. Grimm, D. Pacifici, X. C. Zeng, Y. Zhou, N. P. Padture, *Nat. Commun.* **2019**, *10*, 16.
- [132] A. Abate, D. J. Hollman, J. Teuscher, S. Pathak, R. Avolio, G. D. Errico, G. Vitiello, S. Fantacci, H. J. Snaith, *J. Am. Chem. Soc.* **2013**, *135*, 13538.
- [133] X. Zhao, M. Wang, *Mater. Today Energy* **2018**, *7*, 208.
- [134] U. B. Cappel, T. Daeneke, U. Bach, *Nano Lett.* **2012**, *12*, 4925.
- [135] X. P. Cui, K. J. Jiang, J. H. Huang, Q. Q. Zhang, M. J. Su, L. M. Yang, Y. L. Song, X. Q. Zhou, *Synth. Met.* **2015**, *209*, 247.
- [136] D. Cortecchia, H. A. Dewi, J. Yin, A. Bruno, S. Chen, T. Baikie, P. P. Boix, M. Gratzel, S. Mhaisalkar, C. Soci, N. Mathews, *Inorg. Chem.* **2016**, *55*, 1044.
- [137] X. Li, X. Zhong, Y. Hu, B. Li, Y. Sheng, Y. Zhang, C. Weng, M. Feng, H. Han, J. Wang, *J. Phys. Chem. Lett.* **2017**, *8*, 1804.
- [138] D. Zhao, M. Sexton, H.-Y. Park, G. Baure, J. C. Nino, F. So, *Adv. Energy Mater.* **2015**, *5*, 1401855.
- [139] S. Ryu, J. H. Noh, N. J. Jeon, Y. C. Kim, W. S. Yang, J. Seo, S. I. Seok, *Energy Environ. Sci.* **2014**, *7*, 2614.
- [140] B. Saparov, F. Hong, J. P. Sun, H. S. Duan, W. Meng, S. Cameron, I. G. Hill, Y. Yan, D. B. Mitzi, *Chem. Mater.* **2015**, *27*, 5622.
- [141] J. H. Heo, M. H. Lee, D. H. Song, C. E. Song, J. J. Lee, K. H. Hong, S. H. Im, *Nanosci. Nanotechnol. Lett.* **2018**, *10*, 591.
- [142] W. Ke, C. C. Stoumpos, I. Spanopoulos, L. Mao, M. Chen, M. R. Wasielewski, M. G. Kanatzidis, *J. Am. Chem. Soc.* **2017**, *139*, 14800.
- [143] S. Oz, J.-C. Hebig, E. Jung, T. Singh, A. Lepcha, S. Olthof, J. Flohre, Y. Gao, R. German, P. H. M. van Loosdrecht, K. Meerholz, T. Kirchartz, S. Mathur, *Sol. Energy Mater. Sol. Cells* **2016**, *158*, 195.
- [144] T. Krishnamoorthy, H. Ding, C. Yan, W. L. Leong, T. Baikie, Z. Zhang, M. Sherburne, S. Li, M. Asta, N. Mathews, S. G. Mhaisalkar, *J. Mater. Chem. A* **2015**, *3*, 23829.
- [145] S. Shao, J. Liu, G. Portale, H. H. Fang, G. R. Blake, G. H. Brink, L. A. Koster, M. A. Loi, *Adv. Energy Mater.* **2018**, *8*, 1702019.
- [146] X. Liu, Y. Wang, F. Xie, X. Yang, L. Han, *ACS Energy Lett.* **2018**, *3*, 1116.
- [147] J. C. Hebig, I. Kühn, J. Flohre, T. Kirchartz, *ACS Energy Lett.* **2016**, *1*, 309.
- [148] K. W. Wong, H. L. Y. Ip, Y. Luo, K. Y. Wong, W. M. Lau, K. H. Low, H. F. Chow, Z. Q. Gao, W. L. Yeung, C. C. Chang, *Appl. Phys. Lett.* **2002**, *80*, 2788.
- [149] D. Huang, T. Goh, J. Kong, Y. Zheng, S. Zhao, Z. Xu, A. D. Taylor, *Nanoscale* **2017**, *9*, 4236.
- [150] Z. Zhao, F. Gu, Y. Li, W. Sun, S. Ye, H. Rao, Z. Liu, Z. Bian, C. Huang, *Adv. Sci.* **2017**, *4*, 1700204.
- [151] Y. Yu, D. Zhao, C. R. Grice, W. Meng, C. Wang, W. Liao, A. J. Cimaroli, H. Zhang, K. Zhu, Y. Yan, *RSC Adv.* **2016**, *6*, 90248.
- [152] P. W. Liang, C. Y. Liao, C. C. Chueh, F. Zuo, S. T. Williams, X. K. Xin, J. Lin, A. K. Y. Jen, *Adv. Mater.* **2014**, *26*, 3748.

- [153] S. Sun, T. Salim, N. Mathews, M. Duchamp, C. Boothroyd, G. Xing, T. C. Sum, Y. M. Lam, *Energy Environ. Sci.* **2014**, *7*, 399.
- [154] Z. Xiao, C. Bi, Y. Shao, Q. Dong, Q. Wang, Y. Yuan, C. Wang, Y. Gao, J. Huang, *Energy Environ. Sci.* **2014**, *7*, 2619.
- [155] J. Seo, S. Park, Y. C. Kim, N. J. Jeon, J. H. Noh, S. C. Yoon, S. I. Seok, *Energy Environ. Sci.* **2014**, *7*, 2642.
- [156] Y. Liao, H. Liu, W. Zhou, D. Yang, Y. Shang, Z. Shi, B. Li, X. Jiang, L. Zhang, L. N. Quan, R. Quintero-Bermudez, B. R. Sutherland, Q. Mi, E. H. Sargent, Z. Ning, *J. Am. Chem. Soc.* **2017**, *139*, 6693.
- [157] N. Wang, Y. Zhou, M. G. Ju, H. F. Garces, T. Ding, S. Pang, X. C. Zeng, N. P. Padture, X. W. Sun, *Adv. Energy Mater.* **2016**, *6*, 1601130.
- [158] J. A. Christians, R. C. M. Fung, P. V. Kamat, *J. Am. Chem. Soc.* **2014**, *136*, 758.
- [159] K. P. Marshall, R. I. Walton, R. A. Hatton, *J. Mater. Chem. A* **2015**, *3*, 11631.
- [160] T. Minemoto, M. Murata, *Curr. Appl. Phys.* **2014**, *14*, 1428.
- [161] D. Zhou, T. Zhou, Y. Tian, X. Zhu, Y. Tu, *J. Nanomater.* **2018**.
- [162] F. Hao, C. C. Stoumpos, P. Guo, N. Zhou, T. J. Marks, R. P. H. Chang, M. G. Kanatzidis, *J. Am. Chem. Soc.* **2015**, *137*, 11445.
- [163] K. P. Marshall, M. Walker, R. I. Walton, R. A. Hatton, *Nat. Energy* **2016**, *1*, 16178.
- [164] F. D. Giacomo, A. Fakhruddin, R. Jose, T. M. Brown, *Energy Environ. Sci.* **2016**, *9*, 3007.
- [165] Q. Chen, H. Zhou, Z. Hong, S. Luo, H.-S. Duan, H.-H. Wang, Y. Liu, G. Li, Y. Yang, *J. Am. Chem. Soc.* **2014**, *136*, 622.
- [166] T. Yokoyama, D. H. Cao, C. C. Stoumpos, T. B. Song, Y. Sato, S. Aramaki, M. G. Kanatzidis, *J. Phys. Chem. Lett.* **2016**, *7*, 776.
- [167] S. J. Lee, S. S. Shin, J. Im, T. K. Ahn, J. H. Noh, N. J. Jeon, S. Seok, J. Seo, *ACS Energy Lett.* **2018**, *3*, 46.
- [168] S. Ito, S. Tanaka, K. Manabe, H. Nishino, *J. Phys. Chem. C* **2014**, *118*, 16995.
- [169] H. S. Kim, I. H. Jang, N. Ahn, M. Choi, A. Guerrero, J. Bisquert, N. G. Park, *J. Phys. Chem. Lett.* **2015**, *6*, 4633.
- [170] P. Zhu, C. Chen, S. Gu, R. Lin, J. Zhu, *Sol. RRL* **2018**, *2*, 1700224.
- [171] M. Zhang, M. Lyu, J. H. Yun, M. Noori, X. Zhou, N. A. Cooling, Q. Wang, H. Yu, P. C. Dastoor, L. Wang, *Nano Res.* **2016**, *9*, 1570.
- [172] W. Liao, D. Zhao, Y. Yu, C. R. Grice, C. Wang, A. J. Cimaroli, P. Schulz, W. Meng, K. Zhu, R. G. Xiong, Y. Yan, *Adv. Mater.* **2016**, *28*, 9333.
- [173] J. W. Lee, T. Y. Lee, P. J. Yoo, M. Gratzel, S. Mhaisalkar, N. G. Park, *J. Mater. Chem. A* **2014**, *2*, 9251.
- [174] T. Singh, A. Kulkarni, M. Ikegami, T. Miyasaka, *ACS Appl. Mater. Interfaces* **2016**, *8*, 14542.
- [175] K. Wojciechowski, S. D. Stranks, A. Abate, G. Sadoughi, A. Sadhanala, N. Kopidakis, G. Rumbles, C. Z. Li, R. H. Friend, A. K. Y. Jen, H. J. Snaith, *ACS Nano* **2014**, *8*, 12701.
- [176] G. Grancini, R. S. Santosh Kumar, A. Abrusci, H. L. Yip, C. Z. Li, A. K. Y. Jen, *Adv. Funct. Mater.* **2012**, *22*, 2160.
- [177] J. Cui, P. Li, Z. Chen, K. Cao, D. Li, J. Han, Y. Shen, M. Peng, Y. Q. Fu, M. Wang, *Appl. Phys. Lett.* **2016**, *109*, 171103.
- [178] J. Huang, X. Zhang, D. Zheng, K. Yan, C. Z. Li, J. Yu, *Sol. RRL* **2017**, *1*, 1600008.
- [179] M. V. Pelarda, B. C. Hames, I. G. Benito, O. Almora, A. M. Ontoria, R. S. Sanchez, G. Garcia Belmonte, N. Martín, I. M. Sero, *J. Phys. Chem. Lett.* **2016**, *7*, 4622.
- [180] A. Abrusci, S. D. Stranks, P. Docampo, H. L. Yip, A. K. Y. Jen, H. J. Snaith, *Nano Lett.* **2013**, *13*, 3124.
- [181] K. M. Boopathi, P. Karuppuswamy, A. Singh, C. Hanmandlu, L. Lin, S. A. Abbas, C. C. Chang, P. C. Wang, G. Li, C. W. Chu, *J. Mater. Chem. A* **2017**, *5*, 20843.
- [182] J. Dong, Y. Zhao, J. Shi, H. Wei, J. Xiao, X. Xu, J. Luo, J. Xu, D. Li, Y. Luo, Q. Meng, *Chem. Commun.* **2014**, *50*, 13381.
- [183] D. Y. Son, J. H. Im, H. S. Kim, N. G. Park, *J. Phys. Chem. C* **2014**, *118*, 16567.
- [184] Y. Xu, T. Liu, Z. Li, B. Feng, S. Li, J. Duan, C. Ye, J. Zhang, H. Wang, *Appl. Surf. Sci.* **2016**, *388*, 89.
- [185] F. Anwar, R. Mahbub, S. S. Satter, S. M. Ullah, *Int. J. Photoenergy* **2017**.
- [186] Z. Shao, T. L. Mercier, M. B. Madic, T. Pauporte, *Mater. Des.* **2018**, *141*, 81.
- [187] L. Y. Huang, W. R. L. Lambrecht, *Phys. Rev. B* **2013**, *88*, 165203.
- [188] Y. Dang, Y. Zhou, X. Liu, D. Ju, S. Xia, H. Xia, X. Tao, *Angew. Chem., Int. Ed.* **2016**, *55*, 3447.
- [189] U. Mandadapu, S. V. Vedanayakam, K. Thyagarajan, M. R. Reddy, B. Jagdeeshbabu, *Int. J. Renewable Energy Res.* **2017**, *7*, 1603.
- [190] M. C. Jung, S. R. Raga, Y. Qi, *RSC Adv.* **2016**, *6*, 2819.
- [191] C. M. Tsai, N. Mohanta, C. Y. Wang, Y. P. Lin, C. L. Wang, E. W. G. Diau, *Angew. Chem., Int. Ed.* **2017**, *56*, 13819.
- [192] H. Hoshi, N. Shigeeda, T. Dai, *Mater. Lett.* **2016**, *183*, 391.
- [193] W. Li, J. Li, J. Li, J. Fan, Y. Mai, L. Wang, *J. Mater. Chem. A* **2016**, *4*, 17104.
- [194] T. Fujihara, S. Terakawa, T. Matsushima, C. Qin, M. Yahiro, C. Adachi, *J. Mater. Chem. C* **2017**, *5*, 1121.
- [195] S. J. Lee, S. S. Shin, Y. C. Kim, D. Kim, T. K. Ahn, J. H. Noh, J. Seo, S. I. Seok, *J. Am. Chem. Soc.* **2016**, *138*, 3974.
- [196] F. Hao, C. C. Stoumpos, R. P. H. Chang, M. G. Kanatzidis, *J. Am. Chem. Soc.* **2014**, *136*, 8094.
- [197] T. Yokoyama, D. H. Cao, C. C. Stoumpos, T. B. Bin Song, Y. Sato, S. Aramaki, M. G. Kanatzidis, *J. Phys. Chem. Lett.* **2016**, *7*, 776.
- [198] X. Liu, Z. Yang, C. Chueh, A. Rajagopal, S. T. Williams, Y. Sun, A. K. Y. Jen, *J. Mater. Chem. A* **2016**, *4*, 17939.
- [199] T. B. Song, T. Yokoyama, C. C. Stoumpos, J. Logsdon, D. H. Cao, M. R. Wasielewski, S. Aramaki, M. G. Kanatzidis, *J. Am. Chem. Soc.* **2017**, *139*, 836.
- [200] F. Wang, J. Ma, F. Xie, L. Li, J. Chen, J. Fan, N. Zhao, *Adv. Funct. Mater.* **2016**, *26*, 3417.
- [201] C. Ferrara, M. Patrini, A. Pisanu, P. Quadrelli, C. Milanese, C. Tealdi, L. Malavasi, *J. Mater. Chem. A* **2017**, *5*, 9391.
- [202] C. Ran, J. Xi, W. Gao, F. Yuan, T. Lei, B. Jiao, X. Hou, Z. Wu, *ACS Energy Lett.* **2018**, *3*, 713.
- [203] E. Jokar, C. H. Chien, A. Fathi, M. Rameez, Y. H. Chang, E. W. G. Diau, *Energy Environ. Sci.* **2018**, *11*, 2353.
- [204] K. Chen, P. Wu, W. Yang, R. Su, D. Luo, X. Yang, Y. Tu, R. Zhu, Q. Gong, *Nano Energy* **2018**, *49*, 411.
- [205] C. M. Tsai, Y. P. Lin, M. K. Pola, S. Narra, E. Jokar, Y. W. Yang, E. W. G. Diau, *ACS Energy Lett.* **2018**, *3*, 2077.
- [206] W. Ke, C. C. Stoumpos, I. Spanopoulos, M. Chen, M. R. Wasielewski, M. G. Kanatzidis, *ACS Energy Lett.* **2018**, *3*, 1470.
- [207] W. Ke, C. C. Stoumpos, J. L. Logsdon, M. R. Wasielewski, Y. Yan, G. Fang, M. G. Kanatzidis, *J. Am. Chem. Soc.* **2016**, *138*, 14998.
- [208] W. Ke, C. C. Stoumpos, M. Zhu, L. Mao, I. Spanopoulos, J. Liu, O. Y. Kontsevoi, M. Chen, D. Sarma, Y. Zhang, M. R. Wasielewski, M. G. Kanatzidis, *Sci. Adv.* **2017**, *3*, e1701293.
- [209] D. H. Cao, C. C. Stoumpos, T. Yokoyama, J. L. Logsdon, T.-B. Song, O. K. Farha, M. R. Wasielewski, J. T. Hupp, M. G. Kanatzidis, *ACS Energy Lett.* **2017**, *2*, 982.
- [210] A. E. Maughan, A. M. Ganose, M. M. Bordelon, E. M. Miller, D. O. Scanlon, J. R. Neilson, *J. Am. Chem. Soc.* **2016**, *138*, 8453.
- [211] M. Konstantakou, T. Stergiopoulos, *J. Mater. Chem. A* **2017**, *5*, 11518.
- [212] Z. Chen, J. J. Wang, Y. Ren, C. Yu, K. Shum, *Appl. Phys. Lett.* **2012**, *101*, 093901.
- [213] T. B. Song, T. Yokoyama, S. Aramaki, M. G. Kanatzidis, *ACS Energy Lett.* **2017**, *2*, 897.
- [214] J. Jiang, C. K. Onwudinanti, R. A. Hatton, P. A. Bobbert, S. Tao, *J. Phys. Chem. C* **2018**, *122*, 17660.

- [215] M. H. Kumar, S. Dharani, W. L. Leong, P. P. Boix, R. R. Prabhakar, T. Baikie, C. Shi, H. Ding, R. Ramesh, M. Asta, M. Graetzel, S. G. Mhaisalkar, N. Mathews, *Adv. Mater.* **2014**, *26*, 7122.
- [216] X. Qiu, B. Cao, S. Yuan, X. Chen, Z. Qiu, Y. Jiang, Q. Ye, H. Wang, H. Zeng, J. Liu, M. G. Kanatzidis, *Sol. Energy Mater. Sol. Cells* **2017**, *159*, 227.
- [217] D. Sabba, H. K. Mulmudi, R. R. Prabhakar, T. Krishnamoorthy, T. Baikie, P. P. Boix, S. Mhaisalkar, N. Mathews, *J. Phys. Chem. C* **2015**, *119*, 1763.
- [218] E. S. Parrott, R. L. Milot, T. Stergiopoulos, H. J. Snaith, M. B. Johnston, L. M. Herz, *J. Phys. Chem. Lett.* **2016**, *7*, 1321.
- [219] T. B. Song, T. Yokoyama, J. Logsdon, M. R. Wasielewski, S. Aramaki, M. G. Kanatzidis, *ACS Appl. Energy Mater.* **2018**, *1*, 4221.
- [220] D. Moghe, L. Wang, C. J. Traverse, A. Redoute, M. Sponseller, P. R. Brown, V. Bulovic, R. R. Lunt, *Nano Energy* **2016**, *28*, 469.
- [221] A. E. Maughan, J. A. Kurzman, J. R. Neilson, *Inorg. Chem.* **2015**, *54*, 370.
- [222] A. Kaltzoglou, M. Antoniadou, D. Perganti, E. Siranidi, V. Raptis, K. Trohidou, V. Psycharis, A. G. Kontos, P. Falaras, *Electrochim. Acta* **2015**, *184*, 466.
- [223] X. Qiu, Y. Jiang, H. Zhang, Z. Qiu, S. Yuan, P. Wang, B. Cao, *Phys. Status Solidi RRL* **2016**, *10*, 587.
- [224] B. Lee, C. C. Stoumpos, N. Zhou, F. Hao, C. Malliakas, C. Y. Yeh, T. J. Marks, M. G. Kanatzidis, R. P. H. Chang, *J. Am. Chem. Soc.* **2014**, *136*, 15379.
- [225] B. Saparov, J. P. Sun, W. Meng, Z. Xiao, H. S. Duan, O. Gunawan, D. Shin, I. G. Hill, Y. Yan, D. B. Mitzi, *Chem. Mater.* **2016**, *28*, 2315.
- [226] B. Lee, A. Krenselewski, S. I. Il Baik, D. N. Seidman, R. P. H. Chang, *Sustainable Energy Fuels* **2017**, *1*, 710.
- [227] R. H. Kretsinger, V. N. Uversky, E. A. Permyakov, *Encyclopedia of Metalloproteins*, Springer, New York **2013**.
- [228] X. Lu, Z. Zhao, K. Li, Z. Han, S. Wei, C. Guo, S. Zhou, Z. Wu, W. Guo, C. L. Wu, *RSC Adv.* **2016**, *6*, 86976.
- [229] C. C. Stoumpos, L. Frazer, D. J. Clark, Y. S. Kim, S. H. Rhim, A. J. Freeman, J. B. Ketterson, J. I. Jang, M. G. Kanatzidis, *J. Am. Chem. Soc.* **2015**, *137*, 6804.
- [230] P. P. Sun, Q. S. Li, L. N. Yang, Z. S. Li, *Nanoscale* **2016**, *8*, 1503.
- [231] L. C. Tang, Y. C. Chang, J. Y. Huang, M. H. Lee, C. S. Chang, *Jpn. J. Appl. Phys.* **2009**, *48*, 112402.
- [232] I. Kopacic, B. Friesenbichler, S. F. Hoefler, B. Kunert, H. Plank, T. Rath, G. Trimmel, *ACS Appl. Energy Mater.* **2018**, *1*, 343.
- [233] M. J. Ju, J. Dai, L. Ma, X. C. Zeng, *J. Am. Chem. Soc.* **2017**, *139*, 8038.
- [234] P. Cheng, T. Wu, J. Zhang, Y. Li, J. Liu, L. Jiang, X. Mao, R. Lu, W. Deng, K. Han, *J. Phys. Chem. Lett.* **2017**, *8*, 4402.
- [235] M. Liang, M. G. Ju, J. Dai, X. C. Zeng, *Nanoscale* **2018**, *10*, 11314.
- [236] C. Y. Huang, X. C. Yan, G. Cui, Z. Liu, S. Pang, H. Xu, *CN Patent 103943368*, **2014**.
- [237] S. F. Hoefler, G. Trimmel, T. Rath, *Monatsh. Chem.* **2017**, *148*, 795.
- [238] L. C. Lee, T. N. Huq, J. L. M. Driscoll, *APL Mater.* **2018**, *6*, 084502.
- [239] A. J. Lehner, D. H. Fabini, H. A. Evans, C. A. Hebert, S. R. Smock, J. Hu, H. Wang, J. W. Zwanziger, M. L. Chabiny, R. Seshadri, *Chem. Mater.* **2015**, *27*, 7137.
- [240] X. Zhang, G. Wu, Z. Gu, B. Guo, W. Liu, S. Yang, T. Ye, C. Chen, W. Tu, H. Chen, *Nano Res.* **2016**, *9*, 2921.
- [241] C. Ran, Z. Wu, J. Xi, F. Yuan, H. Dong, T. Lei, X. He, X. Hou, *J. Phys. Chem. Lett.* **2017**, *8*, 394.
- [242] T. Okano, Y. Suzuki, *Mater. Lett.* **2017**, *191*, 77.
- [243] J. K. Wenderott, A. Raghav, M. Shtein, P. F. Green, S. Satpathi, *Langmuir* **2018**, *34*, 7647.
- [244] A. Kulkarni, T. Singh, M. Ikegami, T. Miyasaka, *RSC Adv.* **2017**, *7*, 9456.
- [245] J. Huang, Z. Gu, X. Zhang, G. Wu, H. Chen, *J. Alloys Compd.* **2018**, *767*, 870.
- [246] S. Sanders, D. Stummler, P. Pfeiffer, N. Ackermann, *MRS Adv.* **2018**, *3*, 3085.
- [247] S. M. Jain, D. Phuyal, M. L. Davies, B. Philippe, C. D. Castro, Z. Qiu, J. Kim, T. Watson, W. C. Tsoi, O. Karis, H. Rensmo, G. Boschloo, T. Edvinsson, R. Durrani, *Nano Energy* **2018**, *49*, 614.
- [248] W. Zhang, X. Liu, L. Li, Z. Sun, S. Han, Z. Wu, J. Luo, *Chem. Mater.* **2018**, *30*, 4081.
- [249] S. S. Shin, J. P. C. Baena, R. C. Kurchin, A. Polizzotti, J. J. Yoo, S. Wiegold, M. G. Bawendi, *Chem. Mater.* **2018**, *30*, 336.
- [250] H. Li, C. Wu, Y. Yan, B. Chi, J. Pu, J. Li, S. Priya, *ChemSusChem* **2017**, *10*, 3994.
- [251] Z. Zhang, X. Li, X. Xia, Z. Wang, Z. Huang, B. Lei, Y. Gao, *J. Phys. Chem. Lett.* **2017**, *8*, 4300.
- [252] N. A. Yelovik, A. V. Mironov, M. A. Bykov, A. N. Kuznetsov, A. V. Grigorieva, Z. Wei, E. V. Dikarev, A. V. Shevelkov, *Inorg. Chem.* **2016**, *55*, 4132.
- [253] M. R. Filip, S. Hillman, A. A. Haghighirad, H. J. Snaith, F. Giustino, *J. Phys. Chem. Lett.* **2016**, *7*, 2579.
- [254] D. M. Fabian, S. Ardo, *J. Mater. Chem. A* **2016**, *4*, 6837.
- [255] S. Sun, S. Tominaka, J. H. Lee, F. Xie, P. D. Bristowe, A. K. Cheetham, *APL Mater.* **2016**, *4*, 031101.
- [256] E. T. McClure, M. R. Ball, W. Windl, P. M. Woodward, *Chem. Mater.* **2016**, *28*, 1348.
- [257] A. H. Slavney, T. Hu, A. M. Lindenberg, H. I. Karunadasa, *J. Am. Chem. Soc.* **2016**, *138*, 2138.
- [258] F. Wei, Z. Deng, S. Sun, F. Xie, G. Kieslich, D. M. Evans, M. A. Carpenter, P. D. Bristowe, A. K. Cheetham, *Mater. Horiz.* **2016**, *3*, 328.
- [259] G. Giorgi, K. Yamashita, *Chem. Lett.* **2015**, *44*, 826.
- [260] N. C. Miller, M. Bernechea, *APL Mater.* **2018**, *6*, 084503.
- [261] G. Volonakis, M. R. Filip, A. A. Haghighirad, N. Sakai, B. Wenger, H. J. Snaith, F. Giustino, *J. Phys. Chem. Lett.* **2016**, *7*, 1254.
- [262] L. Zhang, C. Liu, L. Wang, C. Liu, K. Wang, B. Zou, *Angew. Chem., Int. Ed.* **2018**, *57*, 11213.
- [263] M. Khazaei, K. Sardashti, J.-P. Sun, H. Zhou, C. Clegg, I. G. Hill, J. L. Jones, D. C. Lupascu, D. B. Mitzi, *Chem. Mater.* **2018**, *30*, 3538.
- [264] S. S. Mali, H. Kim, D. Kim, C. K. Hong, *ChemistrySelect* **2017**, *2*, 1578.
- [265] Y. Kim, Z. Yang, A. Jain, O. Voznyy, G. H. Kim, M. Liu, L. N. Quan, F. P. G. de Arquer, R. Comin, J. Z. Fan, E. H. Sargent, *Angew. Chem., Int. Ed.* **2016**, *55*, 958666.
- [266] E. Greul, M. L. Petrus, A. Binek, P. Docampo, T. Bein, *J. Mater. Chem. A* **2017**, *5*, 19972.
- [267] P. C. Harikesh, H. K. Mulmudi, B. Ghosh, T. W. Goh, Y. T. Teng, K. Thirumal, M. Lockrey, K. Weber, T. M. Koh, S. Li, S. Mhaisalkar, N. Mathews, *Chem. Mater.* **2016**, *28*, 7496.
- [268] P. Karoppuswamy, K. M. Boopathy, A. Mohaptra, H. Chen, K. T. Wong, P. C. Wang, C. Chu, *Nano Energy* **2018**, *45*, 330.
- [269] Y. J. Li, T. Wu, L. Sun, R. X. Yang, L. Jiang, P. F. Cheng, Q. Q. Hao, T. J. Wang, R. F. Luc, W. Q. Deng, *RSC Adv.* **2017**, *7*, 35175.
- [270] F. Jiang, D. Yang, Y. Jiang, T. Liu, X. Zhao, Y. Ming, B. Luo, F. Qin, J. Fan, H. Han, L. Zhang, Y. Zhou, *J. Am. Chem. Soc.* **2018**, *140*, 1019.
- [271] R. Nie, A. Mehta, B. W. Park, H. Kwon, J. Im, *J. Am. Chem. Soc.* **2018**, *140*, 872.
- [272] B. Vargas, E. Ramos, E. P. Gutierrez, J. C. Alonso, D. S. Ibarra, *J. Am. Chem. Soc.* **2017**, *139*, 9116.
- [273] A. K. Baranwal, H. Masutani, H. Sugita, H. Kanda, S. Kanaya, N. Shibayama, Y. Sanehira, M. Ikegami, Y. Numata, K. Yamada, T. Miyasaka, T. Umeyama, H. Imahori, S. Ito, *Nano Convergence* **2017**, *4*, 26.
- [274] S. A. Adonin, L. A. Frolova, M. N. Sokolov, G. B. Shilov, D. V. Korchagin, V. P. Fedin, S. M. Aldoshion, K. J. Stevenson, P. A. Troshin, *Adv. Energy Mater.* **2018**, *8*, 1701140.

- [275] P. C. Harikesh, B. Wu, B. Ghosh, R. A. John, S. Lie, K. Thirumal, L. H. Wong, T. C. Sum, S. Mhaisalkar, N. Mathews, *Adv. Mater.* **2018**, *30*, 1802080.
- [276] M. Jahandar, J. H. Heo, C. E. Song, K. J. Kong, W. S. Shin, J. C. Lee, S. H. Im, S. J. Moon, *Nano Energy* **2016**, *27*, 330.
- [277] A. M. Elseman, M. M. Rashid, S. Sajid, Ali M. A. Hassan, A. M. Elseman, A. E. Shalan, S. Sajid, M. M. Rashad, A. M. Hassan, M. Li, *ACS Appl. Mater. Interfaces* **2018**, *10*, 11699.
- [278] M. R. Filip, F. Giustino, *J. Phys. Chem. C* **2016**, *120*, 166.
- [279] K. Choudhary, *Identification of Potential Replacement Materials for Lead in CH₃NH₃PbI₃ using First Principle Calculations*, **2015**, eprint: arXiv:1505.01238.
- [280] M. Suta, C. Wickleder, *J. Mater. Chem. C* **2015**, *3*, 5233.
- [281] J. I. Uribe, D. Ramirez, J. M. O. Guillen, J. Osorio, F. Jaramillo, *J. Phys. Chem. C* **2016**, *120*, 16393.
- [282] M. Pazoki, T. J. Jacobsson, A. Hagfeldt, G. Boschloo, T. Edvinsson, *Phys. Rev. B* **2016**, *93*, 144105.
- [283] T. J. Jacobsson, M. Pazoki, A. Hagfeldt, T. Edvinsson, *J. Phys. Chem. C* **2015**, *119*, 25673.
- [284] D. P. D. Rey, D. Forgacs, E. M. Hutter, T. J. Savenije, D. Nordlund, P. Schulz, J. J. Berry, M. Sessolo, H. J. Bolink, *Adv. Mater.* **2016**, *28*, 9839.
- [285] A. D. Raw, J. A. Ibers, *J. Solid State Chem.* **2012**, *192*, 34.
- [286] H. Arend, W. Huber, *J. Cryst. Growth* **1978**, *43*, 213.
- [287] J. Han, S. Nishihara, K. Inoue, M. Kurmoo, *Inorg. Chem.* **2014**, *53*, 2068.
- [288] M. A. Semaary, M. F. Mostafa, M. A. Ahmed, *Solid State Commun.* **1978**, *25*, 443.
- [289] P. P. Boix, S. Agarwala, T. M. Koh, N. Mathews, S. G. Mhaisalkar, *J. Phys. Chem. Lett.* **2015**, *6*, 898.
- [290] D. B. Mitzi, K. Liang, *Chem. Mater.* **1997**, *9*, 2990.
- [291] J. Grimm, J. F. Suyver, E. Beurer, G. Carver, H. U. Gudel, *J. Phys. Chem. B* **2006**, *110*, 2093.
- [292] M. Suta, W. Umland, C. Daul, C. P. Wickleder, *Phys. Chem. Chem. Phys.* **2016**, *18*, 13196.
- [293] L. M. C. Castro, A. M. Guloy, *Angew. Chem., Int. Ed.* **2003**, *42*, 2771.
- [294] M. Chen, M. G. Ju, A. J. D. Carl, Y. Zong, R. L. Grimm, J. Gu, X. C. Zeng, Y. Zhou, N. P. Padture, *Joule* **2018**, *2*, 1.
- [295] Y. Y. Sun, J. Shi, J. Lian, W. Gao, M. L. Agiorgousis, P. Zhang, S. Zhang, *Nanoscale* **2016**, *8*, 6284.
- [296] F. Hong, B. Saporov, W. Meng, Z. Xiao, D. B. Mitzi, Y. Yan, *J. Phys. Chem. C* **2016**, *120*, 6435.
- [297] Y. Y. Sun, M. L. Agiorgousis, P. Zhang, S. Zhang, *Nano Lett.* **2015**, *15*, 581.
- [298] S. Perera, H. Hui, C. Zhao, H. Xue, F. Sun, C. Deng, N. Gross, C. Milleville, X. Xu, D. F. Watson, B. Weinstein, Y.-Y. Sun, S. Zhang, H. Zeng, *Nano Energy* **2016**, *22*, 129.
- [299] L. R. Morss, M. Siegal, L. Stenger, N. Edelstein, *Inorg. Chem.* **1970**, *9*, 1771.
- [300] T. N. Tran, N. M. An, K. D. Nguyen, T. D. Nguyen, T. T. Truong, *J. Sci.: Adv. Mater. Devices* **2018**, *3*, 471.
- [301] J. Liu, M. Ozaki, S. Yakumaru, T. Handa, R. Nishikubo, Y. Kanemitsu, A. Saeki, Y. Murata, R. Murdey, A. Wakamiya, *Angew. Chem., Int. Ed.* **2018**, *57*, 13221.
- [302] J. H. Heo, J. Kim, H. Kim, S. H. Moon, S. H. Im, K. H. Hong, *J. Phys. Chem. Lett.* **2018**, *9*, 6024.
- [303] H. Kim, Y. H. Lee, J. H. Yoo, T. Park, J. H. Oh, *J. Mater. Chem. A* **2018**, *6*, 18173.
- [304] S. Hayase, N. Ito, M. A. K. Kamarudin, Q. Shen, Y. Ogomi, S. Iikubo, K. Yoshino, T. Minemoto, T. Toyoda, *Proc. SPIE* **2018**, 107371F.
- [305] M. Z. Rahamam, A. K. M. A. Hossain, *RSC Adv.* **2018**, *8*, 33010.
- [306] I. Benabdallah, M. Boujnah, A. E. Kenz, A. Benyoussef, M. Abatal, A. Bassam, *J. Alloys Compd.* **2019**, *773*, 796.
- [307] C. Zhang, S. Teo, L. Gao, Y. Kamata, T. MA, *Proc. SPIE* **2018**, 107240A.
- [308] S. Sanders, D. Stummler, P. Pfeiffer, N. Ackermann, F. Schimkat, G. Simkus, M. Heuken, P. K. Baumann, A. Vescan, H. Kalisch, *Phys. Status Solidi A* **2018**, *215*, 1800409.
- [309] C. Lu, J. Zhang, H. Sun, D. Hou, X. Gan, M. H. Shang, Y. Li, Z. Hu, Y. Zhu, L. Han, *ACS Appl. Energy Mater.* **2018**, *1*, 4485.
- [310] T. Jun, K. Sim, S. Iimura, M. Sasase, H. Kamioka, J. Kim, H. Hosono, *Adv. Mater.* **2018**, *30*, 1804547.
- [311] M. Aamir, M. D. Khan, M. Sher, N. Revaprasadu, M. A. Malik, J. Akhter, *New J. Chem.* **2018**, *42*, 17181.
- [312] K. Kumari, T. Chakrabarti, A. Jana, D. Bhattachartjee, B. Gupta, S. K. Sarkar, *Opt. Mater.* **2018**, *84*, 681.
- [313] N. Padture, *Proc. SPIE* **2018**, 107370R.
- [314] L. Zhou, J. F. Liao, Z. G. Huang, X. D. Wang, Y. F. Xu, H. Y. Chen, D. B. Kuang, C. Y. Su, *ACS Energy Lett.* **2018**, *3*, 2613.
- [315] Y. Zhao, D. Wei, J. Du, Z. Xu, *J. Electroceram.* **2019**, *42*, 74.
- [316] S. Raja, M. Vadivel, R. R. Babu, S. Kumar, K. Ramamurti, *Solid State Sci.* **2018**, *85*, 60.
- [317] E. Meyer, D. Mutukwa, N. Zingwe, R. Taziwa, *Metals* **2018**, *8*, 667.
- [318] M. Wang, P. Zeng, S. Bai, J. Gu, F. Li, Z. Yang, M. Liu, *Sol. RRL* **2018**, *2*, 1800217.
- [319] C. Lan, S. Zhao, J. Luo, P. Fan, *Phys. Chem. Chem. Phys.* **2018**, *20*, 24339.
- [320] N. Singhal, R. Chakraborty, P. Ghosh, A. Nag, *Chem. - Asian J.* **2018**, *13*, 2085.
- [321] Z. Zhang, L. Gao, T. Ma, *Proc. SPIE* **2018**, 107370W.
- [322] R. Das, R. N. P. Choudhary, *J. Mater. Sci.: Mater. Electron.* **2018**, *29*, 19099.